Sensitivity of the IceCube Detector for Ultra-High Energy Electron-Neutrino Events

DISSERTATION

zur Erlangung des akademischen Grades
doctor rerum naturalium
(Dr. rer. nat.)
im Fach Physik

eingereicht an der
Mathematisch-Naturwissenschaftlichen Fakultät I
Humboldt-Universität zu Berlin

von
Dipl.-Phys. Bernhard Voigt
geboren am 03.07.1977 in Hannover

Präsident der Humboldt-Universität zu Berlin:
Prof. Dr. Dr. h. c. Christoph Markschies

Dekan der Mathematisch-Naturwissenschaftlichen Fakultät I:
Prof. Dr. Lutz-Helmut Schön

Gutachter:

1. Prof. Dr. Hermann Kolanoski
2. Dr. Marek Kowalski
3. Prof. Dr. Shigeru Yoshida

eingereicht am:	30.04.2008
Tag der mündlichen Prüfung:	16.07.2008

Abstract

ICECUBE is a neutrino telescope currently under construction in the glacial ice at South Pole. At the moment half of the detector is installed, when completed it will instrument 1 km^3 of ice providing a unique experimental setup to detect high energy neutrinos from astrophysical sources.

In this work the sensitivity of the complete ICECUBE detector for a diffuse electron-neutrino flux is analyzed, with a focus on energies above 1 PeV. Emphasis is put on the correct simulation of the energy deposit of electromagnetic cascades from charged-current electron-neutrino interactions. Since existing parameterizations lack the description of suppression effects at high energies, a simulation of the energy deposit of electromagnetic cascades with energies above 1 PeV is developed, including cross sections which account for the LPM suppression of bremsstrahlung and pair creation. An attempt is made to reconstruct the direction of these elongated showers.

The analysis presented here makes use of the full charge waveform recorded with the data acquisition system of the ICECUBE detector. It introduces new methods to discriminate efficiently between the background of atmospheric muons, including muon bundles, and cascade signal events from electron-neutrino interactions. Within one year of operation of the complete detector a sensitivity of $1.5 \cdot 10^{-8} E^{-2}\,\mathrm{GeV\,s^{-1}\,sr^{-1}\,cm^{-2}}$ is reached, which is valid for a diffuse electron neutrino flux proportional to E^{-2} in the energy range from 16 TeV to 13 PeV. Sensitivity is defined as the upper limit that could be set in absence of a signal at 90 % confidence level. Including all neutrino flavors in this analysis, an improvement of at least one order of magnitude is expected, reaching the anticipated performance of a diffuse muon analysis.

Keywords:
IceCube, Neutrino, Cascade, LPM

Zusammenfassung

Zur Zeit wird das IceCube Neutrino-Teleskop am Südpol im Eis der Antarktis installiert, die Hälfte des Detektors ist bereits im Betrieb. Bei Fertigstellung im Jahr 2011 wird mehr als $1\,\mathrm{km}^3$ Eis mit Photovervielfachern instrumentiert sein. IceCube bietet damit eine einzigartige Möglichkeit, die Quellen der kosmischen Strahlung mit Hilfe hochenergetischer Neutrinos zu finden.

Im Rahmen dieser Arbeit wurde die Sensitivität des kompletten IceCube Detektors für den Nachweis eines diffusen Flusses von Elektronneutrinos bestimmt. Ziel war es, die Eigenschaften des Detektors für Energien oberhalb von einem PeV zu bestimmen. Besonderes Augenmerk wurde dabei auf die Simulation von elektromagnetischen Kaskaden gelegt, die in Neutrino-Nukleon-Wechselwirkungen auftreten. Da existierende Parametrisierungen die Unterdrückung der Wechselwirkungsquerschnitte durch den LPM-Effekt nicht beinhalten, wurde eine Simulation des Energieverlustes von elektromagnetischen Kaskaden für Energien oberhalb von 1 PeV entwickelt, die entsprechend modifizierte Wirkungsquerschnitte verwendet. Basierend auf den Ergebnissen dieser Simulation wird versucht, die Richtungsinformation von hochenergetischen Kaskaden zu rekonstruieren.

Die Analyse, die in dieser Arbeit vorgestellt wird, nutzt die komplette Information des durch einen Photovervielfacher aufgezeichneten Ladungsverlaufes aus, die mit der Datennahme des IceCube Detektors zur Verfügung steht. Es werden neue Methoden entwickelt, um zwischen atmosphärischen Myonen-Hintergrund- und Signalereignissen von Kaskaden aus Neutrino-Nukleon-Wechselwirkungen zu unterscheiden. Die erreichbare Sensitivität innerhalb einer Laufzeit von einem Jahr ist $1.5 \cdot 10^{-8} E^{-2}\,\mathrm{GeV\,s^{-1}\,sr^{-1}\,cm^{-2}}$ in einem Energiebereich von 16 TeV bis 13 PeV für den Nachweis von Elektronneutrinos eines diffusen Flusses, der einem E^{-2} Energiespektrum folgt. Die Sensitivität ist definiert als das obere Limit, welches bei nicht vorhandenem Signal, mit einem Konfidenzniveau von 90 % gesetzt werden kann. Eine Verbesserung von mindestens einer Größenordnung wird erwartet, wenn alle Neutrinofamilien in die Analyse einbezogen werden. Damit sollte eine Sensitivität erreicht werden, die auf dem gleichen Niveau einer diffusen Myonenanalyse liegt.

Schlagwörter:
IceCube, Neutrino, Kaskade, LPM

Für Tina und Emil.

Contents

Chapter 1

Introduction

Almost 100 years after the discovery of charged cosmic rays by V. Hess [77], their origin is still not clear, mainly because charged particles are deflected by interstellar magnetic fields and therefore do not point back to their sources. An exceptional case are particles with extremely high energies $\mathcal{O}(10\,\mathrm{EeV})$ which keep their directional information. However, their flux is low with less than one particle per year and square-kilometer, and due to interactions with the cosmic microwave background (CMB) radiation they can only travel limited distances $\mathcal{O}(50\,\mathrm{Mpc})$. Recently, the AUGER experiment, spanning an area of more than $3000\,\mathrm{km}^2$, observed a correlation between extremely high-energetic charged cosmic rays and the distribution of matter nearby our galaxy, including active galactic nuclei, one prime candidate source of cosmic rays [1]. This is a major step in the direction of the identification of the sources of charged cosmic rays, however, only at the highest energies.

Photons and neutrinos propagate in straight lines independent of energy, hence they are good messengers to find the sources of cosmic rays. The progress in the field of high energy photon-astronomy with the new generation of γ-ray telescopes like H.E.S.S. and MAGIC is impressive. Sources that are known from radio and optical astronomy are now seen in the light of high energy γ-rays. In addition sources are discovered which have not been seen before at all [17]. However, high energy γ-ray observations are also limited to short distances on astrophysical scales due to interactions with the CMB radiation and the extra-galactic background light. For example, above $\sim 100\,\mathrm{TeV}$ γ-rays do not survive the journey through our galaxy [104]. They also do not reveal their production mechanism as there are two competing scenarios which can explain the origin of high energy γ-rays, namely electromagnetic and hadronic acceleration scenarios. As only the latter produces charged cosmic rays, the observation of γ-rays can not solve the cosmic ray puzzle.

Neutrinos as cosmic messengers are tempting, because they would definitely reveal hadronic acceleration mechanisms as sources of charged cosmic rays. They would also provide crucial information about the in situ physical conditions of the sources as they are unaffected by intervening scattering processes. Additionally, the observation range is almost unlimited. It is the extremely low cross section of the weak interactions that make this possible, however, it makes it also very difficult to detect neutrinos. At energies above $\sim 1\,\mathrm{GeV}$ it is possible to use large natural target media with relatively sparse instrumentation of photomultiplier tubes (PMTs) to detect the Cherenkov light of charged secondary particles created in neutrino-nucleon interactions. The first high energy neutrino telescope in operation was the BAIKAL detector, followed by the AMANDA detector located at South Pole. Both collaborations could prove the working principle of high energy neutrino detectors in open water and glacial ice by detecting neutrinos produced in the atmosphere. However, no extraterrestrial neutrinos could be detected. Theoretical bounds on the neutrino fluxes predict that detectors of a least $1\,\mathrm{km}^3$ volume are required to observe extraterrestrial high energy neutrinos. See [108] for a review of astrophysical neutrino telescopes.

The ICECUBE experiment is currently installed at the South Pole as a successor of the AMANDA-II detector and will instrument a volume of $\sim 1\,\mathrm{km}^3$. At the time of this writing half of the detector is in operation and the completion of the array is planned for 2011. With KM3NET a second detector of the same size is proposed to be installed in the Mediterranean Sea [86]. The sensitivity of both instruments will surpass the upper theoretical bounds as studies similar to that performed in this work predict [21, 86, 96].

Two distinct event signatures are produced by the charged secondary particles of neutrino nucleon interactions. Tracks produced by muons allow to reconstruct the direction of the neutrino and the effective volume exceeds the actual detector volume due to the large range of high energy muons. The direction reconstruction allows to perform point-source searches and provides the opportunity to combine informations from other experiments and signal sources in a multi-messenger approach [2, 99]. The other signature is provided by particle cascades with energies, which deposit energy in a small volume, for energies below $\sim 100\,\mathrm{PeV}$. Hence, the effective volume for cascade detection is similar to the geometrical volume of the detector. An advantage over the muon channel is the good background rejection potential to remove atmospheric muons, which allows to perform a search over the full hemisphere. For detectors located in a medium like ice where light is strongly scattered, the directional information of cascades was not reconstructible up to now. Thus, for ICECUBE the cascade detection channel is still limited to diffuse flux searches, where the calorimetric measurement of an isotropic neutrino background is used to find an enhancement above the expected background from atmospheric neutrinos.

The results presented in this thesis focus on the electron-neutrino detection channel, with signals produced by hadronic and electromagnetic cascades. The original idea was to develop a direction reconstruction which would allow to perform point-source searches also in the cascade detection channel. Although several improvements to the simulation and reconstruction of cascade-like events were introduced the achieved direction reconstruction resolution is not sufficient. Hence, the focus of this work was directed to an analysis of a diffuse neutrino flux with the aim to obtain the best possible sensitivity for this approach exploiting the improvements of the IceCube readout system.

The outline of the thesis is described in the following. After a brief introduction to cosmic rays and high energy astrophysical neutrinos and their sources in Chapter 2 the principles of neutrino detection and the physical processes involved are summarized in Chapter 3. Emphasis is put on the physics of cascades, in particular on that of electromagnetic cascades at high energies where suppression effects can reduce the bremsstrahlung and pair production cross sections which increases the length of the energy deposit volume significantly. In order to include this effect in the signal response simulation of the detector, a simulation of electromagnetic cascades has been developed which is described in the same Chapter. An overview of the IceCube experiment is given in Chapter 4 with a detailed description of the sensors used for the Cherenkov light detection, which reflects the fact that part of my work was dedicated to the production and test of these instruments. The properties of glacial ice and the influence on the event reconstruction are discussed in the same Chapter. In Chapter 5 the reconstruction algorithms used in the sensitivity analysis are described, as well as the reconstruction which tries to deduce the direction of cascades based on the improvements of the cascade simulation.

Thereafter, a sensitivity study for a diffuse electron-neutrino flux is presented, which expands existing studies [21, 96], that are based on inadequate Amanda-II simulations which do not provide the full capabilities of the improved readout system of the IceCube sensors. The work presented here concentrates on electron-neutrino with energies above 1 PeV, similar to the energy range of studies presented in [6], which focuses on signals from muon-neutrinos and tau-neutrinos. The studies there simulate background based on an empirical model derived from experimental data taken with the 9-string configuration of the IceCube detector. The analysis presented here follows an approach similar to existing high energy analyses performed with Amanda-II, where specific high energy cosmic ray background samples are used [10]. The production of these samples, as well as the signal Monte Carlo samples are presented in Chapter 6. The sensitivity analysis is described in Chapter 7. It introduces new filter quantities which exploit the information of the waveform readout system of the IceCube detector and the application of a classification scheme not yet used in the collaboration. The results of the sensitivity study and the effective area for electron-neutrino detection as a function of energy are given in Chapter 8, followed by a brief discussion of statistical and systematic uncertainties. The thesis is completed by a summary and an outlook with recommendations for further improvements of this analysis for the existing and upcoming data from the IceCube detector.

Chapter 2

Cosmic Rays and High Energy Neutrinos

Neutrino flux predictions from cosmological objects are directly related to the observed cosmic ray spectrum. This Chapter gives an overview of the cosmic rays that have been observed and the possible sources, which are also believed to produce high energy neutrinos. The production mechanism of astrophysical neutrinos is briefly summarized and their expected flux rates are discussed.

2.1 High Energy Cosmic Rays

Cosmic rays have been observed over more than 13 orders of magnitude in energy, up to 10^{20} eV. At energies below ~ 100 GeV the cosmic ray flux, with approximately one particle per square meter and second, is still strong enough for direct observations with balloon or satellite experiments. However, the steeply falling flux requires larger detectors for observations of the cosmic ray flux above ~ 1 TeV. At these energies only indirect measurements of the primary particles are possible. This is done using detector arrays, which record secondary particles that are produced in extensive air showers initiated by high energy particles penetrating the atmosphere.

Generally the charged primary particles of the cosmic rays consist of protons, α-particles, nuclei of heavier elements and electrons [118]. The detailed chemical composition of the heavier nuclei is only known at energies where direct observations are possible and it follows mostly the abundance of solar elements. The composition is difficult to determine at high energies, because of the indirect measurements.

Charged particles with charge Z are deflected during propagation by intergalactic magnetic fields. Thus for energies $E < Z \cdot 100\,\mathrm{PeV}$, they do not point back to the sources. Neutral particles in the cosmic radiation like γ-rays, neutrinos and anti-neutrinos are not influenced by magnetic fields and hence point back to their sources. Figure 2.1 shows a compilation from several experiments which measure the charged cosmic ray flux. Above 10 GeV the energy follows a power law [59]:

$$\frac{dN}{dE} \propto E^{\gamma}, \tag{2.1}$$

which can be explained by stochastic particle acceleration in collision-plasmas as described below. There are two, possibly three breaks, where the power index changes. At the "knee" around 4 PeV the index changes from $\gamma \approx -2.67$ to $\gamma \approx -3.10$. A second "knee" is discussed where another steepening of the spectrum occurs at $\sim 400\,\mathrm{PeV}$ [80]. The spectrum becomes harder again at the "ankle" at energies $\sim 3\,\mathrm{EeV}$, where the index changes back to $\gamma \approx -2.75$. Finally, at $E > 300\,\mathrm{EeV}$ a strong suppression predicted by Greisen, Zatsepin and Kuzmin sets in, known as the GZK cutoff. At these ultra-high energies cosmic rays lose energy through pion production in interactions with the cosmic microwave background radiation [70, 149], as described in Section 2.4.3.

2.2 Sources of High Energy Cosmic Rays

There are two basic scenarios for the production of high energy charged cosmic rays referred to as "top-down" and "bottom-up" models. In top-down models, high energy cosmic rays are assumed to originate from the decay of super-heavy particles, with masses up to $10^{24}\,\mathrm{eV}$ which are predicted by theories beyond the Standard Model. These models avoid the GZK suppression since ultra high energy particles might be produced in the vicinity of the Earth. In addition, the decay products are accompanied by photons and neutrinos. The absence of these signatures and the confirmation of the GZK cutoff [145], however, favor the "bottom-up" scenarios, where charged particles are accelerated in distant sources to the highest energies observed in the cosmic ray spectrum.

The acceleration is commonly explained by the concept of stochastic particle collisions with inhomogeneous magnetic fields co-moving with plasma clouds in the interstellar medium, which is known as the "Fermi Mechanism" [55]. The inhomogeneities are found in gas clouds, and appear for example in shock fronts of supernova explosions and galaxy collisions. Particles crossing the field inhomogeneities back and forth will gain energy. In case of a plasma cloud with isotropical magnetic fields, the average relative gain

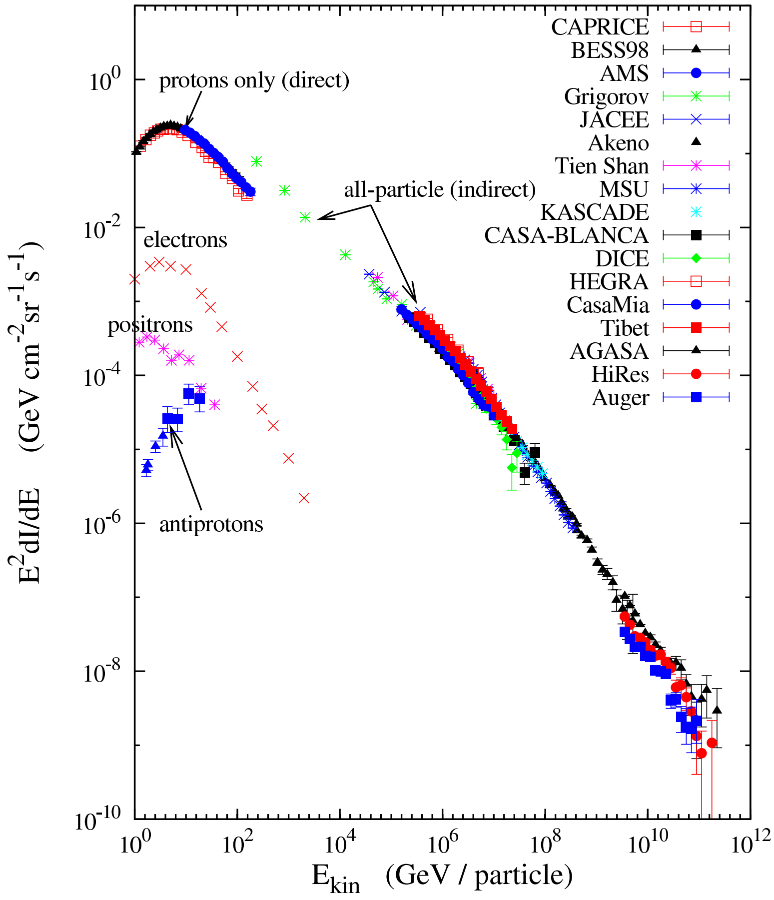

Figure 2.1: All particle cosmic ray spectrum. The data points are from different experiments as indicated in the legend. For references see [60], where the Figure is taken from.

is proportional to the squared velocity $\beta^2 = (v/c)^2$ of the cloud, i.e. it is a second order acceleration. In case of shock front acceleration, the deflections have a preferred direction and the average gain is more efficient and linearly proportional to the velocity β of the shock front [59].

The energy spectrum obtained from this model have spectral indices between -2.1 and -2.4 [104] which depend on the conditions of the acceleration region, e.g. magnetic field strength and orientation, velocity of the shock front, and the extension of the region where acceleration takes place. Taking into account propagation effects yields the observed spectral index of -2.7 up to the knee.

The change of the spectral index at the knee could be caused by two charge dependent cut-off energies. One is related to the acceleration mechanism which can have a maximum energy cut-off proportional to the particle charge Z. The other is due to the charged dependent rigidity $R = pc/eZ$, which lets particles with low Z escape more likely from the galaxy [80]. Hence, particles with low charge contribute less to the observed cosmic ray flux at high energies and the spectral index steepens.

The index change at the ankle is probably caused by a transition from galactic to extra-galactic sources as the origin of the charged cosmic rays as pointed out by Hillas [79]. Since the maximum energy gain is limited by the size of the acceleration region and magnetic field strength, one can exclude galactic sources as the origin of the cosmic rays above $\mathcal{O}(1\,\mathrm{EeV})$. Additionally, the observed particles are mainly isotropically distributed which requires travelling length of more than $\sim 50\,\mathrm{Mpc}$ for sufficient diffusion. Recently, the first evidence for the correlation between a catalog of active galactic nuclei (AGN) and cosmic rays with energies above 57 EeV have been seen in the region of the super-galactic plane [1]. This is a first step in the direction of the identification of extragalactic sources as the origin of cosmic rays with energies above $\mathcal{O}(10\,\mathrm{EeV})$.

Possible sources of high energetic charged cosmic rays have been observed in detail by photons in the low energy region $\mathcal{O}(<1\,\mathrm{TeV})$, which can have all possible wavelengths from radio over visible to X-ray and γ-ray. Over the last years the improved capabilities of imaging air Cherenkov telescopes like H.E.S.S. [14] and MAGIC [24] allowed observations of γ-rays with energies up to several TeV associated with sources known from low energy photon astronomy. The acceleration of high energy γ-rays can be explained by inverse Compton scattering. Photons of the synchrotron radiation field are "up-scattered" to high energies by electrons which have been accelerated in magnetic fields. The scenario is called Synchrotron Self Compton (SSC) model [34]. Another model is that of hadronic acceleration, known as proton-induced cascades or proton beamdump scenario. Within this model, high energy γ-rays are produced in the decay chain of high energy protons that have been accelerated at the sources. These protons produce π^0 particles in *pp* and pγ interactions, which decay into photons. The question whether high energy photons originate from (SSC) leptonic or hadronic processes is crucial for the observation of high energy neutrinos, which are only produced in the hadronic processes as described in Section 2.3. In turn, the observation of high energy neutrinos would reliably reveal the nature of the acceleration process and the sources of charged cosmic rays.

In the following, a brief overview of possible high energy cosmic ray sources is given. It mentions the most promising candidates only, while more details and references for the particular class can be found in [34, 59, 104, 118].

Supernova Remnants

A supernova remnant (SNR) is a leftover from a supernova, a massive star explosion at the end of its life cycle. The emitted material moves in shock fronts at typical velocities of $\sim 10^5\,\mathrm{m/s}$. SNRs are good candidates for the production of cosmic rays within our galaxy: the total energy flux emitted is large enough to sustain the cosmic ray flux from $\mathcal{O}(1\,\mathrm{GeV})$ up to the ankle and they the elements found in SNRs have the chemical abundance found in cosmic rays. γ-rays from SNRs with energies up to some TeV have been observed. Depending on the particular source, leptonic [23] and hadronic [15] acceleration scenarios are possible.

Pulsars and Binary Systems

Two other source classes of galactic origin are assumed to be responsible for the production of cosmic rays in the energy region between the knee and the ankle, namely pulsars and binary systems. Pulsars are driven by fast rotating neutron stars which are relic objects of supernova explosions of stars with masses similar to the Sun. Due to the very high magnetic fields of neutron stars, they are good candidates for particle acceleration. The emission observed is pulsed if the magnetic field and the rotational axis are not aligned. The luminosity is smaller than for SNRs and not strong enough to cause the cosmic ray flux at low energies, however, they probably contribute at energies above the knee. Pulsed emissions of high energy γ-rays $\mathcal{O}(100\,\mathrm{GeV})$ has not been detected yet [16].

In binary systems a neutron star or a black hole accretes mass from an accompanying star. The gained energy is emitted along the magnetic axis of the compact object into jets of plasma. Such systems can lead to particle acceleration with energies up to the ankle. They contribute to the total cosmic ray flux at energies above the knee. There are different classes of binary systems, two prominent examples are X-ray binaries and microquasars, the latter have been observed with periodic emissions of TeV γ-rays [113].

Active Galactic Nuclei

Active galactic nuclei are cores of galaxies with luminosities as large as the total luminosity of the host galaxy. They are assumed to be powered by a super-massive back hole ($M > 10^8 M_\odot$) with an accretion disk spiraling into the black hole and thereby radiating strongly at all optical wavelengths. Short time variabilities of the observed radiation require a compact engine [73]. Most of the energy is released into jets, which can extend over several Mpc, pointing away from the core parallel to the rotation axis of the object. Shock fronts around and within the accretion disk and the jets cause particle acceleration up to the highest energies observed. These particles form the extra-galactic contribution in the cosmic ray spectrum above the ankle. Depending on the orientation of the jets towards the Earth, the activity and luminosity of the radio and optical emission, AGNs are categorized following a classification scheme [34]. AGNs have been observed at energies up to several TeV with high energy γ-ray telescopes, a detailed list can be found in [34].

Gamma Ray Bursts

Gamma ray burst (GRB) are the brightest sources in the Universe, though they last only for short times from $10^{-3}\,\mathrm{s}$ to about $10^{3}\,\mathrm{s}$. The total energy output is therefore lower than for AGNs. Gamma ray burst have been observed in X-rays and GeV γ-rays, and in radio and optical wavelength during the afterglow which lasts long after the prompt emission. The isotropic distribution of observed GRBs suggests an extra-galactic origin, which is confirmed by the observation of emission lines and host galaxy identification during the afterglow phase. The current interpretation of how GRBs form is borrowed from supernova models. The large energy release is produced by a correspondingly large amount of gravitational energy that is released due to a core collapse of a massive object, or merging of compact objects. The favored model is the fireball model, where relativistic plasma shells are emitted which form shock fronts responsible for particle acceleration up to the highest energies. GRBs might contribute to the extra-galactic cosmic rays above the ankle. For details on GRBs see [109].

2.3 Astrophysical Neutrinos

Figure 2.2 shows the expected energy spectrum of astrophysical neutrinos covering 15 orders of magnitude in energy and more than 40 orders of magnitude in flux. In the following, the different classes of neutrino fluxes shown in the plot will be briefly discussed.

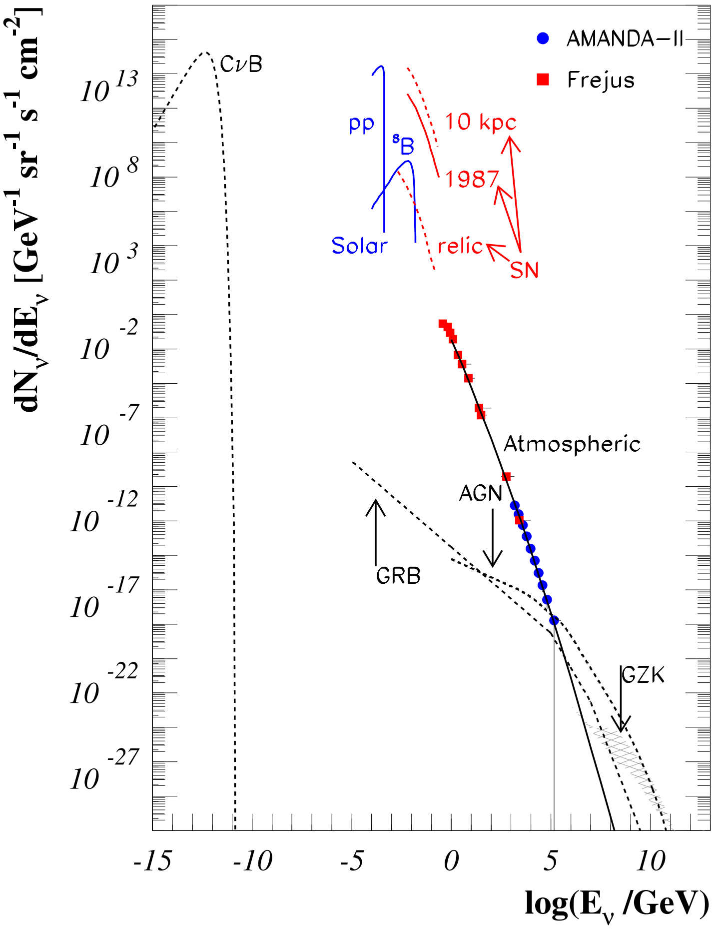

Figure 2.2: The astrophysical neutrino spectrum from different sources. Solid lines represent measured fluxes, dashed lines those from predictions. Figure is taken from [34].

Cosmic Neutrino Background

At the lowest energies the Figure shows the cosmic neutrino background, an isotropic neutrino flux decoupled from matter and expanding independently 1 s after the Big Bang similar to the cosmic microwave background radiation which decoupled $\sim 10^5$ years later [95]. Although it is a guaranteed flux, it has not been detected yet, due to the small cross section of low energetic neutrinos.

Solar Neutrinos

Above $\mathcal{O}(100\,\mathrm{keV})$ up to MeV energies neutrinos from the sun have been observed. They are dominantly created in proton-proton fusion processes. The figure also shows the spectrum from B^8 decays. One of the most important results is the observation of neutrino-flavor oscillations, which can explain the deficit of solar electron-neutrinos arriving at the Earth. See [89] for a review of solar neutrino experiments.

Supernova Neutrinos

Supernova neutrinos from SN 1987A [27], are the only neutrinos from outside the solar system which have been detected so far. They are created in thermal disintegration processes and have mean energies $\sim 15\,\mathrm{MeV}$. Though, their energy is below the detection threshold of high energy neutrino detectors like IceCube, they could be detected with these instruments. A supernova explosion in our galaxy would create a neutrino flux of the order of 10^9 neutrinos per cm^2, which can produce a global rate enhancement due to charged secondaries created in neutrino nucleon interactions in the detector volume.

Atmospheric Neutrinos

In extensive air showers, which are produced when cosmic rays interact in the upper atmosphere, secondary neutrinos are produced. These atmospheric neutrinos have been observed with experiments like Baikal, Amanda-II [18, 31], and IceCube [4]. Together with atmospheric muons they form the background in the search for extraterrestrial neutrinos. Neutrinos are mainly produced in meson decays, like pions and kaons. With rising energy the mesons travel longer distances before decaying due to the relativistic time dilatation. Hence, they interact and lose energy before decaying into neutrinos. Thus, the atmospheric neutrino spectrum is steeper than the primary cosmic ray spectrum with a spectral index of $\gamma \approx -3.7$ in the energy range 1 TeV to 1 PeV [104]. However, in these decays and already in the first interaction short-lived heavy hadrons with charm and beauty content can be produced, in particular at high energies. Due to the short livetimes $\mathcal{O}(10^{-12}\,\mathrm{s})$ these particles decay before interacting and produce a hard prompt neutrino component, additionally to the conventional neutrino flux. The uncertainties in the flux predictions for prompt neutrinos are larger than one order of magnitude and therefore the cross-over energy, where the prompt contribution dominates over the conventional flux might be anywhere between $10^4 - 10^6$ GeV. See [48] for a review of the different calculations.

The uncertainties of the conventional neutrino flux are estimated to be 20-25% and become larger at energies above $\sim 10\,\mathrm{TeV}$ [61]. Figure 2.3 shows predictions for atmospheric neutrino fluxes for electron and muon-neutrinos from different models including the contribution from prompt neutrinos. The conventional atmospheric electron-neutrino flux is suppressed due to the fact that electron neutrinos are almost exclusively produced in K^0_L decays [146], and high energetic muons will reach the detector before decaying. The prompt contribution for both neutrino flavors is similar. Not shown is the zenith angle dependence of the neutrino flux. The flux is larger close to the horizon due to an increased path length in the atmosphere, resulting in a higher decay probability for muons. The prompt flux contribution is almost isotropic.

Although atmospheric neutrinos are an irreducible background in searches for extraterrestrial neutrinos, they can be used to verify the detector performance. The observation of prompt neutrinos would provide valuable input for hadronic interaction models at high energies.

2.4 High Energy Neutrinos

Extending up to the highest energies three unobserved neutrino fluxes are depicted in Figure 2.2: a generic GRB flux [135], an upper limit for AGN contributions and neutrinos caused by the GZK cutoff [147]. The same objects which have been described above as potential sources of charged cosmic rays constitute also potential sources of these high energy neutrinos. Before possible fluxes and theoretical bounds are discussed, the production mechanism and neutrino flavor oscillation are described in the following.

2.4.1 Neutrino Production

In case of hadronic acceleration neutrinos will be produced when high energy protons interact with ambient matter or photon fields, which is known as the

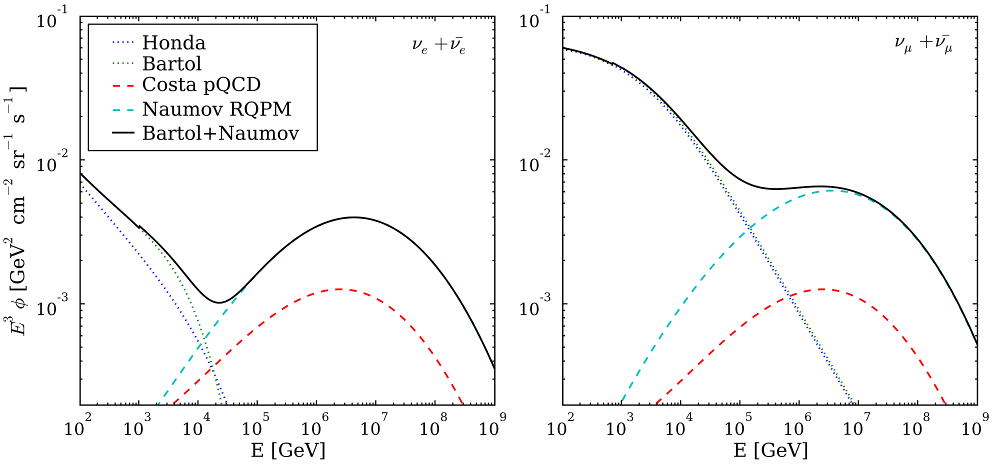

Figure 2.3: Atmospheric neutrino flux models for conventional fluxes and contributions from prompt neutrinos for electron (left) and muon neutrinos (right) averaged over one hemisphere. Conventional fluxes calculated by the Bartol group [32] and by Honda [82] are shown. Prompt models from pertubative QCD calculations taken from Costa [48] and calculations using a recombination quark parton model (RQPM) performed by Naumov [57] are shown. The black solid line is the sum of the RQPM and Bartol models.

beam dump scenario [104]. In proton-photon or proton-proton interactions short lived mesons will be produced:

$$p + X \rightarrow \begin{cases} \pi^0 + X \\ \pi^\pm + X \end{cases} , \tag{2.2}$$

$$p + \gamma \rightarrow \Delta^+ \rightarrow \begin{cases} \pi^+ + n \\ \pi^0 + p \end{cases} , \tag{2.3}$$

where the incident proton can also be replaced by a neutron and the equations are changed accordingly for the pions in the final state. Instead of pions also kaons can be created. The charged pions and kaons decay dominantly into leptons:

$$\pi^+ \rightarrow \mu^+ + \nu_\mu \rightarrow e^+ + \nu_e + \bar{\nu}_\mu + \nu_\mu \tag{2.4}$$

$$\pi^- \rightarrow \mu^- + \bar{\nu}_\mu \rightarrow e^- + \bar{\nu}_e + \nu_\mu + \bar{\nu}_\mu \,. \tag{2.5}$$

The neutrino flavor ratio follows from this equation to be $\nu_e : \nu_\mu : \nu_\tau = \bar{\nu}_e : \bar{\nu}_\mu : \bar{\nu}_\tau = 1 : 2 : 0$ under the assumption that the interaction length for the pions and muons is much larger than the decay length. The actual flavor ratio depends on the decay kinematics and the parent particle flux, however, it can be shown that the flavor ratio at all energies is almost constant [59].

2.4.2 Neutrino Oscillation

During propagation through cosmos, neutrinos oscillate as a consequence of non-vanishing neutrino masses. The flavor eigenstate, which appears in neutrino interactions as an associated lepton flavor, is a combination of the mass eigenstates. The linear combination of mass eigenstates $i = (1, 2, 3)$ that form the flavor eigenstates $\alpha = (e, \mu, \tau)$ is described by the unitarian Maki-Nakagawa-Sakata (MNS) matrix U^* [69]:

$$|\nu_\alpha\rangle = \sum_{i=1}^{3} U^*_{\alpha i} \, |\nu_i\rangle \, . \tag{2.6}$$

Applying the Schrödinger equation for time evolution to the mass eigenstates an energy and time dependent phase factor is added to each summand. The consequence is that the flavor of a massive neutrino changes as it propagates. The probability to observe a neutrino of flavor β at location x, which originally was produced with a flavor α is given by [29]:

$$\begin{aligned} P(\nu_\alpha \to \nu_\beta; x) &= |\, \langle \nu_\beta \, | \nu_\alpha(x) \rangle \,|^2 \\ &= \delta_{\alpha,\beta} - \sum_{i \neq j} U^*_{\alpha i} U_{i\beta} U^*_{\beta j} U_{j\alpha} \left(1 - \exp\left(\frac{-i\Delta m^2_{ij} x}{2E} \right) \right) , \end{aligned} \tag{2.7}$$

where $\Delta m^2_{ij} = m^2_i - m^2_j$ is the difference between the squared mass eigenstates and E the neutrino energy. The oscillation length is given by the exponential term and depends on the mass difference and energy. In the approximation of two flavor mixing, the length between two maxima of the oscillation is given by

$$L_{ij} = \frac{4\pi E \hbar}{\Delta m^2_{ij} c^3} = 2.48\,\mathrm{m} \left(\frac{E}{\mathrm{MeV}} \right) \left(\frac{\mathrm{eV}^2}{\Delta m^2_{ij}} \right)$$

Compared to astronomical distances the oscillation length is small. Hence, full mixing can be assumed for cosmic neutrinos and averaging the oscillation probability is possible. For a cosmic neutrino flux produced with a flavor ratio of $\nu_e : \nu_\mu : \nu_\tau = 1 : 2 : 0$ one expects to observe a flavor ratio of $1 : 1 : 1$ at the Earth due to oscillation [29].

2.4.3 Expected Diffuse Neutrino Fluxes

Galactic sources of charged cosmic rays and γ-rays are likely to produce neutrinos with energies below $\mathcal{O}(100\,\mathrm{TeV})$ and a diffuse flux might be difficult to detect [72]. They are not further discussed here, for a review of galactic neutrinos sources see [35]. The extra-galactic sources mentioned above are the prime candidates to produce neutrinos, whether observed as a diffuse flux above the atmospheric background or as point-sources. Especially, the observation of high energy γ-rays which might be produced in neutral pion decays motivates these candidates. The neutrino flux depends on the optical thickness of the sources and the energy transfer to the secondary particles in equation (2.2) and (2.3), in particular the energy transfer is different for pp and $p\gamma$ interactions.

The measured cosmic ray spectrum in the energy range from 10 PeV to 100 EeV can be used to estimate the diffuse flux from extra-galactic optically thin sources under the assumption of hadronic acceleration. An upper bound is derived by calculating the flux normalization for a generic E^{-2} injection spectrum which generates the same energy density as the charged cosmic ray flux. This assumes that the entire energy of the primary proton is transferred to the pions. The resulting bound is known as the Waxman-Bahcall bound and it is loosely confined to the range [72, 134]:

$$E^2\, dE/dN = 1 \sim 5 \cdot 10^{-8}\,\mathrm{GeV\,cm^{-2}\,s^{-1}\,sr^{-1}}\,.$$

Mannheim, Protheroe and Rachen (MPR) do not assume a fixed E^{-2} injection spectrum and take into account source characteristics, like the opacity to neutrons which determines the rate of the cosmic flux observed at the Earth [107]. The less restrictive bound is derived from sources being optically thick for nuclear interactions, where high energy neutrons are shifted towards lower energies before escaping the acceleration region, and the observed high energy cosmic ray flux is lower than at the acceleration site. Thus, the derived neutrino flux is higher than for an optically thin source, where the cosmic rays at the highest energies are not attenuated at the sources.

The neutrino spectrum from GRBs is modelled following the observed photon spectrum as a combination of two power laws. Again, this spectrum can be normalized to the observed flux of ultra-high energy cosmic rays, which has been done by Waxman and Bahcall in [135] for the prompt phase of the GRB. Also in the afterglow and hours before the GRB different models predict high energy neutrinos. A review of several extra-galactic neutrino flux models can be found in [34].

Cosmological Neutrinos

The Greisen-Zatseptin-Kuzmin (GZK) cutoff mentioned above describes the process of protons losing energy by interactions with the CMB radiation:

$$p + \gamma_{\mathrm{CMB}} \rightarrow \begin{cases} \Delta^+ \\ p + e^+ + e^- \end{cases}, \tag{2.8}$$

with threshold energies $E_{\text{th}}^{\Delta} \approx 5 \cdot 10^{19}$ eV and $E_{\text{th}}^{e^+e^-} \approx 5 \cdot 10^{18}$ eV, respectively. The attenuation length $\lambda = E/(-dE/dx)$ for resonant production of Δ^+ is only ~ 10 Mpc, while it is ~ 1000 Mpc for the pair creation process [34]. In particular the resonant Δ^+ production leads to a rapid decrease of the cosmic particle spectrum. Two experiments, namely HIRES and AGASA, measured incompatible fluxes. While HIRES observed a decline of the spectrum [34], AGASA detected two events above 50 EeV [130]. However, taking large systematic uncertainties into account, it is possible to interpret the two results to be consistent with the GZK cutoff [47]. Recent observations from the AUGER experiment exclude the continuation of the power law behavior above ~ 40 EeV with a significance of 6σ [145].

An important consequence of the GZK cutoff is the existence of ultra high energy neutrinos, which are produced in the decay chain of the Δ^+-resonance similar to the $p\gamma$ interactions described in equation (2.3). The resulting neutrinos are commonly referred to as cosmogenic or GZK neutrinos. The energy ranges from approximately 10 PeV to 1 ZeV [34]. The strength and shape of the spectrum depends on several parameters. In particular the evolution of the source population with redshift has a large impact on the modelling of the spectrum [41], as well as the maximum energy of the primary particle flux. Also the composition of the cosmic ray flux is crucial for the calculation. If heavier elements dominate at the highest energies, photodisintegration processes need to be taken into account, which suppress the cosmogenic neutrino flux [83].

Figure 2.4 shows a compilation of electron neutrino flux expectations and experimental flux limits for extraterrestrial neutrinos in the energy range from 10 TeV to 10 EeV. Up to ~ 50 TeV the spectrum is dominated by atmospheric neutrinos which is shown as a shaded area, to account for the variations due to the zenith angle dependence and the unknown contributions from prompt neutrinos. At these energies cosmic neutrinos could be detected as an excess of events in the energy spectrum of atmospheric neutrinos. Above 100-500 TeV the contribution from extraterrestrial neutrino fluxes exceeds that of the atmospheric neutrinos due to the steeply falling spectrum. The fluxes of cosmic neutrinos shown are the theoretical bounds discussed above, namely the Waxman-Bahcall bound and the MPR bound. The MPR bound is given by a shaded area, where the upper bound is valid for optically thick and the lower bound for optically thin sources. Also shown are the MPR model for neutrino production in AGN jets [107] and the model by Stecker, Done, Salamon and Sommers (SDSS) [126, 127]. Additionally, the Waxman-Bahcall GRB flux prediction is depicted, which has been mentioned above. A range of cosmogenic neutrino fluxes with different evolution parameters from [147] is indicated as a shaded area. Limits for fluxes $\propto E^{-2}$ from different experiments are shown, all-flavor limits are scaled with 1/3 to get comparable one-flavor limit: AMANDA-II analyses using 4 years ν_μ data (1), 3 year all neutrino flavors (3), 5 years cascade signatures (4), and 1 year all flavors with an enhanced data acquisition system (5) [3, 10, 13, 125]; BAIKAL all neutrino flavors (2) [30]; RICE all neutrino flavors (6) [101]; AUGER ν_τ (7) [38]; ANITA-LITE all neutrino flavors (8) [33]; an estimated ν_μ sensitivity of the complete ICECUBE detector within one year of operation (9) [21].

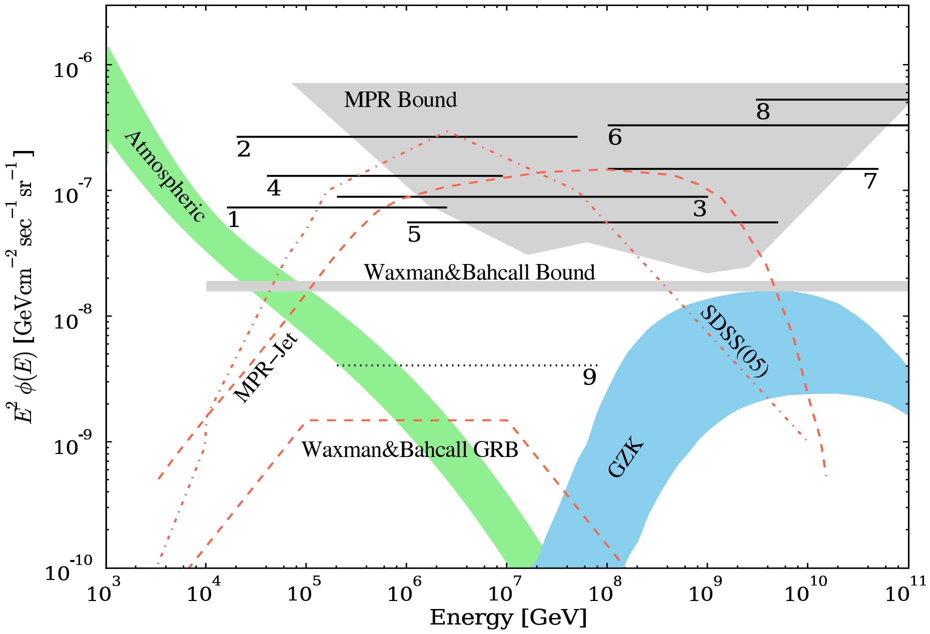

Figure 2.4: Flux predictions and theoretical bounds for electron neutrino fluxes. Models based on muon neutrino fluxes are scaled down by a factor of 2 to obtain the electron neutrino flux taking into account the production ratio and oscillation effects. The SDSS model is not scaled, because it does not account for anti-neutrinos and is therefore a factor 2 lower. Experimental limits for E^{-2} fluxes are shown from different experiments, all-flavor limits are scaled with 1/3: AMANDA-II analyses using 4 years ν_μ data (1), 3 year all neutrino flavors (3), 5 years cascade signatures (4), and 1 year all flavors with an enhanced data acquisition system (5) [3, 10, 13, 125]; BAIKAL all neutrino flavors (2) [30]; RICE all neutrino flavors (6) [101]; AUGER ν_τ (7) [38]; ANITA-LITE all neutrino flavors (8) [33]; an estimated ν_μ sensitivity of the complete ICECUBE detector within one year of operation (9) [21].

Chapter 3

Neutrino Detection

Neutrinos which are produced at cosmic objects need to propagate through space to reach the detector located on the Earth. During propagation the flavor state might change due to oscillation as discussed in the previous Chapter. Eventually, when the neutrino reaches the sensitive volume of the detector it may interact with the detector medium and thus can be detected. Since neutrinos are neutral particles which interact weakly, they can only be observed by secondary particles produced in these interactions which interact electromagnetically. Cherenkov detectors like IceCube detect the Cherenkov light produced by charged relativistic secondary particles. In order to reconstruct the energy and direction of the primary neutrino, it is important to understand how neutrinos interact, how the secondary particles deposit the energy in the detector and finally how the Cherenkov light is produced. All this is topic of this chapter, which briefly introduces physics processes involved in neutrino detection.

3.1 Neutrino-Nucleon Interactions

In the Standard Model (SM) description of particles and their interactions, neutrinos interact through the weak force which is mediated by the Z^0-boson and $W^{\pm}$-bosons. Two kinds of interaction processes are distinguished, charged current (CC) interactions mediated by $W^{\pm}$, where a charged lepton is produced and neutral current (NC) interactions, mediated by Z^0, where the neutrino from the initial state can also be found in the final state. The deep-inelastic-scattering process between the nucleon N and the neutrino ν_l with flavor l, produces in both cases a hadronic cascade X as the result of the hadronization of the debris of the nucleon:

$$\nu_l + N \xrightarrow{W^\pm} l + X \qquad (CC) \tag{3.1}$$

$$\nu_l + N \xrightarrow{Z^0} \nu_l + X \qquad (NC). \tag{3.2}$$

The charged secondaries of these interactions are detectable with Cherenkov light detectors, as described below. The cross sections for these processes have been calculated in [62]. It involves the evaluation of quark distribution functions of the target nucleon, which are measured at collider experiments [22, 42]. Tabulated versions of these functions are provided by the CTEQ collaboration [102]. At energies above $\sim 1\,\text{PeV}$ no experimental data is available and extrapolations have to be used. Uncertainties from different extrapolation models can reach a factor of two at energies around $100\,\text{EeV}$ [63]. Also, new physics could step in and considerably change the cross sections at the highest energies [43]. Relevant for the discussion in this work is the behavior of the integrated cross section:

$$\sigma_{\text{CC/NC}} \propto \left(\frac{1}{Q^2 + M_{W/Z}^2} \right)^2 E_\nu \,, \tag{3.3}$$

where $-Q^2$ is the invariant momentum transfer between the incident neutrino and the outgoing lepton; E_ν the energy of the neutrino; and $M_{W/Z}$ is the mass of mediating boson $M_W = 80\,\text{GeV}$ and $M_Z = 91\,\text{GeV}$, respectively. Figure 3.1 shows the integrated neutral and charged current cross sections for νN and $\bar{\nu} N$. The NC cross sections are lower than the CC cross sections, both rise linearly with energy up to $\sim 10^4\,\text{GeV}$. As the propagator term of the interaction $1/(Q^2 + M_{W/Z}^2)$ is then dominated by Q^2 which exceeds the mass of the boson, the rise is damped and $\sigma \propto E^{0.36}$ [95]. At low energies the cross section for $\bar{\nu} N$ is smaller, but it becomes equal to the νN cross section above $\sim 1\,\text{PeV}$ where the contribution from sea quarks dominates the quark distribution functions of the nucleon.

The νe^- interactions can generally be neglected, because owing to the small electron mass the cross section is much smaller. However, for $\bar{\nu}_e e^-$ interactions resonant W^- production occurs, leading to a cross section about 300 times higher than that for CC neutrino-nucleon interactions (Glashow resonance) at energies around $E_{\bar{\nu}_e} = M_W^2/2m_e \approx 6.3\,\text{PeV}$ [66]. The interactions $\bar{\nu}_e e \rightarrow W^- \rightarrow \bar{\nu}_\mu \mu$ and $\bar{\nu}_e e \rightarrow W^- \rightarrow X_{\text{hadr}}$ dominate in the energy range from $3\,\text{PeV}$ to $10\,\text{PeV}$ (see Figure 3.1). This offers a good chance to detect a signal from electron-neutrinos.

In contrast to muon searches, where a muon is required in the final state, in cascade analyses as presented in this work, the neutral-current channel

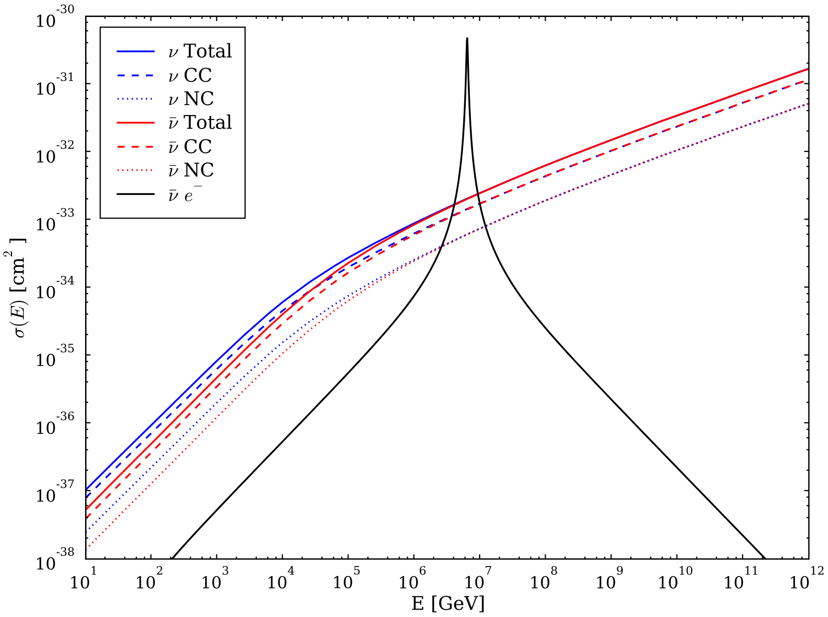

Figure 3.1: Neutrino-nucleon cross sections from 10 GeV to 100 EeV (data from [62]). The solid lines are the total cross sections, including CC (dashed) and NC (dotted) interactions. Anti-neutrino (red) and neutrino (blue) cross sections differ at energies below 1 PeV but are equal above. The resonant W^- production in $\bar{\nu}_e e^-$ interactions (black) with a peak at 6.3 PeV (Glashow resonance) is also shown.

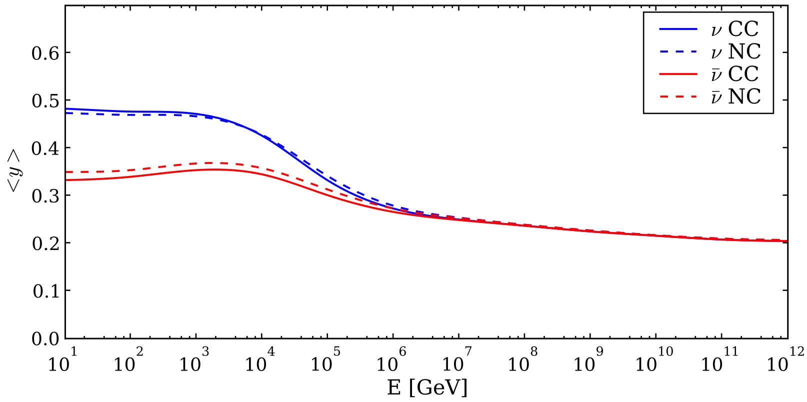

Figure 3.2: Mean of the inelasticity parameter of the charged current (solid) and neutral current (dashed) νN (blue) and $\bar{\nu}N$ (red) cross sections as a function of the neutrino energy (data from [62]).

offers also detection potential. For the assessment of a measured energy spectrum from cascade events, it is important to know the energy transfer to the nucleon and the corresponding energy deposit of the hadronic cascade. This is given by the inelasticity $y = 1 - E_l/E_\nu$ where E_l is the energy of the outgoing lepton. The mean value $\langle y \rangle$ as a function of the neutrino energy E_ν is shown in Figure 3.2. For high energies $\langle y \rangle$ approaches a value of ~ 0.2. However, as neutral-current and charged-current interactions have the same event signatures, it can only be taken into account for an error estimate of the energy reconstruction of the primary neutrino.

The mean scattering angle between the incident neutrino and the outgoing lepton is less than a degree for neutrino energies above 1 TeV [104], which is an important measure for point-source searches, as it is the upper limit of the angular resolution of the detector.

Absorption in the Earth

In the standard muon neutrino search one exploits the small neutrino nucleon cross section by looking for particles coming from below the horizon. Other particles like muons from air showers, which form the major background, are absorbed after propagating through a few kilometers of dense material. However, at high energies the steadily rising neutrino interaction cross sections interfere. The interaction length is given by:

$$L_{\text{int}} = \frac{1}{\sigma_{\text{tot}}(E_\nu)\frac{N_A}{A}\rho}, \tag{3.4}$$

where $N_A = 6.022 \cdot 10^{-23}\,\text{mol}^{-1}$ is Avogadro's number, A the atomic weight which is $1\,\text{g/mol}$ for nucleons, and ρ is the density of the medium, here taken to be water ($\rho = 1\,\text{g/cm}^3$). The interaction length is proportional to $1/\sigma$ and hence decreases with energy. Figure 3.3 shows the interaction length for neutrino-nucleon interactions and $\bar{\nu}_e e$-scattering as a function of the energy of the incident neutrino. Above ~ 50 TeV the earth diameter, shown as the dashed line, exceeds L_{int}. The interaction probability after traversing a column depth x is given by:

$$P(x) = 1 - \exp(-x/L_{\text{int}}). \tag{3.5}$$

It is obvious that high-energetic neutrinos are absorbed by the Earth. Hence, searches for ultra-high energy neutrinos are restricted to the upper hemisphere. Figure 3.4 shows the rate for neutrino interactions in the vicinity of the IceCube detector from a hypothetical E^{-2} ν_e flux as a function of energy and zenith angle. Above 100 TeV the contribution from neutrinos

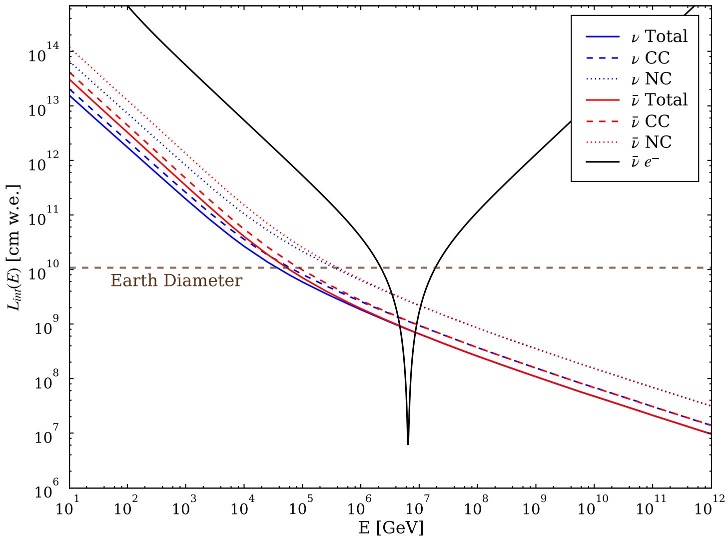

Figure 3.3: Interaction length for neutrino-nucleon interactions as a function of energy for charged-current (dashed), neutral-current (dotted), and total (solid) νN (blue) and $\bar{\nu} N$ (red) interactions. Also shown is the interaction length for $\bar{\nu}e^-$-scattering (black).

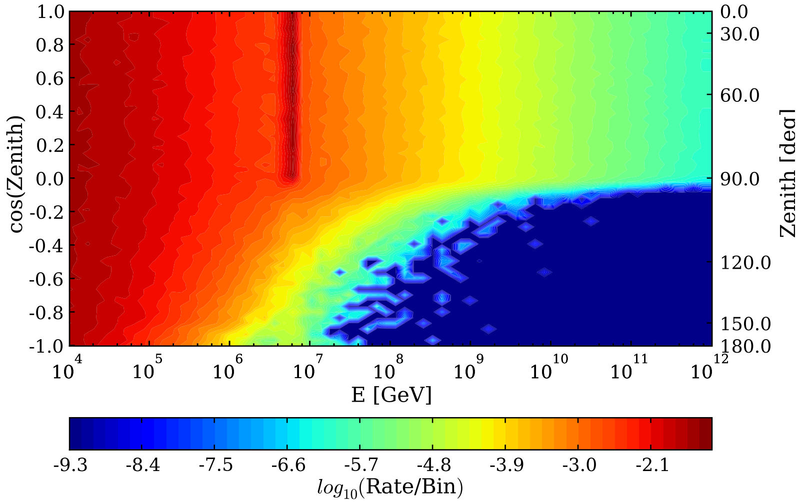

Figure 3.4: The interaction rate in a 1 km^3 target volume from a $\nu_e + \bar{\nu}_e$ flux ($1 \cdot 10^{-7} E^{-2}\,\mathrm{GeV\,s^{-1}\,sr^{-1}\,cm^{-2}}$) per energy and zenith angle bin. The angle bin width is equally spaced in cosine(zenith) to compensate the angle dependence of the integration area.

from the lower hemisphere gradually decreases, because the column depth $x = \int \rho dl$ is larger than the interaction length at these energies. At the highest energies only neutrinos with zenith angles smaller than 95 ° reach the detector. The increased interaction probability for $\bar{\nu}_e$ interactions due to the Glashow resonance is clearly visible for neutrinos coming from above the horizon. The increased absorption probability is barely visible, though.

Tau-neutrinos are affected differently by absorption. In case of CC interactions the tau-lepton decays rapidly due to its short lifetime of $\tau = 2.9 \cdot 10^{-13}$ s. The final state of this decay will again have a tau-neutrino with less energy. This process is commonly known as "tau-regeneration". In addition, due to the energy decrease, the interaction length increases. Details can be found in [74].

3.2 Event Signatures

Depending on the neutrino flavor and interaction type, there are distinct event topologies which appear in the detector. Two major classes can be distinguished, track-like and a cascade-like events, they are schematically depicted in Figure 3.5.

Cascade signatures are the results of short ranged energy deposits caused by electromagnetic or hadronic cascades in the final state of the neutrino interaction. For energies below 10 PeV the Cherenkov light of the charged secondaries in these showers is emitted in a limited volume $\sim 5\,\mathrm{m}^3$ and almost isotropically distributed after $\sim 25\,\mathrm{m}$ if one takes into account light scattering in ice. Due to light absorption in ice, the energy deposit needs to be in the vicinity if not in the detector volume itself. The typical signature of these events is a light flash propagating in all directions with a defined center. The details of the energy loss processes are discussed in the following sections.

In case of a track-like event, a high energetic muon is present in the final state which can travel large distances before it decays. If the muon track is crossing the detector volume, it is possible to detect muon-neutrinos which interacted far away from the detector. The energy loss along the track and the muon itself produce Cherenkov light. The typical event signature in this case is a track of light propagating through the detector. Again, the energy loss processes are described below. In the following the event signatures and corresponding interactions are summarized.

- All NC interactions and approximately 70% of $\bar{\nu}_e e^-$-scattering events at the Glashow resonance have hadronic cascades in the final state and hence appear as cascade-like events.

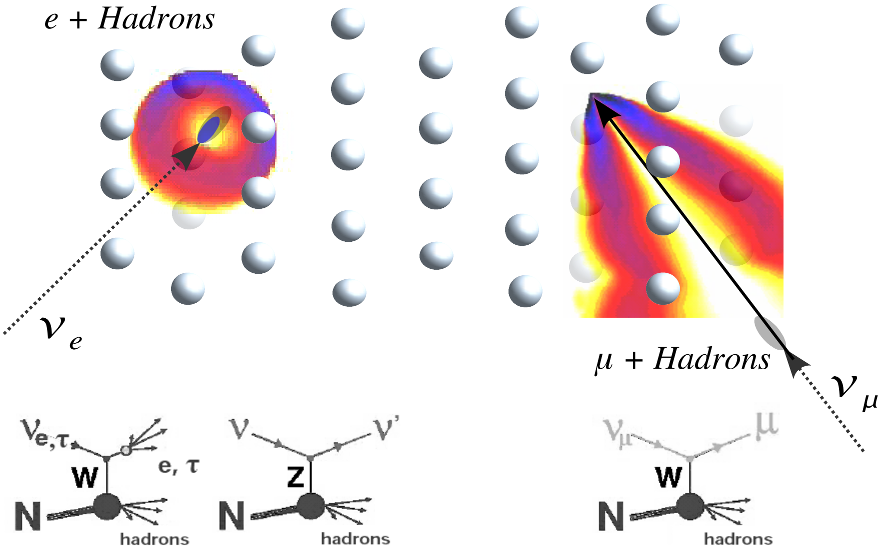

Figure 3.5: The plot shows a schematic view of the two event signature classes, as they appear in the IceCube detector (gray bullets). All neutral-current interactions and charged-current ν_e and low energetic ν_τ interactions have cascade-like signatures (left). The Cherenkov light (color patch) is distributed in a sphere with a localized center. Track-like events (right) originate typically from charged-current ν_μ interactions. The Cherenkov light is emitted into a distinct light cone around the muon track. Here, the contributions from secondary energy losses along the muon track are not shown.

- CC electron neutrino events have a hadronic and an electromagnetic cascade in the finale state. In $\sim 10\%$ of resonant $\bar{\nu}_e e^-$-scattering events an electromagnetic cascade is produced. They appear as cascade-like events.

- CC muon neutrino events have a muon and a hadronic cascade in the final state. In about 10% of $\bar{\nu}_e e^-$-scattering events at the Glashow resonance a muon is produced. Despite the hadronic cascade, the track-like character of the muon dominates this event signature.

- CC tau neutrino events and approximately 10% of the resonant $\bar{\nu}_e e^-$-scattering events will have a tau and a hadronic cascade in the final state. As the tau decays in 18% of the cases into a muon, some events appear track-like. Others appear as cascades, when the tau decays into electrons or hadrons. The decay length $\Delta x = \beta\gamma c\tau_{\mathrm{Life}}$ increases with energy and the tau decay can appear as a separate cascade. At 1 PeV the mean decay length is already 46 m and for a 100 PeV tau it is already above 1 km. Therefore, these events are rather complicated to interpret. Some can appear as "double bang" events with two distinct cascades in the detector. Others are called "lollipop" events, a track with one cascade (vertex or decay) inside the detector. If neither of the cascades is inside the detector, again, this event appears as track-like.

It should be mentioned, that there is no possibility to distinguish between hadronic and electromagnetic cascades, because they appear very similar in terms of Cherenkov light production, which will be described below. Thus, it is not possible to distinguish between a CC electron-neutrino event and a NC event of any flavor.

3.3 Cherenkov Radiation

Charged particles propagating through a medium with $v = \beta c$ larger than the local phase velocity of light emit Cherenkov radiation [84]. The process is negligible in terms of energy loss, however, it is widely used for particle detection. The threshold for Cherenkov radiation is given by $\beta = 1/n$. Given an index of refraction of $n = 1.33$ for ice and water, the corresponding threshold energies of electrons and muons are 0.26 MeV and 54 MeV, respectively. The light is emitted mainly into the direction of the Cherenkov angle:

$$\cos(\theta_c) = \frac{1}{n\beta}, \tag{3.6}$$

relative to the direction of the motion of the particle. The energy spectrum per unit track length for a particle with charge ze is given by [85]:

$$\frac{d^2N}{dxd\lambda} = \frac{2\pi\alpha z^2}{\lambda^2}\left(1 - \frac{1}{\beta^2\, n(\lambda)^2}\right), \tag{3.7}$$

where α is fine structure constant and the index of refraction n appears as a function of the wavelength λ. The number of photons emitted per unit length is obtained by integrating over the sensitive wavelength range of the detector. For the sensors used in the IceCube detector, it is taken to be $300 - 600\,\mathrm{nm}$ (see Section 4.1.1), which results in 32440 photons/m for $\beta \approx 1$. Given the total track length of a particle, the overall light yield can be calculated easily. For the different particle classes which appear in the context of high energy neutrino Cherenkov detectors (these are electromagnetic cascades, hadronic cascades and ionizing muons) the track lengths have been parametrized in [138].

3.4 The Physics of Cascades

For cascades the total track length parametrization sufficiently describes the energy dependence of the Cherenkov light yield. Knowing this relation one can reconstruct and simulate cascades in a reasonable manner. However, it does not take into account the development of the cascade in the medium and how energy is deposited in space and time. In this section the track length to energy relation is discussed in more detail and the underlying physical processes of the cascade development are described. In addition improvements to the treatment of cascades in the simulation, which have been developed in this work are introduced.

3.4.1 Energy loss by charged particles and photons in matter

Low energetic electrons loose energy due to ionization, which is roughly constant. However, radiative processes, namely bremsstrahlung, dominate already for energies of a few tens of MeV. In good approximation the cross section for bremsstrahlung processes is given by [146]:

$$\frac{d\sigma}{dk} = \frac{A}{X_0 N_A k}\left(\frac{4}{3} - \frac{4}{3}y + y^2\right), \tag{3.8}$$

where $y = k/E$ is the fraction of the electron's energy E transferred to the radiated photon with energy k, A is the atomic mass of the medium, and N_A

is Avogadro's constant. In this equation the "infrared limit" at small y and suppression effects (e.g. the LPM effect) are ignored. The energy weighted cross section for this process is shown in Figure 3.6. The energy loss due to bremsstrahlung can be approximated as

$$\langle dE/dx \rangle_{\mathrm{brems}} \approx -E/X_0. \tag{3.9}$$

This defines the radiation length X_0 as the length over which the electron loses all but $1/e$ of its energy. The radiation length has been calculated and tabulated [132], for ice it is $36.08\,\mathrm{g\,cm^{-2}}$.

The critical energy E_C is defined as the energy at which the energy loss per radiation length by ionization is equal to the electron energy. Thus, from equation (3.9) follows that at E_C ionization and bremsstrahlung energy losses are equal $(dE/dx)_{\mathrm{brems}} = (dE/dx)_{\mathrm{ion}}$. In solids, the critical energy is approximated by $E_C = 610\,\mathrm{MeV}/(Z + 1.24)$, for ice the value is $E_C \approx 78.99\,\mathrm{MeV}$.

Photons lose energy by the photo-electric effect; Compton and Rayleigh scattering; and at high energies mainly by pair creation, which is closely related to the process of bremsstrahlung. Indeed, the mean free path of pair creation is 9/7 of the radiation length and the cross sections definitions are alike. Without suppression effects and the same notation as in equation (3.8), the cross section is given by [146]:

$$\frac{d\sigma}{dx} = \frac{A}{X_0 N_A}\left(1 - \frac{4}{3}x + \frac{4}{3}x^2\right), \tag{3.10}$$

where $x = E/k$ is the fraction of the photon's energy k transferred to the pair-produced electron E. The cross-section is shown in Figure 3.7.

Heavy charged particles at moderate energies $\mathcal{O}(< 10\,\mathrm{GeV})$ lose energy in matter mainly due to ionization, which is well described by the Bethe-Bloch equation [146]. At higher energies radiative processes dominate as well. The relevant details for muon and hadrons are discussed in Sections 3.4.5 and 3.5.

3.4.2 The Landau-Pomeranchuk-Midgal Effect

At very-high energies the bremsstrahlung and pair production cross sections are suppressed due to influences of the surrounding material. The longitudinal momentum transfer between the target nucleus and an electron (photon) in bremsstrahlung (pair production) processes can be very small at high energies. The uncertainty principle dictates the interaction to be spread over a comparatively long distance, called the formation length. When the formation length is long and the surrounding material has enough influence on the interacting particle, even weak factors can perturb the interaction. The overview given here, follows [91, 146].

In case of the Landau-Pomeranchuk-Midgal (LPM) effect multiple scattering of the electron at surrounding nuclei is taken into account [103]. For example, in bremsstrahlung interactions, the electron can scatter multiple times in the formation zone, which adds an additional term to the longitudinal momentum transfer to the nucleus ($q_\parallel$) due to the change in the longitudinal velocity:

$$q_\parallel \propto \frac{k\, m_e^2}{E\,(E-k)} + k\,\langle \Theta^2 \rangle, \tag{3.11}$$

where $\langle \Theta^2 \rangle$ is the mean of the squared multiple scattering angle in one half of the formation length and k is the energy of the emitted photon. Scattering is significant if the second term dominates, which is the case for

$$k < \frac{E^2}{E + E_{\mathrm{LPM}}}, \tag{3.12}$$

where $E_{\mathrm{LPM}} = 7.7\,\mathrm{TeV/\,cm} \cdot X_0/\rho$ is a material dependent constant.

Again, the increased longitudinal momentum transfer dictates a somewhat shorter formation length in contrast to the one where scattering effects are neglected. As the emitted radiation is proportional to the formation length, the energy loss due to bremsstrahlung photons is reduced. In other terms, as q_{min} which increases being equal to $q_\parallel$, the form factor $F \propto \log(q_{\mathrm{max}}/q_{\mathrm{min}})$ decreases, which in turn is proportional to the cross section. As a consequence, the radiation length rises significantly for high energies and the longitudinal spread of a cascade can be vastly larger. Figure 3.6 shows the suppression of the bremsstrahlung cross section for different energies in ice. The radiation length is given by the integrated cross section and is depicted in the lower plot. In the low energy regime, where suppression effects can be neglected the radiation length is constant, however in the LPM regime, starting at $\sim 100\,\mathrm{TeV}$, the radiation length rises with $\log(E)$.

Multiple scattering can also reduce the cross section for pair creation. The threshold is higher than for bremsstrahlung processes, because the created electron and positron are the particles which scatter with nuclei of the surrounding material and they share the energy of the incident photon and the lower energetic particle dominates $q_\parallel$. Pair production is suppressed for

$$E\,(k-E) > k\,E_{\mathrm{LPM}}, \tag{3.13}$$

where E is the energy of the electron, $k - E$ that of the positron and k is the energy of the photon. Figure 3.7 shows the cross section for different

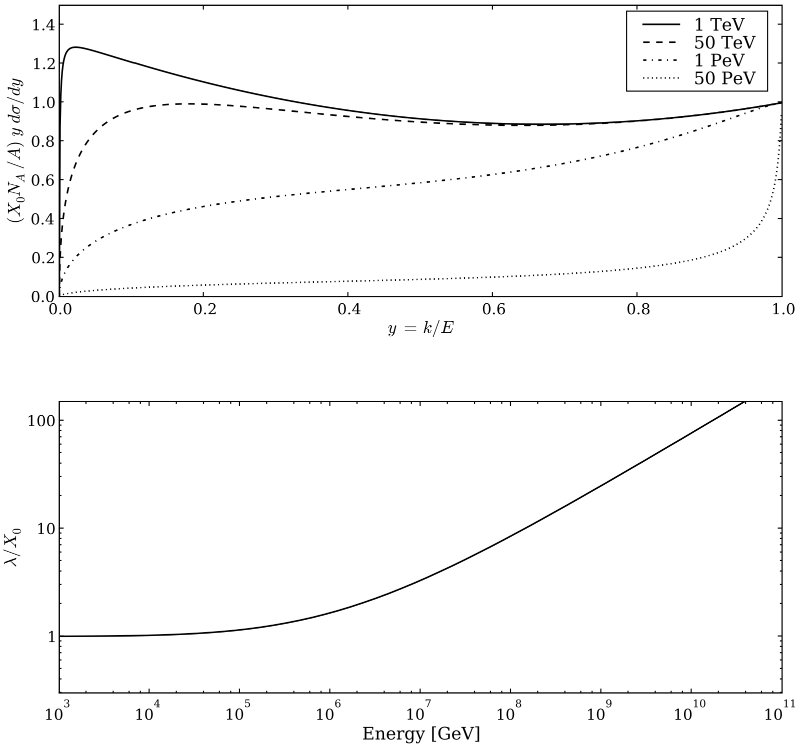

Figure 3.6: Top: Energy weighted normalized bremsstrahlung cross sections for different energies as a function of the fractional energy transfer to the radiated photon. The normal Bethe-Heitler cross section (solid line) is suppressed for higher energies, in particular the radiation of low energetic photons is suppressed. The vertical axis has units of photons per radiation length.
Bottom: Radiation length in ice as a function of energy in units of unsuppressed radiation length. Due to LPM suppression the radiation length increases for energies above 100 TeV.

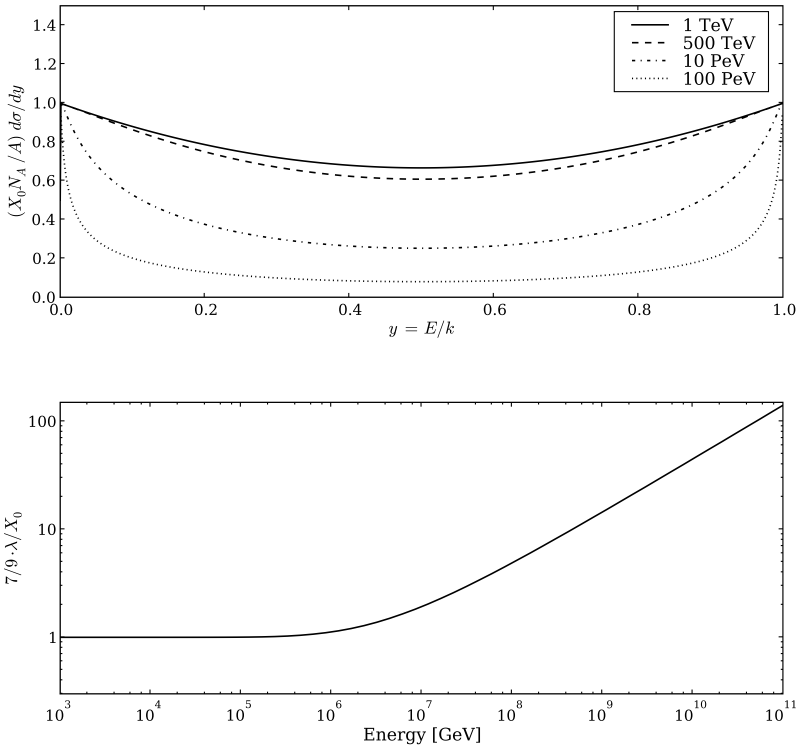

Figure 3.7: Top: Normalized pair production cross sections for different energies as a function of the fractional energy transfer to one of the secondaries. The normal Bethe-Heitler cross section (solid line) is suppressed for higher energies due to the LPM effect.
Bottom: Mean free path in ice as a function of energy in units of the unsuppressed mean free path ($9/7 \cdot X_0$). Due to LPM suppression the radiation length increases for energies above 1 PeV.

energies. For high energies, starting at $\sim 1\,\mathrm{PeV}$ the suppression is significant and the mean free path increases.

There are more mechanisms which can contribute to suppression, e.g. scattering of emitted photons and magnetic fields. Details can be found in [91]. The suppression of the pair creation cross section at energies above $10^{20}\,\mathrm{eV}$ is thwarted by rise of the photo-nuclear cross section. At these energies electromagnetic showers might turn into hadronic cascades when the photons produce hadrons rather than electron-positron pairs [92].

3.4.3 Electromagnetic Cascades

Based on the theoretical considerations given above, the development of electromagnetic cascades is described, followed by the description of a simulation for cascades at extremely high energies which takes the LPM effect into account.

Simplistic Model of Electromagnetic Cascades

When a high energetic electron of energy E_0 passes through matter it radiates bremsstrahlung photons, which in turn produce electron and positron pairs in pair creation interactions. In this iterative process an avalanche of particles is produced which leads to the development of a particle shower, also called a cascade. In a simplistic model one assumes that in each radiation length the number of particles is doubled and the energy is distributed equally to the secondaries, which is, after t radiation lengths, $E(t) = E_0/2^t$. This process ceases, when $E(t) < E_C$ and no more particles are produced. Solving for t yields the depth of the maximum and the number of particles at the maximum:

$$t_{\max} = \log_2(E_0/E_C) \qquad \text{and} \qquad N_{\max} = 2^{t_{\max}} = E_0/E_C\,. \tag{3.14}$$

Two important inferences can be drawn, the shower length scales logarithmically and the number of particles linearly with the primary energy E_0.

Cherenkov detectors measure the energy deposit of a cascade via the amount of Cherenkov light emitted by charged particles in the cascade. It is directly related to the total track length, i.e. the sum off all charged particle track lengths. Since the energy loss due to ionization is almost constant, the track length of a single particle is $\Delta x = E_C/(dE/dx)_{\mathrm{ion}}$. An estimate of the total track length is given by the integral over all particles with energies below E_C:

$$L = \Delta x \cdot N = \Delta x \cdot \int_o^{t_{\max}} 2^t dt \approx \Delta x \cdot E_0/E_C \approx (dE/dx)^{-1}_{\mathrm{ion}} \cdot E_0 = \alpha \cdot E_0\,. \tag{3.15}$$

The total track length is linearly dependent on the primary energy. Detailed simulations have been performed to determine $\alpha = 5.2\,\mathrm{m/\,GeV}$ in ice [97][1]. The total light yield of an electromagnetic cascade with energy E_0 is calculated by multiplying the total track length with the integral of equation (3.7).

The longitudinal energy deposit profile of a cascade, has a steeply rising leading edge, followed by a slow decrease after the maximum (Figure 3.8). It can be well described by a gamma distribution [146]:

$$\frac{dE}{dt} = E_0 b\, \frac{(bt)^{a-1}\, e^{-bt}}{\Gamma(a)}\,, \tag{3.16}$$

where $t = x/X_0$ is a length measured in units of radiation length. The parameters $a = 2.03 + 0.604 \cdot \log(E_0/\,\mathrm{GeV})$ and $b = 0.633$ have been determined for the Cherenkov light output of electromagnetic cascades in water [138].

The lateral distribution of particles is given in units of the Molière radius $R_M = 21\,\mathrm{MeV} \cdot X_0/E_c$ [146]. About 99% of the energy is contained within $3.5\,R_M$, which is roughly 35 cm for electromagnetic cascades in ice.

Important for the detection of cascades with Cherenkov detectors is the angular distribution of the Cherenkov light around a cascade. Again, this has been parametrized using simulations [138], it is strongly peaked in the direction of the Cherenkov angle (see Figure 4.14).

3.4.4 Simulation of Electromagnetic Cascades

The simulation and reconstruction of cascades in the Amanda-II detector was based on the assumption that the small spatial spread of cascades is negligible in contrast to the large distances between the detector modules. Hence, a cascade was treated as point-like light source, emitting Cherenkov light according to the parametrized angular distribution mentioned above. The light intensity is scaled according to the total track length. This might be suitable for energies below 100 TeV, where 99% of the cascade energy is contained in a volume with a length of 9 m. However, at high energies cascades show a distinct longitudinal spread, which should be accounted for in the simulation and reconstruction of cascade-like events. The lateral spread is in any case negligible for the optical detection, as it is very small and does not change much with energy.

In order to enhance the existing simulation by the longitudinal development of cascades, an algorithm used in previous works was adapted for the IceCube simulation. In this simple approach, a single cascade is replaced

---

[1] Though, in the detector simulation a value from older studies $\alpha = 4.37\,\mathrm{m/\,GeV}$ [138] is still in use.

by a sequence of sub-cascades. Each sub-cascade is displaced in space and time and attributed with an energy according to the energy loss profile of low energetic cascades given by equation (3.16). This is illustrated in Figure 3.8. The left plot shows the energy deposit profile of a electromagnetic cascade where dots indicate locations of sub-cascades. In the plot on the right the sub-cascades are displaced in space to account for the longitudinal development of the shower following the incident direction of 70 ° zenith angle. Details on the simulation algorithm can be found in Appendix A.

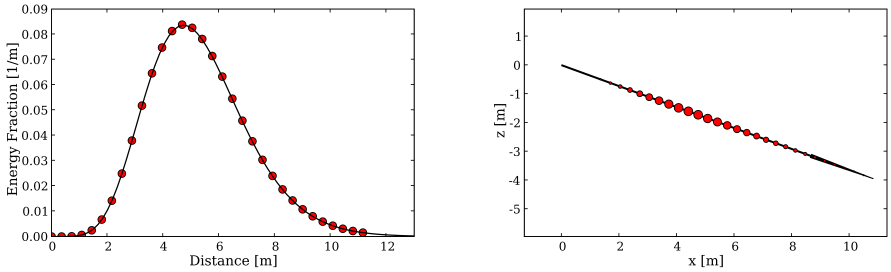

Figure 3.8: LEFT: Longitudinal energy deposit of a 100 TeV electromagnetic cascade (solid line). The red dots indicate locations of sub-cascades used as a replacement to simulate the longitudinal development of the cascade.
RIGHT: A series of sub-cascades which develops into the direction of the arrow. The simulated sub-cascades approximate the development of a 500 TeV cascade which propagates through the ice. The size of the sub-cascades corresponds to the energy deposit at that point.

Simulation of the energy deposit at extremely-high energies

At high energies above $\mathcal{O}(1\,\mathrm{PeV})$ the energy loss profile does not follow the parametrization anymore. The representation of a high energetic cascade by a list of sub-cascades is still applicable, however, the energy loss profile must be simulated individually. In this work a simulation was developed taking into account the LPM suppression effect for bremsstrahlung and pair creation processes (Figure 3.7 and 3.6), following existing simulation packages [116, 148]. Details on the simulation can be found in Appendix A.

Figure 3.9 shows the result of two simulations for an electromagnetic shower with an energy of 10 EeV. The showers extend over more than 200 m and show a distinct structure varying significantly between the two showers. Due to the LPM suppression, some high energy electrons and photons propagate large distances $\mathcal{O}(10\,\mathrm{m})$ before they deposit some of their energy. These energy deposits, if below the LPM threshold, follow the regular parametrization. Thus the energy loss profile of an extremely-high energetic electromagnetic cascade looks like a track consisting of multiple high energetic cascades separated by a few meters. The energy loss profile fluctuates strongly between different cascades, because the path length of particles depends on their energy which is determined by the stochastic energy transfer to the secondaries.

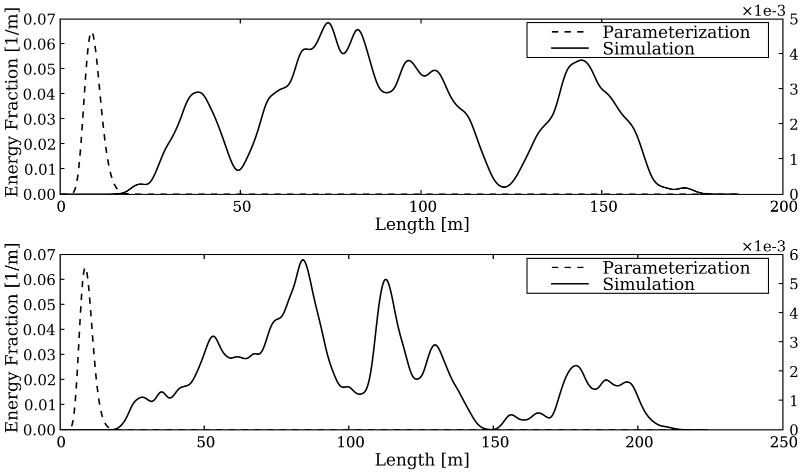

Figure 3.9: Simulated energy deposit profiles of two 10 EeV electromagnetic cascades (solid line). Due to the stochastic processes involved, the shower profiles fluctuate strongly between different simulations. Also shown the is the parametrization which fails to describe the energy deposit at extremely-high energies (note the different scale on the right y-axis).

The spread of the shower over more than hundred meters is crucial in two ways. First, the distinction between high-energetic muons and high-energetic cascades could be difficult, since muons create high-energetic bremsstrahlung cascades along their path and as the Cherenkov light from the muon is negligible, they also appear as a track consisting of multiple cascades, though still much longer. Second, it might be possible to reconstruct the direction of extremely-high energetic cascades. This will be discussed in Section 5.2.1.

3.4.5 Hadronic Cascades

The treatment of hadronic cascades is more difficult. Despite a prompt electromagnetic component mainly due to π^0 production, the development of the hadronic component involves more processes. In particular due to slow noncharged particles like neutrons and the dissipation of energy into hadronic binding processes, as well as the higher Cherenkov radiation threshold for heavier particles, the linear scaling of the total track length with the energy deposition is not given. Additionally, the light output is lower compared to an electromagnetic cascade. However, using a phenomenological model one can parametrize the difference in the total track length $F = T_{\text{hadronic}}/T_{\text{EM}}$ as a function of the energy of the incident particle [98]. In this sense, hadronic showers can be represented by electromagnetic cascades with an appropriate energy scaling[2]. The scaling factor is shown in Figure 3.10. Interestingly, due to the increasing number of π^0s in high energetic hadronic cascades, the scaling factor approaches unity for increasing energy.

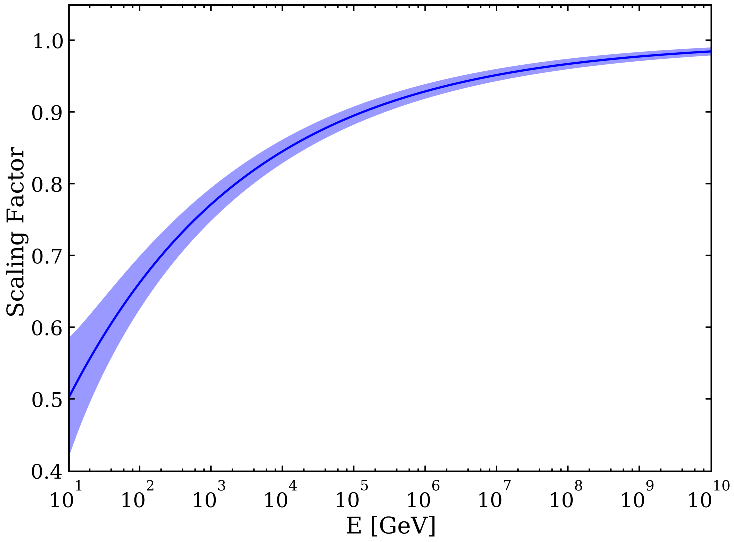

Figure 3.10: The energy scaling factor to convert hadronic to electromagnetic showers. The width of the band exhibits the spread, which is used to account for fluctuations.

An important feature of hadronic cascades is the production of high energetic muons. Muons could change the typical event signature of an almost spherical light distribution around the cascade vertex, even for intermediate energetic cascades. These muons would travel longer distances before they are stopped and could stick out of the Cherenkov light ball. On average, cascades above 10 PeV produce one muon with an energy $\sim 100\,\text{GeV}$ which is around the detection threshold [117].

---

[2] This is necessary, because the simulation of light propagation is limited to deal with electromagnetic showers only.

The energy spectrum of muons produced in hadronic cascades was simulated in ice with a modified CORSIKA version which is currently under development and offers a great potential to study high energetic interactions in water and ice [37, 40]. Before the hadronic cascade is scaled and replaced by a set of electromagnetic sub-cascades, the energy transfer into muons is calculated and the resulting muons are added to the event.

The LPM-effect is not taken into account for the simulation of the longitudinal energy deposit of hadronic cascades. In the first interaction, the energy is distributed over multiple particles and π^0s produced will get only a small fraction of the primary energy and hence, photons from pion decays will probably have energies below the LPM-threshold. Additionally, high energy neutral pions $\mathcal{O}(10\,\mathrm{PeV})$ might interact, rather than decay into photons. The highest energetic hadronic cascades studied in this work, are below 10 EeV, and the probability for these to have a photon with an energy above 100 PeV is less than 50% and steeply decreasing to higher photon energies [25]. The increase of the mean free path for an 100 PeV photon is less than a factor of 7. Thus, it is expected that the LPM effect for hadronic showers for this study can be neglected.

3.5 Energy Loss by Muons

The energy loss by muons is governed by ionization, bremsstrahlung, photonuclear interactions and pair production. However, it is much smaller than that for electrons and the energy deposit is distributed over long distances.

The energy losses along the muon track are of stochastic nature, though the low energetic losses due to ionization can be treated as continuous because they are prevalent and almost constant. The high energy losses are energy dependent. The average energy loss rate is given by [146]:

$$\frac{dE}{dx} = -a - bE,$$

where in ice $a \approx 2.7\,\mathrm{MeV}/(\mathrm{g\,cm^{-2}})$ and $b \approx 4 \cdot 10^{-6}/(\mathrm{g\,cm^{-2}})$ [46]. Solving for x gives the average muon range for a given energy which is proportional to $\log(E)$. For example a 1 TeV muon can penetrate roughly 2 km ice before it is stopped.

In particular the stochastic interactions produce lots of high-energetic secondaries which are typically electromagnetic and hadronic cascades. In case of very high energetic or even “catastrophic” energy losses, where a large fraction of the muon energy is deposited in a single interaction, the resulting electromagnetic shower can imitate a cascade-like event. Also coincident muons or multiple parallel muons could mimic an almost isotropically distributed light pattern. This needs to be addressed in the event selection of a cascade analysis in order to reduce the contribution from misidentified events.

Chapter 4

The IceCube Experiment

IceCube is a kilometer-scale high energy neutrino observatory currently constructed in the ice near the geographic South Pole. It is designed to detect neutrinos with energies from $\sim 100\,\mathrm{GeV}$ up to a few tens of EeV [20]. A deep detector array in the ice and a surface array called IceTop comprise the two main components of IceCube. Both parts use the same detectors, called Digital Optical Modules (DOM), to detect the faint Cherenkov light of relativistic charged particles propagating through ice. Figure 4.1 shows a schematic illustration of IceCube. The “InIce” array uses the 3 km thick glacial ice sheet as a detection medium. The modules are installed on vertical strings, each holding 60 DOMs. The alignment is on a hexadiagonal grid with horizontal spacing of 125 m between the strings. Along a string DOMs are separated by 17 m and distributed uniformly over depths from 1450 m to 2450 m. The light sensitive photo-tubes are pointing downwards, in order to increase the sensitivity for up-going muons.

The IceTop array consists of tanks with frozen water, each instrumented with two DOMs. These tanks are grouped in pairs, called a station, and are buried just below the surface next to each string. IceTop is designed to study extensive air showers in the energy range 300 TeV– 1 EeV. One of the major goals is to measure the cosmic ray composition around the “knee” region $\mathcal{O}(1\,\mathrm{PeV})$, which is possible with coincident measurement of air showers at the surface and the high energetic muon component in the ice. The ratio of these components depends on the mass of the primary particle.

At completion in 2011 IceCube will consist of 75 strings (possibly 5 more) and the corresponding IceTop tanks. In total, more than 4500 DOMs will instrument a volume of more than $1\,\mathrm{km}^3$. DOMs are suspended in a harness from the main string. At the present state (spring 2008) the observatory consists of 40 IceTop stations and 40 strings with 2530 DOMs.

IceCube embeds the predecessor Amanda-II array completed in 2000 [26].

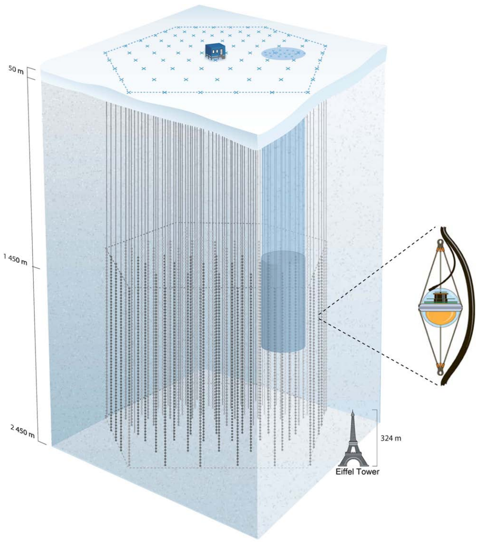

Figure 4.1: Schematic view of the IceCube observatory. The location of Amanda-II is indicated as a shaded cylinder. The Eiffel Tower is shown to get an impression of the size. On the right a DOM as it is deployed in the ice. It is suspended in its harness from the main cable of a string.

With a denser spacing of 677 optical sensors compactly arranged on 19 strings, Amanda-II provides a lower detection threshold. This is beneficial for analysis focusing on low energetic neutrinos, e.g. dark matter searches [71]. In addition, a low energy extension called “Deep-Core” will be installed in the center of IceCube below 2000 m, where the ice is clear. Due to the smaller spacing between the modules, this low-energy extension has a lower detection threshold. It offers the possibility to study contained events and will allow observations of neutrinos over the full solid angle, as the surrounding “InIce” array can be used as a veto.

In the following, the data acquisition system is described in detail. The properties of the ice, which is the main detector material, are discussed afterwards. Both topics are important in order to interprete and reconstruct data recorded with the IceCube detector.

4.1 Data Acquisition (DAQ)

The remote location of the IceCube observatory at South Pole and the harsh conditions demand a highly reliable data acquisition system and components. In particular, the optical modules, once buried in the ice, are inaccessible at later times and can only be configured and maintained via remote connections. It is necessary to be able to execute complex operational and maintenance functions remotely from the northern hemisphere.

In addition, the dead time of the system should be small and a precise timing of the Cherenkov light arrival times is necessary to reconstruct the direction of the incident neutrino if possible.

In order to obtain high quality data, each DOM digitizes the analog signal response and sends the data on request to the global DAQ at the surface. Figure 4.2 shows a schematic view of the organization and interplay of the primary DAQ subsystems components. The DOM production, functionality and performance is described in the next Section. Here follows a brief list of the functionalities of the surface DAQ components:

- the DOMHub controls and collects data from all DOMs on one string;
- the master clock distributes GPS signals to the DOMHubs to maintain a global time;
- the String Processor synchronizes and sorts signals from DOMs on one String and assigns the Coordinated Universal Time;
- the trigger subsystem groups the signals according to time and source (e.g. "InIce" events);
- the event builder and filter software combines signals, which fulfill trigger conditions, to events and creates data streams based on different filters.

Except the DOM hardware and the readout PCI cards located in the DOMHubs all downstream components of the DAQ system are software constructs and run on standard PC platforms communicating via TCP/IP over Ethernet.

Trigger

The DOM is a self-triggered device and launches the local data acquisition when a signal exceeds a configurable threshold, with the possibility to interrogate neighbors on the same string to ensure local coincidence conditions.

The trigger system at the surface combines DOM-launches to decide whether a global event trigger condition is fulfilled. The readout configuration defines a readout time window of typically $\pm 5\,\mu$s around the event trigger. Currently there is a minimum bias trigger which creates an event around every 200th launch, with a dead time of $5\,\mu$s afterwards. The simple majority trigger is defined by a multiplicity of 8 and 6 launches within

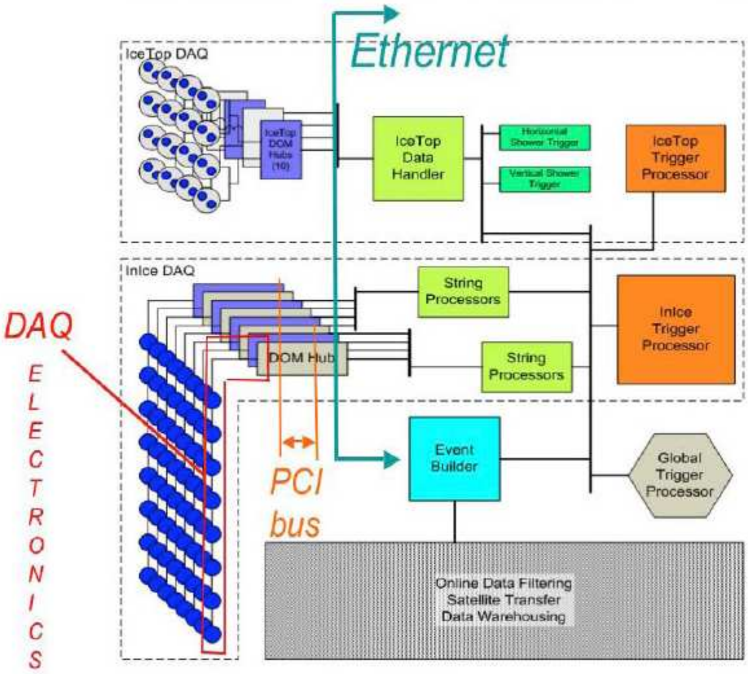

Figure 4.2: Schematic view of the DAQ subsystem components. See text for a description. Picture taken from [128].

$5\,\mu$s for the “InIce” and IceTop array, respectively. For 2008, it is foreseen to have a string trigger which requires 5 DOM launches from one run of 7 adjacent DOMs on one string in a time window of $1\,\mu$s. Individual triggers are combined by the global trigger.

At South Pole data is written to tape and is completely available only one year later, when these tapes are sent to the northern hemisphere. Part of the data is available via satellite transmission for immediate analyses. Since the bandwidth is limited, filters are installed which aim to select events for a certain analysis class. These different data streams are copied on a daily basis to the northern hemisphere.

4.1.1 The Digital Optical Module

The DOM is the fundamental element of the IceCube detector system. It is a nearly autonomous data acquisition platform. Already in Amanda-II a complete string with a prototype version of the DOM was deployed [11] and the operation principle could be proven. The different components of the DOM and their arrangement are shown schematically in Figure 4.3. The faint Cherenkov light is converted to an electrical signal and amplified by a HAMAMATSU R7081-02 photomultiplier tube. It has a 25 cm diameter spherical photocathode and 10 dynodes, offers a low noise rate (200–300 Hz at $-40\,^{\circ}$C [75]) and is operated at a nominal gain of 10^7 for the DOMs located deep in ice. The IceTop DOMs are operated at a nominal gain of $5{\cdot}10^5$ and $5{\cdot}10^6$ to increase the dynamic range. The maximum quantum efficiency is approximately 25%.

The PMT rests in a Room Temperature Vulcanization (RTV) silicone gel, which provides optical coupling to the glass sphere and mechanical support for the PMT and all the electronics, which are supported by the neck of the PMT. A mu-metal wire cage provides magnetic shielding, improving the PMT performance. Different printed circuit boards (PCB) are arranged concentrically around the tube.

On top of the PMT is a passive base to distribute high voltage to the PMT anode and dynodes. A "flasher board" with twelve Light Emitting Diodes (LED) arranged in six pairs, which emit light at 405 nm wavelength, is mounted on top of the main electronics stack. The “flashers” are a powerful tool for calibration and determining the optical properties of the ice. The LEDs on the lower side of the board are pointing horizontally, to send light pulses straight to the neighboring strings. The LEDs on the upper side are inclined at the Cherenkov angle. All LEDs can be pulsed individually or in combinations. They are extremely bright, emitting roughly 10^9 photons per pulse. A flashing DOM can be used to mimic the Cherenkov light pattern

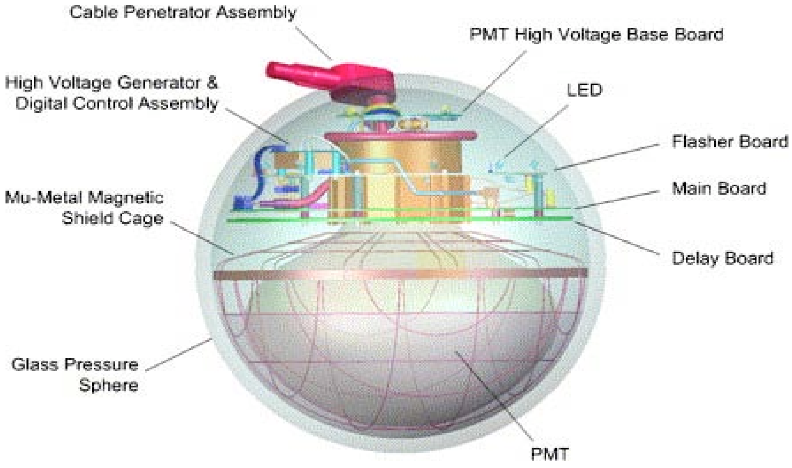

Figure 4.3: Schematic view of a Digital Optical Module (DOM). The picture shows the assembly of the DOM. See text for a full description of the different components. Picture taken from [5].

of a cascade of $\sim 10\,\mathrm{TeV}$, allowing to test cascade reconstruction algorithms. A high voltage generator is mounted on the flasher board and provides the voltage necessary of the operation of the PMT of up to 2 kV.

The mainboard (MB), which is described in the following paragraph, contains most of the functionality of the DOM. Below the mainboard is another PCB which contains a 75 ns delay line which is part of the front-end signal path. Communication with the surface is via twisted pair copper wires, which penetrate the pressure sphere in a molded assembly. The signal transmission over twisted pair wires reduces cross talk. On the outer end it is connected to the main cable. The cables and connectors are immune against high pressure, as well as the 13 mm thick glass sphere, which is able to withstand pressures exceeding 500 bar.

DOM Mainboard and Signal Capture

The DOM mainboard is the core of the IceCube data acquisition system. Besides signal recording, processing and transfer, it manages also functions like state control, message management, analog calibration, time calibration, and monitoring. These are provided in a Field Programmable Gate Array (FPGA) with an embedded CPU in conjunction with Analog to Digital Converters (ADC) and Digital to Analog Converters (DAC). Figure 4.4 shows a block diagram of the main components of the mainboard.

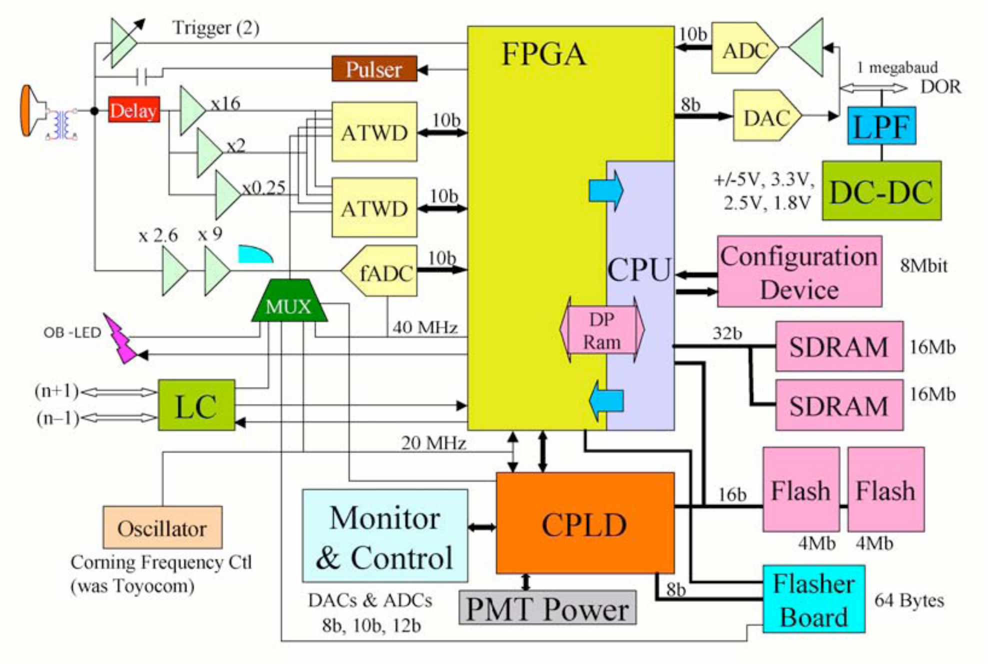

Figure 4.4: Block diagram of the DOM mainboard, see text for a detailed description. Picture taken from [128].

On the upper left the front-end electronics are depicted. The PMT anode signal (waveform) is coupled to the mainboard via a transformer[1]. The signal is split into different paths. Two low noise discriminators (comparators) are configured to launch the signal processing if a configurable threshold is exceeded. The single photo-electron (SPE) discriminator is set to a level of 0.25 pe[2], the multi photo-electron (MPE) discriminator is used to trigger dedicated signal processing tasks, when a bright signal is recorded.

After a delay line another PMT signal path is fed into three gain stages with amplification factors of $\times 16$, $\times 2$, and $\times 0.25$ which are presented to three Analog Transient Waveform Digitizer (ATWD) channels. The ATWD is a 128-sample deep switched capacitor array, which samples a signal onto the capacitors at a programmable rate [93], currently set to 3.3 ns/sample. This provides 420 ns of high-speed sampling. On request, the sampled charges are digitized by the ATWD using 128 10-bit ADCs. This requires 30 μs per channel, however, it can be discarded if for example a channel is saturated. The input range of the ATWD is 2 V, the different gain paths provide an effective sampling depth of 14 bit. To accommodate the delay in the trigger logic and to assure that the leading edge of the PMT waveform is well within the sampling time window a delay of 75 ns is required.

Since the readout of all ATWD channels takes up to 100 μs, a second ATWD chip is available to minimize dead time and also to provide redundancy. This allows to handle a second trigger which occurs after the 6.4 μs readout window of the first trigger. The transition to the second readout phase leads to a dead time of at least 50 ns and up to 22.5 μs if the first ATWD has not been read out at that time.

For longer recording time the fourth path of PMT signal is fed over a three-stage shaping amplifier into a fast ADC (fADC). It provides a continuous data stream of the PMT waveform at a sampling rate of 40 MHz (25 ns/sample). The fADC record is configured to be 6.4 μs long. The dynamic range of this device is limited to a few pe, though and bright signals can lead to saturation.

A local coincidence (LC) communication to neighboring DOMs is provided to reduce the noise of ~ 700 Hz, which arises mainly from electronic noise and the decay of ^{40}K in the glass. When a DOM triggers, it sends an LC "tag" to the neighboring DOMs. In turn, the readout of the ATWD is

---

[1] The first DOMs deployed have improper transformers, the PMT signal is distorted and shows signal droop and undershoot behavior. This problem can be corrected by software to some extent and has been eliminated in another revision of the HV board.

[2] The charge produced by one photo-electron corresponds to unit of 1 pe, it depends on the high voltage setting and amplification of the PMT. Given calibration records, it is a uniform measure across different modules.

only launched when an LC "tag" arrives from a neighboring DOM within a certain time window (currently 1 μs). This tag tells that another DOM in the LC chain, which can span across several DOMs, has triggered. These events are much more likely to originate from a particle than from noise and produce an event rate of ~ 10 Hz.

There are different LC operation modes. In hard local coincidence only signals with an LC "tag" are digitized and stored. This might introduce a bias in the energy reconstruction, because the charge contribution from isolated hit DOMs is omitted. In soft local coincidence mode LC tagged signals are digitized and for un-tagged signals the ATWD information is discarded. Only a coarse charge-stamp formed from the highest fADC sample and the corresponding time-stamp will be stored. This is the standard operation mode for IceCube. Self local coincidence mode uses the MPE discriminator launch to detect a bright signal. The ATWD charge samples are then digitized, regardless of LC "tags" from neighboring DOMs.

The oscillator provides a local clock with a very good short term stability over a couple of minutes. It oscillates at 20 MHz and the frequency is doubled inside the FPGA. It drives the fADC and clock counters, which are used to time-stamp all events. The clock counter provides a coarse time-stamp every 25 ns. Since the ATWD is launched on a clock transition, it provides a time measure for the edge of the first ATWD sample. A much better time resolution is obtained after post-processing the waveform, allowing to determine the offset within a certain readout bin.

The power supply and communication logic circuit is located in the upper right of the block diagram. It provides filters to extract the modulated differential communication and timing signals from the high voltage power connection. Additionally, several DC-DC converters provide different voltages required by the mainboard components.

An on-board LED emitting ultraviolet light can be used for the calibration of the PMT. The amplitude of the LED pulser is adjustable from a fraction of a pe to more than ten pe. The light is scattered inside the glass sphere and reaches the photocathode. Another source for calibration purposes is an electric pulser which can be coupled into the PMT signal path. This is used as a reference signal source to calibrate the ATWD and discriminator thresholds.

A fourth channel of the ATWD, which is driven by an analog multiplexer, permits precise measurement from eight signal sources. For example, it can be used to calibrate the ATWD sampling frequency by recording the local oscillator signal, or to monitor the on-board or flasher board LED currents to time-stamp light signals. In addition there are two serial ADCs which monitor 24 voltages in the DOM which are used for debugging and quality control (Monitor&Control element in Figure 4.4)

The FPGA and CPLD (complex programmable logic device) provide much of the logic to control and interface the hardware components (see Figure 4.4). The FPGA firmware contains multiple state machines for trigger logic, ATWD readout, hit record building, rate counting and data compression. For example, the data stream is reduced by using a delta compression algorithm, which only transmits the difference between two succeeding readout samples. If the changes are small, shorter bit representations can be used. The CPLD provides interfaces to hardware components, e.g. the flasher board, high-voltage generator, memory, DACs and ADCs. In particular, it drives those components which are needed at start-up, as the FPGA is volatile and needs to be loaded with firmware.

A RISC CPU integrated on the same die as the FPGA is running higher level software. Different software and firmware applications are running for different tasks like data acquisition, testing, and verification. The high level software provides a hardware access layer to interface the functionality of the FPGA and CPLD and implements the custom communication protocol. These functionalities are used by high level data acquisition programs which communicate with the DOMHub server software at the surface. This way a DOM buried deep in the ice can act as a basic terminal to which one can log in from any computer, even if located in the northern hemisphere.

The Digital Optical Module Readout (DOR) Card

The DOR card is a custom made interface card between up to eight DOMs and the DOMHub computer. It provides power management for the DOM, communications and data transmission, time calibration and a PCI bus interface to the DOMHub computer. Typically, eight DOR cards are installed in each DOMHub at the surface. A power supply in the DOMHub is connected to each DOR card to provide power for the DOMs. The DOR card communicates with the DOMs in half-duplex mode and is constantly polling the DOM for data. Most of the communication functionality of the mainboard is mirrored in the DOR card, which is important for the time calibration routine described below. The communication interface over the twisted pair connection provides a data rate of up to 45 Kbytes/s.

A dedicated Linux Kernel driver exposes the higher level configuration, control, and communication functions of the DOR card to rest of the surface DAQ software.

4.1.2 Production and Test of the Digital Optical Module

DOMs are integrated and tested at three production sites: University of Wisconsin – Madison (USA), DESY Zeuthen (Germany), and University of Stockholm (Sweden). Each site receives DOM sub-components (circuit boards, PMT, etc.) ready for assembly. After integration, DOMs are subjected to a Final Acceptance Test (FAT) to ensure that only fully functional modules are shipped to South Pole [75]. On site the modules are tested again in a short test cycle before the deployment. Since I was responsible for the production and testing of DOMs in Zeuthen for one year during my work for this thesis, a summary of the production and testing procedures are given in the following sections.

DOM Assembly

DOMs are assembled by technicians following an established procedure:

1. the PMT neck is covered with a molded plastic collar to provide a base for installation of the circuit board stack;
2. it is placed into the lower hemisphere of the glass pressure vessel along with the magnetic shield and the RTV gel, properly mixed and degassed;
3. this sub-assembly is fixed for 24 hours in a jig until the gel is hard cured;
4. the HV divider base is soldered onto the PMT connectors;
5. the PCB stack (delay board, mainboard, HV control board, and flasher board) is installed;
6. the penetrator cable assembly is soldered to the mainboard;
7. the sphere is evacuated and back-filled with dry nitrogen to a pressure of 0.5 atm and sealed;
8. DOMs passing the final acceptance test (FAT) are harnessed with a suspension for the attachment to the main cable;
9. finally, DOMs are packed and shipped to South Pole.

All components, as well as the different production steps are recorded in a database. A custom software allows technicians to easily insert the assembly steps and query the database for information on individual modules. Test and calibration results are also stored in the database. For example, this allows to track calibration results from different batches of PMTs and to study long term behavior of hardware test results. During my work for the DOM production and testing, part of my activity was to design, develop and roll out the database applications at all three production and test sites. The result is an improved tracking and stock keeping database of DOMs and components, which is available throughout the lifetime of the detector.

Final Acceptance Test

After assembly each DOM is tested to find failing or poorly operating units and to obtain optical sensitivity calibration information. The Final Acceptance Test (FAT) is performed in a Dark Freezer Laboratory (DFL) at each production site. A sketch of a DFL and its instrumentation is shown in Figure 4.5. The DAQ system is similar to systems at South Pole. DOMs are connected via quad cables to DOR cards installed in a DOMHub computer. The DOMHub service board (DSB) is connected to a GPS unit which provides the master clock. The local coincidence connections are similar to a full string installation. An electrical filter box emulates a cable length of $\sim 3\,\mathrm{km}$.

DOM test stations are arranged on shelves inside the DFL. Each DOM is placed on a cylinder clad with a reflective foil on the inside to evenly illuminate the DOM. Three light sources located outside of the DFL are used to run different tests: a 405 nm diode laser for time resolution tests, a monochromator-tuned quartz tungsten halogen (QTH) lamp for optical sensitivity measurements in the wavelength range 300-400 nm, and an LED pulser for measurements of the linearity behavior. The filter-wheel attenuator regulates the light intensity for each source. The setup of the optical system is arranged in a box outside the DFL. Light is distributed to stations via optical fibers. In the DFL the light is coupled into the DOM station using mirrors and a diffuser to distribute light evenly inside the cylinder. The stations are calibrated on a regular basis to account for station to station variations with a PMT of the same type as is used in the DOMs.

Inside the optical box there is a reference PMT (XP2020), which is read out using a DOM mainboard. Optical sensitivity and linearity behavior is obtained with respect to the readout of this device. An electric pulser is used to drive the LED and the laser, it is coupled to another DOM mainboard in order to synchronize signals with the light signals in offline processing.

Each FAT lasts approximately 2 weeks during which DOMs experience

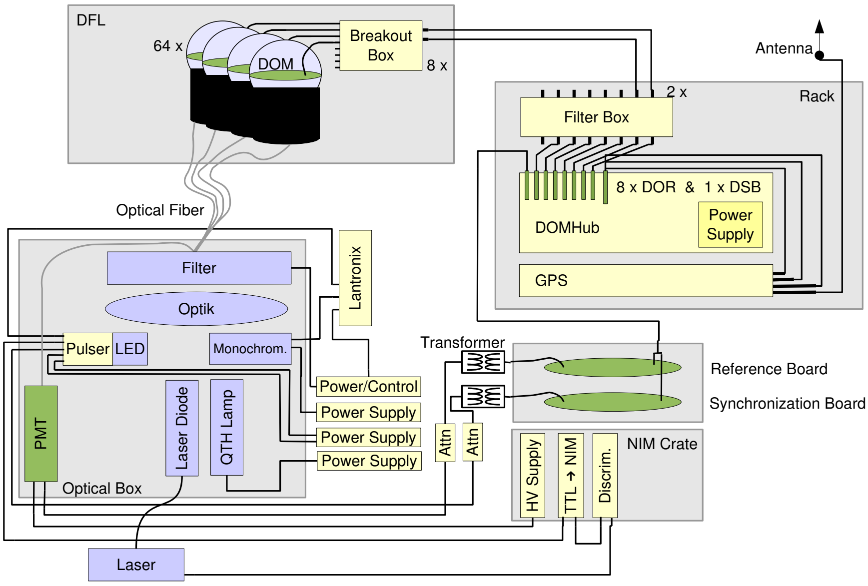

Figure 4.5: Schematic view of the Dark Freezer Laboratory (DFL). DOMs are located inside a dark freezer and connected to a DOMHub computer. Artificial light sources allow extensive tests and calibration of newly produced DOMs.

temperature cycles over the range[3] from −45 °C to +25 °C. After each temperature change the following test series is performed:

1. execution of the Simple Test Framework (STF), which runs on the DOM to test the basic functionality of the electronic components; among the 30 and more tests are for example tests that check the stability of the HV generator, the LEDs on the mainboard and flasher board, and the ATWD performance;

2. test of the local coincidence connection between DOMs;

3. calibration of ATWDs and PMT (see Section 4.1.3);

3. the rate count of the DOMs is recorded, while the QTH lamp is operated and the monochromator is driven to sweep over different wavelength, at different filter settings, in order to obtain the optical sensitivity;

4. for time resolution studies ATWD waveforms are recorded using the TESTDAQ application — this operation mode is similar to the DAQ system at South Pole;

5. for linearity tests of the PMTs the pulsed LED is operated in conjunction with different filter settings and waveforms are recorded;

6. dark noise rates are monitored for several hours.

Finally, DOMs are soaked at −45 °C for at least 180 hours, while the dark noise rates are recorded permanently. During temperature transitions hundreds of power cycles of the DOMs are performed.

Final Acceptance Test Results

Each DOM must pass all tests. If there are failures, components are replaced and the module is tested in another FAT. The test requirements are, for example: no STF failures critical for operation, no power and communication failure, stable PMT gain calibration, better than 5% relative error and no outliers in time resolution and sensitivity measurements. The performance is very good, less than $\sim 1\%$ of all components are non-confirming material.

---

[3] in the US DOMs are tested down to −55 °C

Dark Noise Figure 4.6 shows the dark noise rate of a DOM over many hours. It is stable around 2.7 kHz, which is well below the test criteria of 3.5 kHz. The rate is higher than in ice, due to environmental influences and the fact that light transmission from glass to air is much worse than from glass to gel or from glass to ice. Thus, light produced in the glass sphere from the decay of ^{40}K is trapped inside the DOM, if it is surrounded by air. At low temperatures the noise rate in ice is less than 700 Hz. This is important to detect galactic supernovae events that can be observed by an overall rate increase. Also in neutrino events, which last only microseconds, the number of noise hits is negligible.

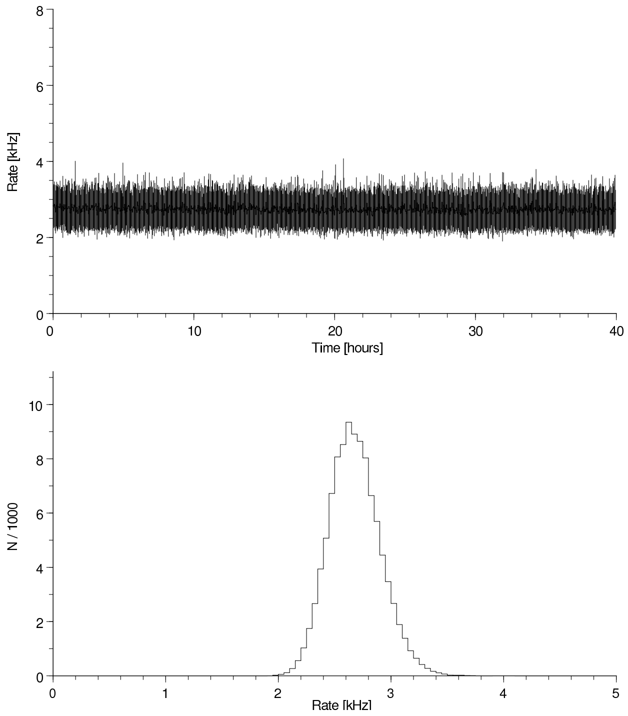

Figure 4.6: TOP: Dark noise rate recording over several hours for one DOM. BOTTOM: The projection of the rates to the ordinate. The mean dark noise rate for this DOM is ~ 2.7 kHz.

Optical Sensitivity A typical sensitivity measurement relative to a reference PMT performed during a FAT is shown in Figure 4.7. The wavelength band spans from 340 nm to 400 nm, covering the ultraviolet spectrum of the Cherenkov light. The detection efficiency saturates around 400 nm. A few DOMs have been calibrated absolutely and are also deployed in the ice [8]. They can be used as a reference device to obtain optical sensitivities of other deployed modules, and in combination with calibrated light sources, they offer a great opportunity to calibrate the energy reconstruction performance of the detector.

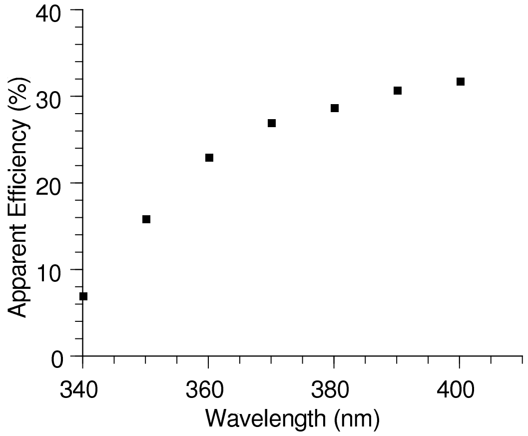

Figure 4.7: Optical sensitivity as a function of wavelength. The sensitivity is obtained by computing ratios between the DOM signal rate and a reference PMT rate.

Time Resolution Figure 4.8 depicts a typical result from a FAT time resolution measurement. The recorded arrival times of light pulses with respect to a reference trigger time are shown in a histogram. The width of the distribution is used as a measure for the time resolution. It should be less than 3 ns. The mean value is shifted due to light travel times and delays in the readout system. The tails appear due to pre-, late-, and after-pulses [8].

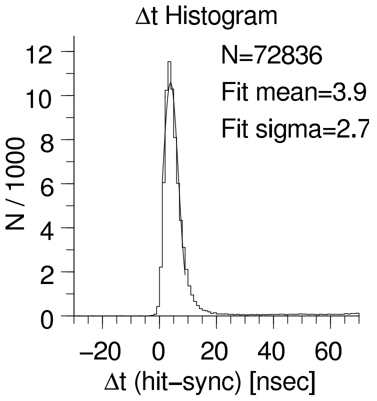

Figure 4.8: Histogram of light arrival times obtained in FAT time resolution runs. DOM hits are stimulated with an external laser. The hit times are recorded with respect to the laser trigger time. The offset reflects light travel and readout delay times. The standard deviation of the gaussian fit gives a measure of the time resolution of the module.

Linearity In Figure 4.9 the linearity measurement of a bare PMT[4] is shown. The plot is based on data presented in [8]. It shows the measured PMT current versus the ideal current I_0 which corresponds to the number of pe per pulse duration emitted by the light source. The pe rates are converted to ideal currents by multiplication with the SPE charge for a given gain. For signals up to ~ 50 mA, which corresponds to ~ 30 pe/ns, the response of the DOM is proportional to the light input. For brighter signals the response is not proportional anymore and saturates for pulses with more than 150 mA (300 pe/ns). This is crucial for bright high energetic neutrino events, as the reconstructed energy might be underestimated due to the lower charge response. Even a 1 PeV cascade in 120 m distance yields on average more than 300 pe/ns. In addition, the pulse width changes dramatically in case of large signals and after-pulses due to ionization of residual gases by electrons accelerated between the dynodes are prominent. All these non-linearity effects need to be taken into account in the energy reconstruction.

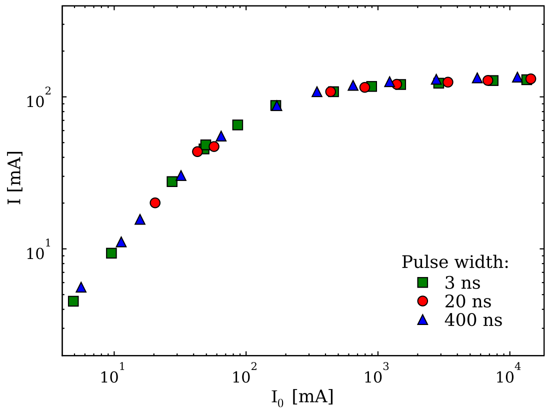

Figure 4.9: The bare PMT current response as a function of the ideal current expected from a linear behavior. The latter is derived from different illumination levels and the charge response of the PMT at a given gain. The illumination levels are given by different filters used as attenuators in the light path. The PMT is interrogated using light pulses of different duration.

4.1.3 Calibration

There are two different calibrations necessary to obtain accurate and comparable measurements throughout the detector. Time calibration is performed

---

[4] Currently, there are is no qualified analysis of linearity measurements of integrated DOMs available.

regularly almost every second. It is performed automatically by subsystems of the DOM and DOR card. The calibration of the front-end electronics and PMT gain is performed on request at least once per month.

Time Calibration

The method used for time calibration is called Reciprocal Active Pulsing Time Calibration (RAPcal) [129]. It determines the relative times of the clocks at the surface and in the DOMs, including the one-way signal transmission time, which allows to map surface time to DOM time. The surface clock is shared across all DOR cards. In order to determine the count and phase of the DOM's local oscillator relative to the master clock, a time-stamped bipolar-pulse is sent from the DOR card to the DOM. After receiving the pulse and after a fixed delay, the DOM sends a pulse of the same shape back to the surface. From the transmitted and received times of the round trip one can calculate the one-way time. The required accuracy is obtained by having the same electronic circuits on both communication sides. As the granularity of the clock is 50 ns, the time-calibration algorithm digitizes the waveform to find the offset in a time bin, for example by fitting the leading edge and using the baseline crossing as a reference point.

The performance of the time-calibration is very good, as can be seen in the time-resolution tests mentioned above. The time resolution of deployed DOMs can also be measured using muons from air showers or flasher board signals. All methods show that on average the time resolution is better than 2 ns [7].

Front-End and PMT Gain Calibration

In order to convert the digital readout to waveforms measured in voltage and time a dedicated software called DOMCAL runs on the DOM. Since the calibration constants do not change much over time, it only needs to be executed about once per month. The calibration comprises the following steps [88]:

1. ADC count to voltage calibration for each ATWD bin using a changing bias to change the baseline of the ATWD;

2. amplifier calibration for each gain path using the on-board pulser, which produces pulses of known amplitude;

3. calibration of the ATWD sample frequency with a waveform from the oscillator multiplexed to the ATWD;

4. PMT gain calibration, the on-board LED is used to interrogate the PMT and SPE waveforms are captured at different voltages to record a charge spectrum which reveals the gain to voltage calibration of the PMT (Figure 4.10);

5. finally, the on-board LED is used to measure the signal transit time, in particular the transit time in the PMT.

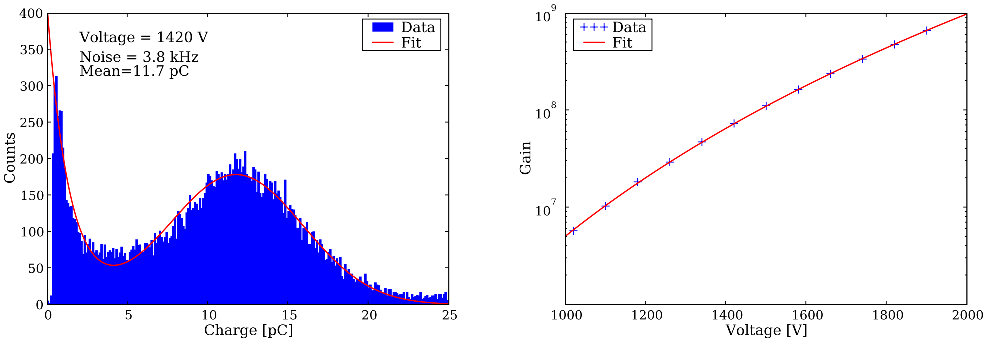

Figure 4.10: The left figure shows the SPE charge spectrum obtained using the on-board LED flashing at below 1 pe to interrogate the PMT and recording the waveform response with the ATWD. Filling a histogram with the charge integral of the ATWD waveform from many hits results in a spectrum with a peak around the charge which corresponds to 1 pe, here it is 11.7 pC. The pedestal on the left originates from noise but also from back-scattered photoelectrons at the first dynode, which results in signals with less charge [49]. Dividing the mean SPE charge by the charge of an electron reveals the gain. The plot on the right shows the gain obtained from fitting several SPE spectra as a function of the PMT's high-voltage. A linear regression on a double-logarithmic scale yields the voltage to gain calibration constants.

The calibration results are stored in a database and are available for offline processing and filtering of the data.

4.2 Ice Properties

IceCube uses the natural Antarctic glacier of roughly 3 km height as a detection medium. It is crucial to understand how neutrinos and charged particles propagate through this medium – this has been addressed in the last Chapter. In addition, it is important to know how the Cherenkov light is influenced by the ice, as it has a direct impact on the reconstruction of events. The propagation of photons depends on the optical properties of the medium, in particular on the velocity of light, the absorption, and scattering cross sections. Glacial ice is optically inhomogeneous, with strong variations in depth. The concentration of air bubbles changes due to pressure and temperature variations. Dust deposits vary due to climatological changes during the thousands of years, over which the glacier has grown[5]. Varying dust concentrations are assumed to be arranged in horizontal layers and the modeling of the optical properties of the ice is therefore parameterized as functions of the depth.

The speed of light is governed by the group refractive index n_g, while transmission and scattering depend on the phase velocity and its index of refraction n_p [120]. In the description of the ice they are assumed to be constant throughout the glacier.

The strength of absorption is often described by the absorption length λ_a, the distance at which the flux of photons propagating through the medium drops to 1/e. The reciprocal of this length is the absorption coefficient, also called absorptivity. Absorption of visible and near UV photons is due to electronic and molecular excitation processes. In the wavelength range from 200 nm to 500 nm pure ice is extremely transparent and $\lambda_a \approx 100\,\mathrm{m}$. The main component causing absorption is dust [28].

Light is scattered by centers of very different types and sizes, whereby the main contribution is from mineral grains in dust layers. This effect can be well described by Mie scattering theory [111]. The scattering length λ_s is of the order of 1 m, however, it is strongly forward peaked. The mean cosine of the scattering angle has been determined in simulations to be $\langle\cos\theta\rangle = 0.94$ [12]. It is convenient to introduce an effective scattering length, the length after which the initial photon direction is totally randomized:

$$\lambda_e = \frac{\lambda_s}{1 - \langle\cos\theta\rangle} \, .$$

For ice in the depths of the IceCube detector, $\lambda_e \approx 25\,\mathrm{m}$.

Figure 4.11 shows maps of optical scattering and absorption for deep South Pole ice. The left plot shows the effective scattering coefficient (λ_e^{-1}) as a function of depth and wavelength. The contribution from bubbles is shown as a shaded surface, which dominates at shallow depth. However, with increasing depth and pressure air bubbles become unstable and undergo a phase transition to clathrate hydrates which are trapped inside the ice molecules. At depths below 1400 m there are almost no air bubbles left. The wavelength dependence is modeled with a power law. In the right plot the absorptivity (λ_a^{-1}) as a function of depth and wavelength is shown. Two

---

[5] Actually, these changes can be used to track climate changes and events like giant volcanic eruptions on the Earth over a long time.

components contribute to the absorptivity, an exponential term describes the pure ice contribution (shaded surface), which dominates the wavelength band above 500 nm, the second component describes the contribution from dust impurities.

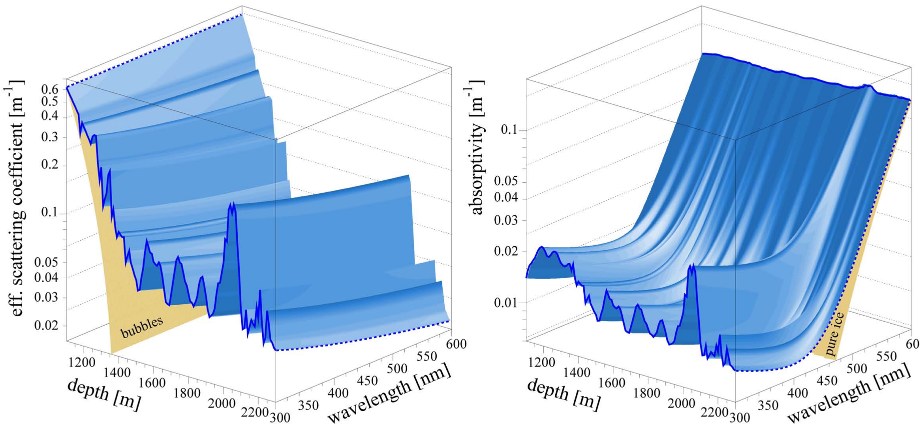

Figure 4.11: The plot shows the effective scattering length (left) and absorption (right) coefficients with varying depth and wavelength. See text for description. Picture taken from [12].

The strong variations in depth of both coefficients are clearly correlated and stem from different dust concentrations in dust layers. These dust layers have been measured using the in-situ light sources deployed with optical modules of the Amanda-II detector. During the deployment of the IceCube DOMs a device called "dust-logger" is lowered in some of the holes and allows a precise measurement $\mathcal{O}(1\,\mathrm{cm})$ of the dust concentration versus depth [50]. A comparison of dust layer measurement from previous Amanda-II measurements and the new dust-logger data is shown in Figure 4.12. The most prominent dust peaks are labeled from A to D. In particular, the peak structure 'D' starting at a depth of ~ 2050 m (100 m below the detector center) has a strong impact on the Cherenkov light distribution emitted from particles. As mentioned above, the flasher-boards installed in each DOM are a powerful tool to characterize this in more detail. Also a dedicated calibrated light source has been installed, called the "Standard Candle" [90]. Both will be used to test the current modeling of the ice properties to a great detail. In particular it is anticipated that these light sources will provide valuable data to classify the effect of the hole ice. Due to the melting and refreezing of the ice in the bore holes, it is probably not as clear as the glacier. In the modeling of the ice for the detector simulation this is taken into account with increased scattering coefficients. However, the correct values in this domain are yet unknown.

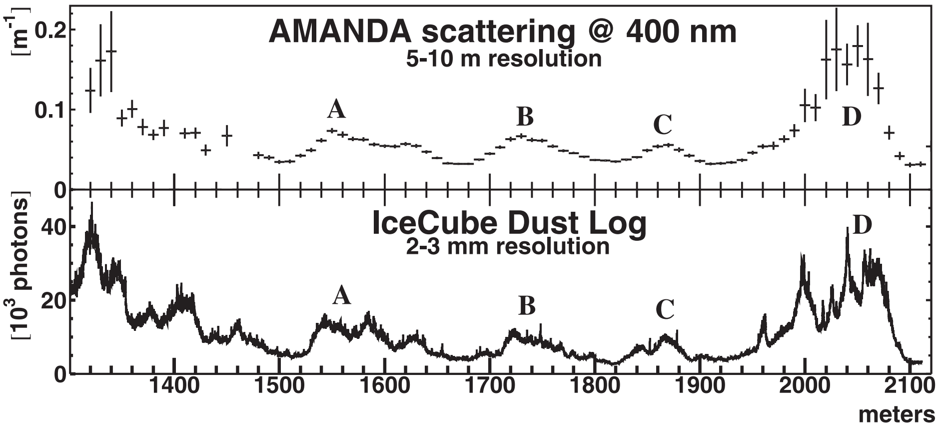

Figure 4.12: The upper plot shows the dust layer structure versus depth from measurements with in-situ light sources of the Amanda-II detector. The y-axis gives the effective scattering coefficient, which is correlated with the dust concentration. Below is the result with much improved resolution using the dust-logger device. The count of back-scattered photons, measured by this device is shown. It is proportional to the dust concentration in the ice. Picture taken from [9].

4.2.1 Light Propagation in Ice

The optical properties of the glacial ice govern the light intensity and arrival time profile of the Cherenkov photons. For the simulation one needs an accurate modeling of the processes involved. Since an analytic description of scattering is not possible [106] the photonics software was developed to perform a random walk simulation of light propagation in ice or water [112]. photonics is used for the simulation and recently also for the reconstruction of events in the IceCube detector. It uses a medium described by depth and wavelength dependent absorption and scattering coefficients. For IceCube the ice model described in the previous section is employed.

Due to the large number of photons emitted from a single particle, it is not possible to perform a dedicated ray tracing for each photon. photonics produces a set of photon flux density tables describing the evolution of the light field around a source in a cellular grid. In case of a Cherenkov light source, photons are injected from a single point in space according to the Cherenkov wavelength spectrum and angular emission profile. For simulation and reconstruction the photon flux tables are converted to the mean number of photons detected in each detector module, as well as the arrival time distribution of these photons. The source is specified by type (e.g. muon or cascade), location $\vec{r}_{\text{source}}$ and orientation θ, ϕ. The module by its spatial coordinates $\vec{r}_{\text{DOM}}$. In order to save disk space, the photon wavelength and arrival orientation are folded with the wavelength and angular acceptance of the detector modules. For the use in reconstructions, a multidimensional interpolation between the discrete coordinates used in the photon tracking is performed. Details can be found in [106].

The photon arrival time is a composite of the travel time of an unscattered photon, called geometrical time, and the time delay due to scattering. The geometrical time is given by $t_{\text{geo}} = \Delta x/c_g$, where Δx is the distance between the point of light emission and the sensor, and c_g is the group velocity of light in the medium. The delay time is governed by a stochastic process and the underlying probability distribution $P(\Delta t)$ is computed in the simulation. The probability distribution depends strongly on the distance between emitter and detector, as well as on the composition of the medium. Figure 4.13a shows a 2-dimensional plot of the delay time distribution for different distances obtained by querying the PHOTONICS tables using a cascade-like emitter at a depth of 1950 m. At short distances, the time distribution has a concise peak at very small delay times. However, with increasing distance, scattering becomes more important and the delay time distribution becomes wider and the most likely delay becomes larger. The right plot (b) shows the delay time distribution for a fixed distance of 100 m at different depths. The change in the distribution is caused by different dust concentrations in the ice layers. In particular, at $z = -100$ m, which corresponds to a depth of ~ 2050 m, the delay time distribution is widened dramatically. This is caused by the dense dust layer labeled with 'D' in Figure 4.12.

The evolution of the light distribution for a cascade-like emitter is shown in Figure 4.14. At different times after the cascade appeared, the mean number of photon-electrons is shown in the $x - z$ plane. The cascade is located at a depth of $z = -120$ m below the detector center, with direction pointing downward and an energy of 100 PeV. It is important to notice that PHOTONICS ignores the extension of the cascade in space and time. The plots on the left show the light distribution as obtained from PHOTONICS using a point-like cascade, whereas plots on the right are obtained using the simulation described in the Section 3.4.3 to take into account the longitudinal development of the shower.

The light distribution in the left plot after 20 ns (a) reflects the emission pattern used in PHOTONICS. Most of the light is emitted in the forward direction, in particular in the direction of the Cherenkov angle. The plot on

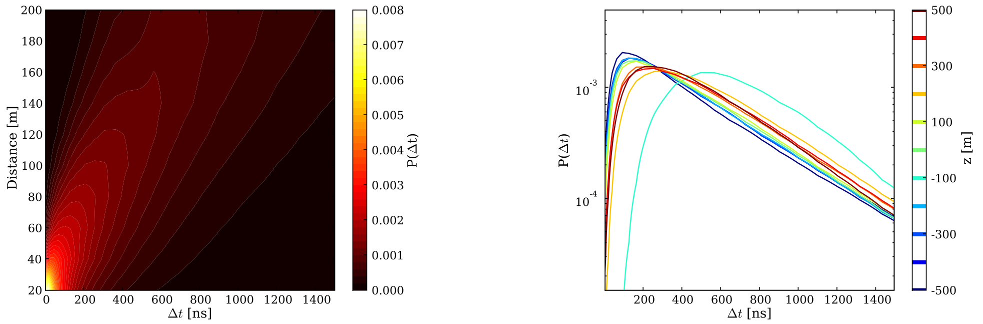

(a) Delay time probability versus distance for a cascade located at the center of the IceCube detector.

(b) Delay time distribution at 100 m horizontal distance in different depths (in detector coordinates)

Figure 4.13: Delay time distributions obtained from PHOTONICS simulations.

the right clearly shows the impact of the shower development. The emission pattern is stretched as a result of the overlay of multiple sub-cascades constituting the complete shower.

After 150 ns (b) the emission pattern is washed out due to scattering. For the point-like emitter, the distribution is almost isotropic and all directional information is lost. This is different in plot on the right, the longitudinal development of the cascade creates a light cone as can be expected from a moving particle.

Even at 300 ns (c) the light distribution in the plot on the right shows the influence of the cascade development, but starts to vanish. The distortions at the top of the light pattern in both plots are due to high dust concentrations at $z \approx -100$ m, which introduces some ambiguity in the interpretation of directional information of the light pattern. In particular, one could argue the cascade is pointing upwards, in both plots. This illustrates that it is hardly possible to reconstruct the direction of cascades.

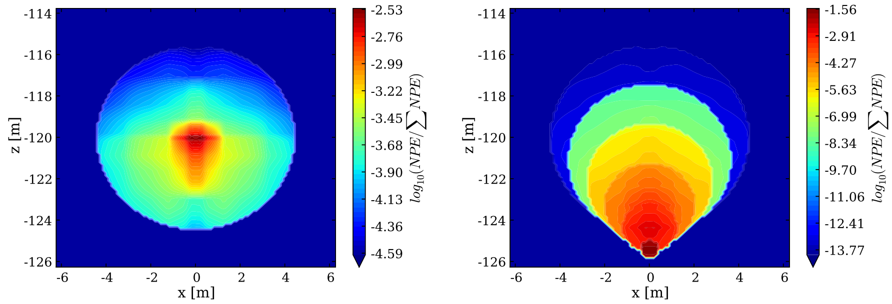

(a) Light distribution after 20 ns

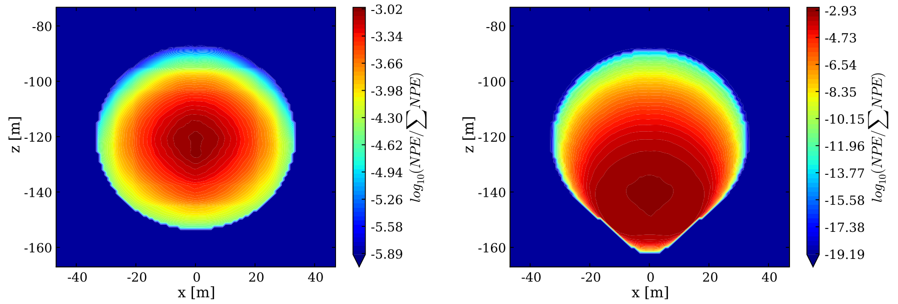

(b) Light distribution after 150 ns

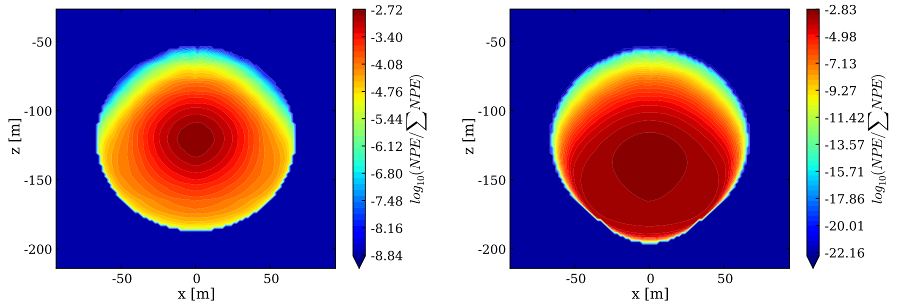

(c) Light distribution after 300 ns

Figure 4.14: Cherenkov light distribution after 20 ns (a), 150 ns (b) and 300 ns (c) for a 100 PeV cascade at a depth of $z = -120$ m pointing downward. The left plots are for point-like cascades as provided by PHOTONICS, the plots on the right are obtained taking the longitudinal development of the shower into account.

Chapter 5

Event Reconstruction

The IceCube detector records the light flux within the detector medium at fixed points given by the DOM positions. The result is a waveform of charge versus time related to space coordinates. This waveform is converted into hits and pulses which provide amplitudes measured in (photo-) electron charge (pe) and time information of the photons arriving at the cathode of the PMT (see Section 7.1 for details).

Based on these measurements, the reconstruction tries to find the best approximation to the particle which created the signals recorded throughout the detector. Depending on the type of analysis, different properties are important to reconstruct: of main interest are the event signature (track-like or cascade-like), energy, direction, and vertex location in space and time.

In an analysis one uses the event and reconstructed particle properties to obtain the optimal signal and background separation to either increase the significance of an observation or give the most stringent upper limit for an expected flux of neutrinos in absence of a signal.

Existing algorithms for cascade reconstructions are capable to reconstruct the vertex location and energy. If the vertex is within the fiducial volume of the detector both can be reconstructed precisely [100]. In particular the energy estimate of the parent neutrino is reliable[1]. Whereas it has a larger uncertainty in muon reconstruction, because the event is seldom fully contained within detector volume and energy losses along the track fluctuate. However, in contrast to muons, where the direction is reconstructible with an accuracy of up to 1° [9, 19], this information was not accessible at all for cascades. Due to the scattering of the light, the initial light emittance pattern of cascades is washed out after $\sim 25\,\mathrm{m}$. In Section 4.2.1 it was shown that the longitudinal development has an impact on the light distribution

---

[1] In neutral current interactions part of the energy is lost to the neutrino in the final state, in these events the energy deposit will not reflect the energy of the incident neutrino.

in the detector, which has not been taken into account in previous works. Based on this information, studies were performed to assess the possibility of the directional reconstruction of cascades in particular at ultra-high energies. Before this is presented in detail, the "first-guess" reconstruction algorithms applied in this analysis presented in the following chapters are described.

5.1 First-Guess Algorithms

First-guess algorithms are used to find approximations of event properties, which can be used to classify events as signal and background for a particular analysis. In addition, they often deliver seeds for the more sophisticated likelihood reconstructions. Ideally first-guess algorithms derive these properties analytically from the measured arrival times and signal amplitudes without much computation. This makes these algorithms suitable to be run on very large datasets and filter events which are of interest for a certain analysis and need to be studied further.

There are many different first-guess algorithms available [19], here only those are discussed which have been employed later in this analysis.

5.1.1 Line-Fit

The LINE-FIT algorithm is used to find an initial track on the basis of hit times with optional amplitude weighting. Ignoring the geometry of the Cherenkov light cone and the optical properties of the medium, one can assume that a light front perpendicular to a hypothetical track is propagating through the detector. If the track starts at $\vec{r}_0$ and moves with velocity $\vec{v}$, the position of module $\vec{r}_i$ hit at time t_i is given by $\vec{r}_i \approx \vec{r}_0 + \vec{v} t_i$. A linear regression yields estimates for $\vec{v}$ and $\vec{r}_0$:

$$\vec{v} = \frac{\mathrm{COV}(\vec{r}, t)}{\mathrm{VAR}(t)} \qquad \text{and} \qquad \vec{r}_0 = \langle \vec{r} \rangle - \vec{v} \langle t \rangle \tag{5.1}$$

where $\langle x \rangle$ denotes the mean of parameter x, $\mathrm{COV}(x, y)$ and $\mathrm{VAR}(x)$ are the covariance between x and y and the variance of x, respectively.

Since this estimate is based on a track hypothesis, it is a rather bad estimate for the cascade vertex and direction. This being said, it provides a powerful discriminator between track-like and cascade-like events. The mean speed of light propagating through the detector taking into account the direction of propagation is given by $\vec{v}$. Although the Cherenkov light is scattered and moves in all directions, the additional movement of the emitter is significant. In case of a muon the direction and speed of the emitted light is dominated by the muon's speed vector with a value around c. However, a cascade in a first approximation is almost static and the light is expanding almost isotropically. Hence, the mean speed of light approximated by $\vec{v}$ is nearly zero (see Figure 7.5 on Page 91). In other words, for track-like events, the hit times and module positions are linearly correlated, whereas they are much less linearly correlated for cascade-like events.

5.1.2 Tensor of Inertia

The Tensor of Inertia is a first-guess approximation to the topology of an event using the spacial distribution of hits. Based on the mechanical analogous, the tensor of inertia of an event is constructed using the observed number of hits n_i at a module $\vec{r}_i$ as mass points. The coordinates are defined with respect to the center of gravity (COG) of the mass distribution. The COG-coordinates and the tensor of inertia components are given by:

$$\mathrm{COG} = \sum_{i=1}^{N} n_i^w \, \vec{r}_i \qquad \text{and} \qquad I_{\alpha,\beta} = \sum_{i=1}^{N} n_i^w \left[\vec{r}_i^{\,2} \delta_{\alpha,\beta} - r_{i,\alpha} r_{i,\beta} \right], \tag{5.2}$$

where $\alpha, \beta = \{1, 2, 3\}$, and w is a weight which can be chosen arbitrarily. For example it can be set to 0 to use a unit mass for all modules. The three eigenvalues of the tensor yield the principal moments of inertia $I_i, i = \{1, 2, 3\}$, which correspond to the principal axes. The smallest eigenvalue corresponds to the longest axes, which approximates the direction of a track, the ambiguity of the direction along the axis is resolved by choosing the direction where the average hit time is latest. The ratio between the smallest eigenvalue and the sum of all can be used to determine the sphericity of the event. For a cascade-like event $I_i \approx I_j$ and $I_{\mathrm{min}}/(I_1 + I_2 + I_3) \approx 1/3$, whereas it is smaller for a more prolate hit distribution of track-like events.

5.2 Maximum Likelihood Reconstruction

Given the probability density function $p(x_i|\vec{a})$ of measured values x_i which constitute the measurement $\vec{x}$ and depend on some parameters $\vec{a}$, one can construct the likelihood function

$$\mathcal{L}\left(\vec{x}|\vec{a}\right) = \prod_i p(x_i|\vec{a}), \tag{5.3}$$

which provides a measure how likely the measurement $\vec{x}$ is, given the parameter set $\vec{a}$. In a maximum likelihood reconstruction one tries to find the optimal parameters of the measurement $\vec{x}$ by maximizing the likelihood function with respect to $\vec{a}$. In turn, these parameters determine the properties of the particle which created the measurement $\vec{x}$. Technically the optimization is performed using the logarithm of the likelihood function to reduce problems with numerical rounding errors and by minimizing the negative of $\log(\mathcal{L})$.

For example, in case of the track reconstruction, the probability density function (PDF) of the arrival time distribution of photons measured at an optical module is used. As mentioned earlier photons are deflected due to scattering, which causes a delay in the arrival time compared to the geometrical travel time t_{geo}, as it is shown in Figure 4.13. The arrival time distribution depends on the distance between the point of emission and the sensor $d = |\vec{r}_0 - \vec{r}_i|$, as well as on the number of photons emitted. This is directly related to the location, energy and orientation of the particle traveling through the detector. In the notation from above, the particle's parameters $\vec{a} = (\vec{r}_0, t_0, \phi, \theta, E_0)$ determine the value of the delay time PDF given the measured time x_i at the module location $\vec{r}_i$. It is important to notice that in this formalism, a single module can contribute with several times x_i. In previous works [19, 100] the arrival time distribution was parametrized using a gamma distribution, with parameters describing the medium properties like scattering and absorption[2]. It was fitted to arrival time distributions obtained from simulations. Varying the parameters of the gamma distribution one can also include the effects from different ice layers [122].

The arrival time distribution is determined mainly by the particle location and orientation, thus for the energy reconstruction another likelihood function is constructed. Again, using simulations one can parametrize the mean number of photons observed by an optical module as a function of distance and energy of the particle. Since the Poisson distribution governs the amount of hits in each module, it is used to construct the likelihood function for the energy reconstruction. In previous works it was based only on the distinction between hit and no-hit probabilities and did not take into account the full charge measurement in each module.

Current studies [110] show that the vertex resolution for cascades obtained including the the full waveform information into the likelihood description is about 10 m. The relative energy resolution is ~ 0.2 in the common logarithm of the energy .

---

[2] Within the collaboration this is known as the Pandel Function.

5.2.1 Direction Reconstruction

In the introduction it was discussed that a directional reconstruction for cascade-like events would allow a point-source analysis, which could not be performed until now. Since this is a strong deficiency compared to muon analyses, studies were performed to assess the possibility of a directional reconstruction for cascade-like events.

The arrival time distribution of a cascade obtained from simulations in previous works is based on the model of a point-like light source. This distribution depends on the cascade orientation, however at distances larger than the effective scattering length, the initial direction information is deteriorated. In a first attempt it was tried to exploit the available information by introducing an effective distance into existing reconstruction algorithms. The effective distance adds a term to the distance between the emitter and sensor which depends on the angle between the speed vector of the cascade $\vec{v}$ and the distance vector $\vec{d}$:

$$d_{\text{eff}} = \left|\vec{d}\right| + f(\varphi) \qquad \text{with} \qquad \varphi = \sphericalangle(\vec{d}, \vec{v}) \tag{5.4}$$

It reflects the fact that a module located in the forward direction of the cascade sees more light and the probability to observe unscattered light is higher, hence the cascade seems to be closer. In contrast to modules in the backward direction of the cascade, in this case light needs to be scattered more and thus the arrival time distribution looks like that of a cascade being located further away. The angular function has been determined from simulations. The method did not yield a sufficient direction information, because the reconstruction shifted the vertex of the cascade to compensate the effect of the effective distance term.

None of the existing algorithms take into account the longitudinal development of cascades in the underlying PDF of the likelihood function and an adaptation was not easy to accomplish. Therefore a new reconstruction algorithm was developed in a Toy-Monte-Carlo based on the PHOTONICS simulation.

Motivated by the fact that fluctuations of the measured arrival times, if not taken into account properly, could mitigate the likelihood description, the time t after which a certain amount of photons arrived, is used as the measured value x_i. This integration might iron out uncertainties due to electronic artifacts which are likely to exist in case of very bright events. The processes which determine the photon arrival times are Poisson processes, which means the time between two photons arriving at the photocathode is exponentially distributed and the number of photons recorded in a given time window is governed by the Poisson distribution. In this case, the waiting time

t for the occurrence of the k'th photon is distributed following the Erlang distribution [137, 143][3]:

$$f(t; k, \lambda) = \frac{\lambda^k t^{k-1} e^{-\lambda t}}{(k-1)!} \qquad \text{for } t > 0. \tag{5.5}$$

The parameter λ is associated with the rate at which events occur, it is given by k/t_k, where t_k is the time when the k'th photon arrived. The mean value of t_k is obtained from simulation using the integrated delay time distribution scaled by the expected mean number of detected photons, both provided by PHOTONICS. Using PHOTONICS directly avoids to introduce a parametrization of the delay time distribution[4]. In this formalism the energy of the particle has a strong impact on the likelihood function, as the number of photons emitted dictate the observation rate. The average rate parameter is related to both, attenuation and scattering processes. Because the simulation returns recorded photo-electrons, it also includes the process of the photon conversion to detected photo-electrons, however, this occurs on different time scales. In order to get a better agreement between the Erlang distribution and simulated arrival times, the shape parameter k is enhanced by the inverse of the quantum efficiency (QE) to adapt the parameters to that of the arrival time distribution at the DOM sphere: $k' = \mathrm{QE}^{-1} \cdot k$. The quantum efficiency is taken to be 20%, which is near to the average over all DOMs and incorporates also the attenuation effects of the glass and gel. A better approach would be a modeling of this enhancement parameter based on simulations. It will probably depend on the distance and could disentangle the scattering and attenuation influence on the rate parameter λ.

Figure 5.1 shows the distribution of the arrival times of the 10th photon for modules at different distances obtained from a simulation of 1000 identical events. The Erlang distribution with appropriate parameters is shown as a red line. The agreement between the simulation and the model is good and justifies the use of the Erlang distribution in the likelihood function (equation (5.3)).

The longitudinal development of cascades is taken into account in the same way as it is done in the simulation (Section 3.4.4). A single cascade is represented by a set of sub-cascades with an appropriate energy distribution and the mean arrival time t_k is derived from PHOTONICS using this model.

The spatial resolution, as well as the energy resolution are of the same performance as the existing algorithms. The aimed directional reconstruction with better than 10 ° could not be achieved in the available time. Although

---

[3] The Erlang distribution is a gamma distribution with an integer shape parameter k

[4] For this purpose the dedicated PHOTOREC interface is available.

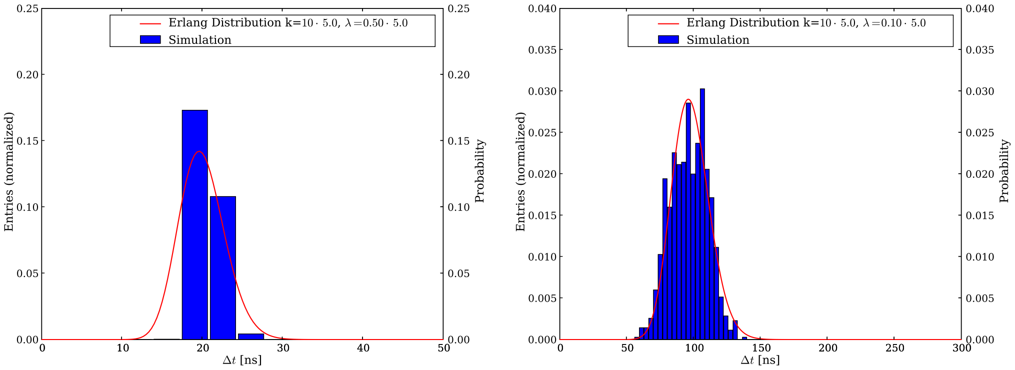

Figure 5.1: The plots show a histogram of simulated arrival times of the 10th photon at a module in 60 m (left) and 100 m (right) distance, emitted by a 1 PeV cascade. The Erlang distribution with a shape parameter enhanced by a factor of 5 and the rate parameter obtained from PHOTOREC is shown as the red line. It adequately describes the arrival time distribution in both cases.

at ultra-high energies the length of the cascade can reach hundreds of meters, the average resolution over an energy range from 10 PeV to 10 EeV is not better than 30 °. Figure 5.2 shows reduced likelihood contour plots in the zenith and azimuth angle parameter space for a cascade with 10 PeV energy. The cross marks the location of the true values and the dot that of the minimum of the contour plot. In many cases, as it is shown in the left plot, there is a distinct minimum in the vicinity of the true values. However, in this plot the other parameters are set to the true values and the location of the minimum changes substantially if they are not reconstructed precisely. This is illustrated in the right plot, where the vertex location was shifted by 10 m in each direction and the energy was set to 1 PeV. In addition the reduced likelihood surface shows several local minima which might trap a minimizer, though this problem could be solved technically with a sophisticated minimization algorithm and a good seed. The assessment of the directional reconstruction was ended at this point. Time limitations restricted further investigations to find reasons, why the minimization failed in so many cases, or to find selection criteria for events which could be reconstructed sufficiently well.

Future studies should try to exploit the capabilities of the “Deep-Core” extension, which provides a denser module spacing in the clear ice. With the denser spacing, the available information might improve the directional reconstruction. Although the volume of this extension is smaller and the sensitive energy range is much lower than considered in this work, the directional reconstruction at low energies should benefit from the methods derived in this work. In particular the application of the longitudinal development in both, simulation and reconstruction is important.

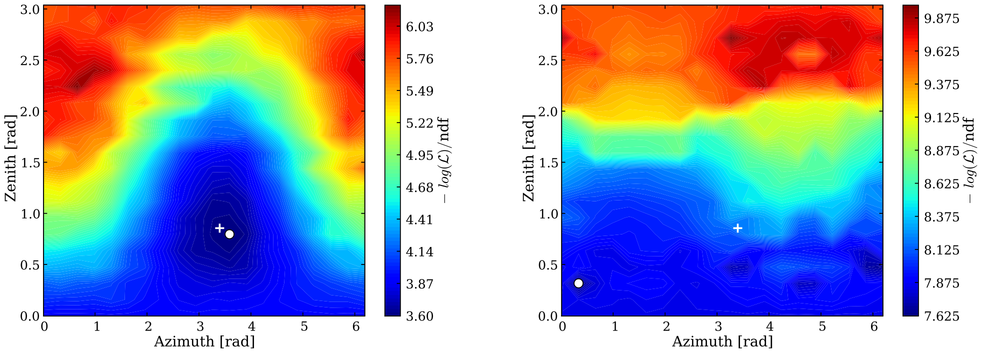

Figure 5.2: Reduced likelihood function in the azimuth-zenith parameter space of the direction reconstruction for a 10 PeV electromagnetic cascade. The true values of the parameters are marked by the cross, the minimum of the contour plot is indicated with the white dot. In the left picture the other parameters were set to the true values, whereas the right plot shows the reduced likelihood contour levels with slightly modified vertex and energy parameters.

Chapter 6

Simulation

In the following chapters a sensitivity study for the search of ultra-high energy electron-neutrino events in the 80-string IceCube detector is presented. As mentioned in the introduction and shown in Section 5.2.1, the directional reconstruction of electron-neutrino events was not successful until now. This inhibits the possibility of a point-source analysis and constrains to search for a diffuse signal in the data. The difficulty of a diffuse flux analysis is the estimation of the background from atmospheric muons, as it can not be measured in an off-source/on-source fashion. In this analysis the background estimation is solely based on Monte Carlo samples.

This chapter gives an overview of the simulated event samples used for the sensitivity study. Background and signal MC samples have been produced. The tools for the production of both event classes are described.

6.1 Simulation Overview

For the purpose of simulating data taken with the IceCube detector, the software framework IceSim is developed in a collaboration wide effort. The main program flow for the production of Monte Carlo events is outlined as depicted in Figure 6.1. At the beginning there is a particle generator producing particles depending on the user inputs. These particles are propagated through different media which are between the origin of the particle and the detector components. The detector response is simulated, including low level data processing like triggering algorithms. The resulting data stream is almost identical to data taken with the real data acquisition system of the detector.

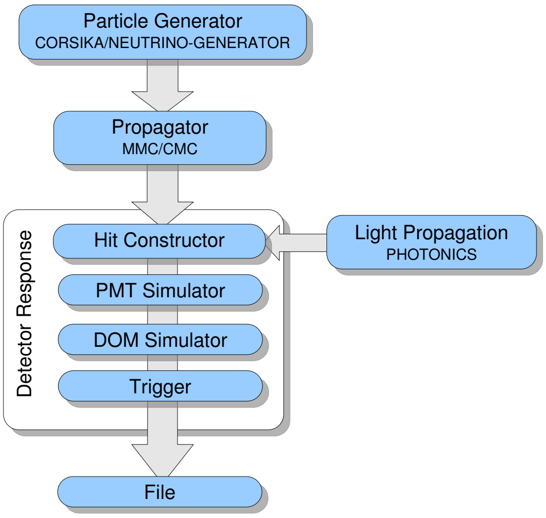

Figure 6.1: Simulation program flow with major components.

6.1.1 Atmospheric Muon Events

Muon background events have been generated with CORSIKA (Version 6.616) [76] as particle generator. CORSIKA performs a detailed simulation of extensive air showers, initiated by high energy cosmic particles penetrating the atmosphere of the Earth. It simulates interactions and decays of nuclei, hadrons, muons, electrons and photons of energies up to 10^{20} eV based on several interaction models. For this simulation GEISHA [56] and SYBILL [51, 58] have been used for the hadronic interactions. Electromagnetic interactions have been treated with EGS4 [115].

In the context of IceSim a slightly modified version of CORSIKA, called dCORSIKA [44, 87], is employed which contains specific adaptations for the simulation of muons penetrating the IceCube detector. Additionally, dCORSIKA allows to sample individual particles from a primary particle spectrum, in order to automatically resemble the composition of the cosmic ray flux. The particles from the air shower simulation are randomly distributed on a circular surface with a configurable radius above the detector. It is possible to omit muons with energies below a certain threshold.

Muon Propagation

Muons traveling through matter lose energy due to ionization, bremsstrahlung, photo-nuclear interactions, and pair production (Section 3.5). The simulation of these processes is performed using the Muon Monte Carlo (MMC [46]) module.

Energy losses above a certain threshold are treated stochastically and secondaries will be produced along the muon track. The Cherenkov light yield per meter muon track includes continuous losses which have energies below the threshold and are not simulated, though, they are taken into account in the muon range calculation.

Muon Bundles

There are three major background event classes which could mimic a cascade event: high energetic secondaries along a muon track, parallel muons, and coincident muons from independent air showers. High energetic secondaries and parallel muons are simulated correctly by the muon propagation and appear in the simulated event samples. Multiple parallel muons (muon bundles) can be miss-classified as signal events because they appear as a bright localized energy deposit which is typical for a cascade-like signature. These events are intrinsically produced in the air shower simulation. In particular the high energy air shower samples, which have been simulated with iron (proton) nuclei as primary particles, show peak muon multiplicities of more than 190,000 (130,000) muons with energies above 500 GeV in one event initiated by a primary particle with an energy of 10 EeV. On average the muon multiplicity ($E_\mu > 500\,\text{GeV}$) in air showers initiated by iron (proton) nuclei with energies between 10 PeV and 100 PeV is ~ 900 (400). This results in bright background events, with lots of triggered modules. As described in the following chapter, one can construct event observables which allow to identify these events.

Coincident muon events from independent air showers are not taken into account for this study. The contribution to the overall background rate is less than 1% [4] and probably negligible at energies above 1 PeV.

Prompt Muons from Charmed Particles

In air showers initiated by primaries with energies $\mathcal{O}(1\,\text{GeV})$, muons are produced by decays of relatively long-lived particles, such as π and K-mesons. With increasing energy, the probability increases that these particles interact before decaying. In these interactions and also in the first interaction of the primary particle short-lived hadrons are produced, mainly D-mesons which contain heavy charm quarks. These mesons decay directly into muons, which have a flatter (harder) energy spectrum. They are generally known as “prompt leptons” [48, 68]. However, there are large uncertainties in the modeling of these interactions and hence the flux predictions vary by orders of magnitude. The prompt muon contribution is closely related to the prompt flux of atmospheric neutrinos which has been discussed in Section 2.3.

The interaction models used in the CORSIKA simulation do not include these “prompt” components. The absence of this contribution has a negligible impact for development of the event selection, as long as high energy muons are present in the event samples, because they have the same event signature. However, it has to be accounted for in the calculation of the passing rates and error estimation.

6.1.2 Neutrino Events

For the simulation of neutrino events the NEUTRINO-GENERATOR module was used. It is a Monte Carlo event generator based on ANIS [64], which generates neutrinos, propagates them through the Earth and in a last step simulates the interaction within a specified volume around the detector. Neutral-current (NC) and charged-current (CC) interactions for all flavors, as well as resonant W^- production in $\bar{\nu}_e e^-$-scattering interactions are implemented. The cross-section data is stored in pre-calculated tables produced with CTEQ structure functions [102].

Neutrinos are generated in NEUTRINO-GENERATOR starting on the surface of the Earth and might be absorbed during their propagation to the detector in case of a CC interaction. In NC interactions, they are regenerated with lower energies. Scattering angles are not simulated for electron-neutrino events. When the neutrino enters the detector volume it is forced to interact and an event vertex is sampled along the neutrino trajectory in the detector. A corresponding interaction probability weight P_{int} is assigned to each event. The final event state consists of a leptonic and hadronic particle, which need to be further propagated through matter with the programs described below.

Typically, neutrino events are simulated with an energy spectrum following E^{-1}. For the development of the event selection the samples are re-weighted according to an assumed extraterrestrial signal flux. The same events are re-weighted to an atmospheric neutrino spectrum to calculate passing rates for the atmospheric neutrino background.

6.1.3 Simulation of Cascades

For this work, the Cascade Monte Carlo (CMC) module was developed to simulate the propagation of hadronic and electromagnetic cascades. This was necessary to overcome the limitations of the light propagation software, which treats showers only as point like light sources. In the simulation a single cascade is replaced by a list of sub-cascades attributed with energies according to the energy loss profile. At energies above 1 PeV the energy loss profile is simulated for individual showers, taking into account the LPM suppression effect. The simulation of cascades and physics processes involved are described in detail in Section 3.4.

6.1.4 Detector simulation

The detector simulation computes the signal response of the optical modules (OM) to photons emitted by charged particles, which have been propagated through the detector volume. In a first step the HIT-CONSTRUCTOR computes the time series of detected photo-electrons for each particle-OM combination. As described in Section 4.2.1, pre-calculated photon arrival time and density tables are provided by the PHOTONICS software. Following Poisson statistics, the number of observed photo-electrons is computed using the mean number of expected photo-electrons stored in these tables. For each photo-electron an arrival time is computed using $t = d/c_{\mathrm{ice}} + \Delta t$, where $d = |\vec{x}_{\mathrm{particle}} - \vec{x}_{\mathrm{OM}}|$ and Δt is a delay time drawn from the delay time distribution provided by PHOTONICS.

This procedure is extremely time consuming if the number of photo-electrons is large. Therefore the algorithm has been optimized in this work. If the number of photo-electrons exceeds the number of readout bins, the number of photo-electrons per readout bin is computed directly from the delay time distribution, rather than computing a delay time for each individual photo-electron. This limits the number of computational loops to the number of readout bins.

When the Monte Carlo time series of detected photo-electron has been computed, the PMT response for the photo-electrons is simulated using a measured photo-electron spectrum and waveform response of the PMT. This signal is then further modified by the DOMSIMULATOR, which applies the mainboard response function and low level trigger logic, like hard and soft local coincidence conditions. Also, electronic artifacts are simulated in this step, e.g. signal degradation due to improper transformers.

In a last step the global trigger is simulated. The trigger used for this work requires 8 triggered OMs within a time window of 5 μs. The format of the resulting data stream is identical to the filtered data stream from the detector data acquisition system, which allows equivalent high level processing for simulated and real data sets.

6.2 Weighting of Simulated Events

The simulated events are weighted to represent a certain flux ϕ. In case of a power law flux, the flux weight for an event with a primary particle of energy E_p is given by:

$$w_{\mathrm{flux}} = \frac{d\phi(E_p)}{dE_p\, dt\, d\Omega\, dA} = C \cdot E_p^{\gamma}\, \mathrm{GeV}^{-1}\, \mathrm{s}^{-1}\, \mathrm{sr}^{-1}\, \mathrm{cm}^{-2}\,, \tag{6.1}$$

where C is the flux normalization constant. In order to weight a certain amount of events accordingly one has to multiply the flux weight with the inverse of the simulated flux. The result is an event count in the detector volume which is caused by the primary particle sampled according to flux ϕ. The simulated flux weight is simply the number of events per simulated area, lifetime and simulated energy range. Except for the energy, particles are uniformly distributed in time, solid angle and area. Therefore only the energy range integration needs to take into account the simulated distribution and the integration is weighted with the fractional contribution of each particle's energy:

$$w_{\text{sim}} = \frac{N}{\int_T dt \int_\Omega d\Omega \int_A dA \int_{E_{\text{min}}}^{E_{\text{max}}} (E/E_p)^{\gamma'} \, dE \;\; \text{GeV}\,\text{s}\,\text{sr}\,\text{cm}^2}\,, \tag{6.2}$$

where N is the number of simulated events, A the simulation area, Ω the solid angle of the simulation, γ' is the power index of the simulated energy spectrum[1], with a range from E_{min} to E_{max}. The integration over time is not influenced by any simulation parameters, it is rather a scaling of the weight to a chosen lifetime T. The event weight is then given by the combination of equation 6.1 and 6.2:

$$w = w_{\text{flux}} \cdot w_{\text{sim}}^{-1}\,, \tag{6.3}$$

and yields the number of events in the time interval T, that are represented by the one simulated event, for which this weight is calculated. If not mentioned otherwise the integration over T is omitted, which is equal to normalizing to a lifetime of 1 s.

6.2.1 Weighting Neutrino Events

The NEUTRINO-GENERATOR forces neutrinos to interact inside the detector volume and assigns an interaction probability weight P_{int}. This weight needs to be taken into account by changing N in equation (6.2) to $N \cdot P_{\text{int}}$. Fortunately, NEUTRINO-GENERATOR provides the inverse flux weight w_{sim}^{-1} for each event including the interaction weight. However, it does not account for the number of events. This means one has to scale each weight with the inverse number of simulated events from all data files $1/N_{\text{total}}$.

6.2.2 Weighting Corsika Events

For CORSIKA events different weights have to be calculated, depending on the type of the simulated particle spectrum. In case of a mixed particle spectrum simulated with dCORSIKA the flux weight w_{flux} is calculated internally, as well as the corresponding simulation weight w_{sim} which includes the summation over the integrals of the individual energy spectra for each component i and the integral of the simulation area[2]. If particles are sampled according to the individual power spectra the resulting weight is given by:

$$w = w_{\text{flux}} \cdot w_{\text{sim}}^{-1} = \frac{\int_T dt \int_\Omega d\Omega \int_A dA \sum_i \int_{E_{min}}^{E_{max}} C_i \, E^{\gamma} \, dE}{N}\,, \tag{6.4}$$

---

[1] It is often useful to artificially increase the contribution from rare events to produce data efficiently and re-weight these events to the "normal" rate. For example, for a signal neutrino flux following an E^{-2} spectrum, one often simulates events following a harder E^{-1} spectrum, which is then re-weighted to E^{-2}.

[2] In the output of dCORSIKA "FLUXSUM" and "AREASUM" hold the corresponding numbers.

where C_i is the flux normalization constant for component i. As mentioned above, the result is a dimensionless count weight representing the event count of a single event in the lifetime T, which in this case is the same for all particles. In other words, the inverse of this weight yields the lifetime of a file that contains N events. The combination of files is done by scaling the weights with the inverse of the number of files $1/N_{\text{files}}$.

In case of simulating individual components in distinct data files and combining them afterwards, the weights are calculated according to equation (6.1) and equation (6.2). As described below, proton and iron samples have been simulated following an E^{-1} spectrum. In this case the flux integral yields:

$$\int_{E_{\min}}^{E_{\max}} (E/E_p)^{-1}\, dE = E_p \cdot \log(E_{\max}/E_{\min})\,. \tag{6.5}$$

The detector volume in the simulation is defined as a cylinder with radius $r = R$ and height $h = 2 \cdot r$. The area and solid angle integral is then given by:

$$\int_{\Omega} d\Omega \int_{A} dA = \pi^2 r(r+h)\,. \tag{6.6}$$

6.2.3 Error of Summed Weights

For a set of n weighted events, the total number of events is given by:

$$N = \sum_{i=1}^{n} w_i\,, \tag{6.7}$$

where w_i is the weight of event i. Applying error propagation under the assumption of Poisson distributed event counts, the variance of N is given by [39]:

$$\sigma_N^2 = \sum_{i=1}^{n} w_i^2\,. \tag{6.8}$$

The error bars shown in histograms are the square root of this variance.

6.3 Simulated Event Samples

This Section gives an overview of the simulated event samples that have been used for the sensitivity study. They consist of atmospheric muon events and electron neutrino events.

6.3.1 Atmospheric Muon events

Two different CORSIKA background event sets have been used. One is a regular background set provided by the collaboration wide simulation effort, in which primary particles are sampled according to the Poly-Gonato cosmic ray spectrum

[80] starting at energies of 600 GeV. The data set consists of 300 files, each corresponding to a lifetime of 2 s and a total of $\sim 10^6$ events. All simulation modules have been used with standard settings. Due to the steeply falling flux, the highest energy of a primary particle in this data set is only 142 PeV. Simulating the full background spectrum to obtain a reasonable number of extremely high energy events results in a tremendous amount of data and is almost impossible if one does not artificially change the power law index and reweight events accordingly. In addition, there is the problem that the Poly-Gonato model does not include an extra-galactic component and relies on elements heavier than iron. These elements contribute significantly to the cosmic ray spectrum at energies above a few PeV, however, they cannot be simulated with CORSIKA. Therefore, the Poly-Gonato model is only adequate at energies below 100 PeV [139, 144].

To overcome both problems, a pure proton and a pure iron CORSIKA sample have been generated following an E^{-1} spectrum in the energy range from 10 TeV to 10 EeV, which are re-weighted according to the 2-Component model presented in [67]. This empirical cosmic ray spectrum model is based on proton and iron nuclei only. The proton component is dominant up to the knee at $E_{\text{knee,H}} = 4.1\,\text{PeV}$, when it starts decreasing. The iron component has a smaller contribution below the proton knee, but due to a rigidity dependent cut-off at $E_{\text{knee,Fe}} = 26 \times E_{\text{knee,H}}$ it is dominating at higher energies. The weighting is performed as described above, where the flux weights $w_{flux,j}$ for $j = \{\text{H}, \text{Fe}\}$ are calculated as:

$$w_{\text{flux},j} = C_j \cdot \begin{cases} E_p^{\gamma_{1,j}} & E_p < E_{\text{knee},j} \\ E_p^{\gamma_{2,j}} \cdot E_{\text{knee}}^{(}\gamma_{1,j} - \gamma_{2,j} & E_p \geq E_{\text{knee},j} \end{cases}, \tag{6.9}$$

where C_j is the flux normalization, $\gamma_{(1,2),j}$ are the power law indices below and above the knee, and E_p the energy of the primary particle. The parameters are given in Table 6.1. Since the normalization constant is given at $E_{\text{knee,H}}$, it necessary to express the energies in units of $E_{\text{knee,H}}$ for the calculation of the weights.

Parameter	Proton (H)	Iron (Fe)
E_{knee} [PeV]	4.1	$26 \cdot 4.1$
C [$\text{GeV}^{-1}\text{m}^{-2}\text{s}^{-1}\text{sr}^{-1}$]	$3.9 \cdot 10^{-14}$	$1.9 \cdot 10^{-14}$
γ_1	-2.67	-2.69
γ_2	-3.39	-3.1

Table 6.1: Parameters of Glasstetter 2-Component model [67]

In order to speed up the simulation, only particles with energies above 500 GeV for muons and hadrons, and above 2 TeV for electrons and gammas, are further treated with in the air shower simulation. In addition, only muons above 500 GeV are included in the propagation and detector simulation. The propagation has been performed using MMC with a slightly modified configuration to use less interpolation points in the numerical integration of energy losses, with the drawback of larger errors (a table in Appendix B summarizes the module settings). However, a comparison between the regular CORSIKA data set and this high energy data set shows reasonable agreement, as presented below. In total, 120.000 proton and iron events have been simulated.

6.3.2 Electron Neutrino Events

For this study 100.000 electron neutrino events with equal numbers of ν_e and $\bar{\nu}_e$ have been generated in the energy range from 10 TeV to 10 EeV following an energy spectrum $\phi(E) \propto E^{-1}$. The secondary cascades have been propagated with CMC including a full simulation of the energy loss profile of electromagnetic cascades for energies above 1 PeV. A summary of the configuration parameters can be found in Appendix B.

For the event selection analysis the events have been re-weighted to a flux of $\phi(E_{\nu_e}) = 1 \cdot 10^{-7} E_{\nu_e}^{-2}\,\mathrm{GeV\,s^{-1}\,sr^{-1}\,cm^{-2}}$ following the procedure described above. For the analysis of passing rates and sensitivities, the events are re-weighted to different atmospheric and extraterrestrial electron neutrino fluxes.

Chapter 7

Sensitivity Analysis

The aim of this study is to develop an efficient selection of high energy electron neutrino events that are present in a $\sim 10^9$ times higher background of atmospheric muons produced in air showers. The filtering is based on the classification of cascade-like and track-like events. In this sense all cascade-like events are considered as signal. The original target energy region lies between 1 PeV and 10 EeV, where the background from atmospheric neutrino events is expected to be lower than hypothetic extraterrestrial neutrino fluxes. However, the filtering is developed including events from lower energies, therefore a final selection of extraterrestrial events would be based on an energy cut, applied to the surviving cascade-like events.

This Chapter describes the data filtering in detail. First the data processing procedure is summarized. Based on the resulting events, filter cuts are developed to reduce the background. Finally an event classification scheme is developed, which allows to select cascade-like events with a very good efficiency.

7.1 Data Processing

The different processing steps are listed in the following. Some of the tools and procedures applied have been introduced in the previous chapters. Here, only a short description is given with references to the corresponding sections. The data flow in the processing is depicted in Figure 7.1.

Cleaning

If the cleaning is performed, it would consist of removing dead and mis-behaving OMs from simulated events and experimental data in order to have an equivalent data basis. For this study events have been used simulated with nominal operating OMs, which makes the cleaning procedure obsolete.

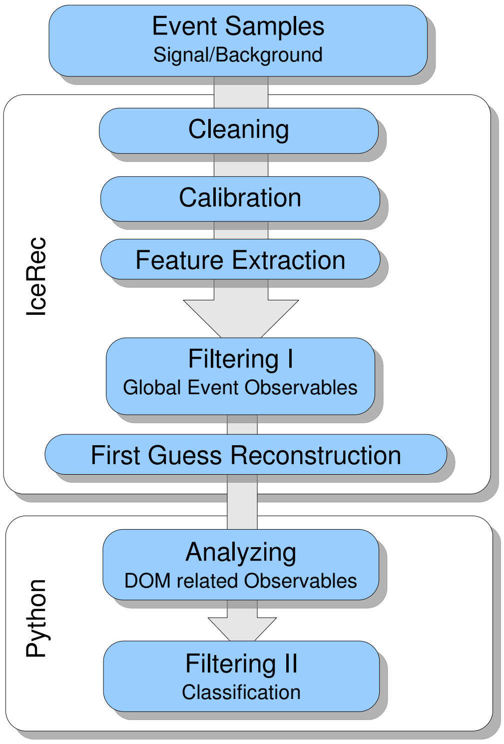

Figure 7.1: Data processing program flow. Up to the first guess reconstruction the data is processes using the IceRec framework. The analysis of DOM related observables and the event classification is done using Python with dedicated analysis libraries. See text for details.

Calibration

The raw data stream from the readout channels of the DOM have to be calibrated. As described in Section 4.1.3, the calibration comprises the conversion of ATWD and FADC count readings to voltages and the bin numbers to times. Based on the PMT gain calibration it also allows to translate measured charges to a charge count measured in photo-electrons (pe). The calibration information from the most recent DOMCAL run is present in the data stream and provides necessary figures for PMT gain, ATWD and FADC gain, count and time conversion. The calibration is performed using the DOMCALIBRATOR module.

Feature Extraction

Generally, analysis and reconstruction modules compute observables based on time and charge information. The FEATURE-EXTRACTOR provides algorithms to extract this information from the ATWD and FADC waveforms. Two distinct result entities are available after the feature extraction, namely hits and pulses. The first represents a single photo-electron emitted at the PMT cathode, with a charge of 1 pe and a time corresponding to the time at the PMT cathode. The latter reflects a bunch of photo-electrons which form one pulse in the waveform due to the overlap of separate single pulses from photo-electrons that have been emitted at the PMT cathode. The time of the pulse is defined by its leading edge and is also converted to the corresponding time at the cathode. The pulse charge is computed from the area under the waveform.

The FEATURE-EXTRACTOR is a quite sophisticated piece of code and has many knobs and handles to tune the estimation of the baseline, the conversion of pulse to photo-electron emission time at the PMT cathode, the finding of pulses in the waveform and even corrections for electronic artifacts. Details can be found in the documentation [45]. For this work a commonly used configuration with an unfolding method is used, a baseline estimate is done using the first three bins of the ATWD and the PMT transit time correction is enabled. The following modules use the reconstructed pulses of the waveform.

Calculation of Event Characteristics

Based on the pulse information common event observables are computed, e.g. number of hit modules, number of hit strings, number of pulses seen by each OM, etc. Detailed information about the observables used for the filtering and classification are given in the following section.

First Guess Reconstruction

Two first guess event reconstruction algorithms (LINE-FIT and TENSOR OF INERTIA) are performed. Details to the algorithms can be found in Section 5.1. The resulting parameters are used in the filtering process.

The results are written to analysis files and further analyzed using data analysis modules for Python [133].

7.2 Filtering

The background MC samples described in Section 6.1.1 are used to simulate the atmospheric muon background. The used $\nu_e + \bar{\nu}_e$ signal data set has been described in Section 6.3.2 and constitutes a hypothetical E^{-2} signal spectrum. The Poly-Gonato event set, which includes low energy events, is used to develop filter cuts which remove events with primary energies lower than 10 TeV. This selection justifies the use of the high-energy 2-Component background and neutrino event samples with an energy range starting at 10 TeV, which are then used to derive an event classification to remove the background from atmospheric muons.

7.2.1 Filtering on Global Event Observables

As mentioned above, the first filter level is used to eliminate low energetic background. It is based on global event observables which are particularly correlated with the energy deposit. A first measure of the energy deposit in the detector are the number of hit modules which contribute to the event. It is called the N-channel observable (N_{chan}). An even better correlation with the energy deposit provides the number of pulses in the event and the total charge recorded by all contributing modules, denoted with N_{pulse} and Σ_{charge}, respectively. The N_{chan} to energy relation saturates quickly and counting individual pulses or charges in OMs provides more information than just counting hit modules.

In order to derive the cut values, only events with primary particle energies below 10 TeV are taken into account. Just from statistical considerations, the N-channel cut is set to $N_{chan} > \langle N_{chan} \rangle + 5 \cdot \sigma_{N_{chan}} \approx 70$. The N_{pulse} distribution is more exposed to fluctuations in the energy deposit, therefore the maximum of the distribution of simulated values in the background sample is used adding an uncertainty of 100%, resulting in the cut $N_{pulse} > 400$. The cut on the total charge is simply set to the same value ($\Sigma_{charge} > 400\,\text{pe}$), since these measures are strongly correlated with a correlation coefficient of ~ 0.9 and the total charge showed some unexpected fluctuations, which could be attributed to wrong baseline estimates in the feature extraction.

Applying these cuts to the Poly-Gonato event set removes the muon background from primaries with energies below 10 TeV. Of course it also removes a large fraction from the high-energy two-component data sample since the cuts were defined with large margins and there is also a contribution from not fully contained air showers, with a much lower energy deposit. The same applies for the signal in the energy region below 1 PeV, also due to not fully contained events and the conservative cut estimation.

Before summary plots are shown and the passing rates for this level are given, another selection criterion is introduced that has also been applied at this analysis step. It focuses more on the event signature than simple energy deposit considerations. The observable is defined as the fraction of modules that contribute to the event with only one recorded pulse ($N^1_{\text{chan}}/N_{\text{chan}}$). One can assume that most of the OMs with only one pulse will be on the surface of the illuminated volume that surrounds the energy deposit volume. Muons in background events will deposit their energy along a track, whereas cascades deposit their energy in an almost spherical volume around the interaction vertex. Since the surface to volume ratio of a cylinder is larger than that of a sphere, the fraction of OMs with only one pulse is larger for track-like events. The distribution of $N^1_{\text{chan}}/N_{\text{chan}}$ is shown in Figure 7.2 and shows a good separation potential for signal and background events. The right plot of the same figure shows the efficiencies for signal and background events with increasing cut strength. A cut of $N^1_{\text{chan}}/N_{\text{chan}} < 0.45$ was chosen in order to keep $\sim$80% of the signal, while the background is reduced by more than a factor of five.

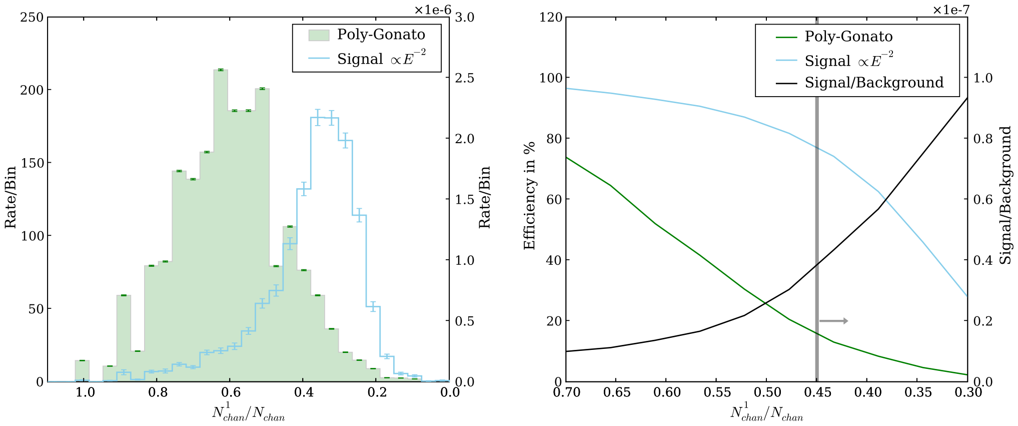

Figure 7.2: LEFT: Fraction of the number of channels with only one pulse distribution for the Poly-Gonato background MC sample (green, left ordinate) and an E^{-2} signal sample (blue, right ordinate). Note the different scales on the ordinates, the background is dominating over the full range. RIGHT: Passing rates for the two event samples with increasing cut strength of $N^1_{\text{chan}}/N_{\text{chan}}$. The cut is set to $N^1_{\text{chan}}/N_{\text{chan}} < 0.45$, as indicated by the vertical line. The arrow points towards the region passing the cut. In black and on a different scale (right ordinate) the signal-to-background ratio is plotted.

Figure 7.3 shows the distribution of the event observables used in the filtering described in this Section, and in addition the primary energy spectrum to illustrate the effect of the filtering. The dashed lines correspond to the full event samples, the solid lines to the event samples after applying the combination of all cuts. The cut value is marked with a vertical grey line and an arrow pointing towards the region which is kept after the filtering. Despite the fact that the background (Poly-Gonato event sample) is reduced to $\sim 0.1\%$ which makes the following high level data processing possible, it was the aim to remove the low energetic background to justify the use of the high energetic background and signal event sets. Indeed, the distributions of the Poly-Gonato and 2-Component background samples agree within the errors already before the filtering except in the regions where the low energy events dominate. The same minor differences remain after filtering. However, the primary energy spectrum shows a significant discrepancy between the two background MC samples. The 2-Component sample has no contributions below 200 TeV, which can be explained by too low statistics. The bin content of the histogram shown here is of the order of 1000 events, while the reduction is of the same order in the energy region below 1 PeV, which leaves no passing events. For the following filtering the impact can be treated as an overall uncertainty due to low statistics, because the missing events would be distributed over the variables used in the next filter level.

Also shown are the distributions for the signal sample. Even after the application of the cuts the signal is dominated by background in all observables except at the higher ends which corresponds to extremely high energetic events. The signal-to-background ratio over the full energy range is $\mathcal{O}(10^{-6})$, being still as low as 10^{-2} at 1 EeV, which is estimated using the 2-Component sample. The numbers have to be taken with care, since they are only valid for the assumed signal flux of $1 \cdot 10^{-8} E^{-2}\,\mathrm{GeV\,s^{-1}\,sr^{-1}\,cm^{-2}}$.

Table 7.1 summarizes the cuts on the global event variables described above. Passing rates for each individual cut are given, for all data sets split into two energy regions: low energy (<1 PeV), high energy (>1 PeV); and for the full energy region. The passing rates for the combination off all four cuts are given in the "Total" column. The filtering performance is similar for both background samples. The high energy part of the 2-Component sample seems to be reduced more than the corresponding Poly-Gonato sample, however, taking into account that the latter sample does not include a large fraction of the highest energies, the efficiency is biased. The overall reduction of the background by a factor of $\sim 10^3$ in contrast to an efficiency of 40% for the signal sample is remarkable. However, as mentioned this is by far not enough, the background needs to be reduced depending on the energy range by 10^2 to 10^6. This can be achieved with a sophisticated classification scheme, which is presented in Section 7.3.

7.2.2 Filtering on OM related Observables

After the global observables are used to remove the low energy background events and to reduce the number of events to a manageable amount, OM related observables are computed for the remaining part of the data sets.

For every event the distributions of the following quantities recorded in each

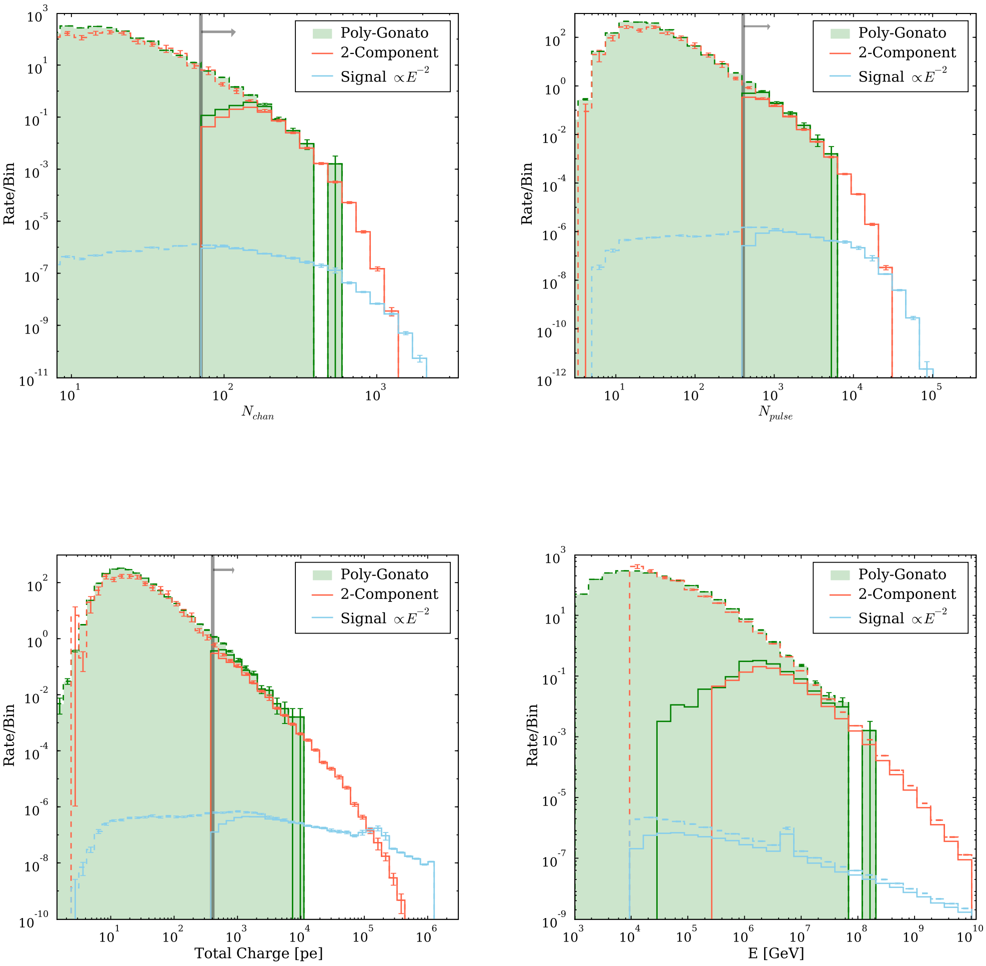

Figure 7.3: The plots show from top left to bottom right the distributions of the observables N_{chan}, N_{pulse}, Σ_{charge} and the spectrum of the primary particle energies. For all samples the distributions at trigger level are shown (dashed) and after the application of the cuts described in the text (solid). The different event samples are the background data samples: Poly-Gonato (green) and 2-Component (red); and a signal (blue) sample weighted to a flux of $1 \cdot 10^{-7} E^{-2}\,\text{GeV}\,\text{s}^{-1}\,\text{sr}^{-1}\,\text{cm}^{-2}$. The vertical lines indicate the cut applied for the filtering, the arrows point towards the region which is kept.

Table 7.1: Filtering efficiencies for the individual cut variables ($N_{\text{chan}} > 70$, $N_{\text{pulse}} > 400$, $\Sigma_{\text{charge}} > 400\,\text{pe}$, $N^1_{\text{chan}}/N_{\text{chan}} < 0.45$) and the combination of all (Total). All numbers are given as percentage of the event rate at trigger level.

Sample	N_{chan}	N_{pulse}	Σ_{charge}	$N^1_{\text{chan}}/N_{\text{chan}}$	Total
Poly-Gonato (P-G)	0.65%	0.12%	0.12%	15.76%	0.07%
P-G ($E < 1\,\text{PeV}$)	0.48%	0.04%	0.05%	15.72%	0.02%
P-G ($E > 1\,\text{PeV}$)	35.63%	16.88	14.26%	47.74%	11.79%
2-Component (2-C)	0.86%	0.11%	0.09%	18.52%	0.07%
2-C ($E < 1\,\text{PeV}$)	0.68%	0.03%	0.02%	18.36%	0.01%
2-C ($E > 1\,\text{PeV}$)	30.02%	13.02%	11.25%	44.51%	9.26%
Signal (S)	44.26%	54.94%	55.07%	77.20%	40.63%
S ($E < 1\,\text{PeV}$)	39.08%	52.20%	52.60%	76.63%	35.79%
S ($E > 1\,\text{PeV}$)	69.69%	68.36%	67.19%	80.03%	64.35%

optical module, which contributes to the event with at least 5 pulses, are analyzed:

- total charge $\Sigma^{\text{OM}}_{\text{charge}}$,
- number of pulses $N^{\text{OM}}_{\text{pulse}}$,
- length of the signal ΔT^{OM},
- time between the first pulse and the pulse when half of the charge has been recorded ($T^{\text{OM}}_{1/2}$).

The distribution of each variable for every event is analyzed by computing the quantities: maximum; mean; median; variance; root mean square (rms), defined as $x_{\text{rms}} = \sqrt{\langle x^2 \rangle} = \sqrt{\langle x \rangle^2 + \sigma^2}$; and the standardized central moments, namely skew and kurtosis, defined as $\mu_k = 1/\sigma^k \int_{-\infty}^{\infty} (x-\mu)^k f(x) dx$, where μ denotes the mean of the distribution and $k = 3, 4$ for skew and kurtosis, respectively [39].

Figure 7.4 shows those observables which appear to have a high potential to discriminate background and signal events. Graph (a) shows the distribution of rms values of the $N^{\text{OM}}_{\text{pulse}}$ distributions from every event. For background events the rms is mostly lower than for signal events. This is expected, because the energy deposit for background events is distributed in a larger volume, compared to signal events with the same energy deposit, and thus the contributing OMs register less charge, which translates into fewer pulses. In addition the $N^{\text{OM}}_{\text{pulse}}$ distribution is wide for signal events, because modules close to the vertex see much light and those further away will have only a few pulses. This is reflected in a larger variance of the $N^{\text{OM}}_{\text{pulse}}$ distributions which contributes to the larger rms values for signal events. Background events on average show a lower spread in the number of pulses, as the energy loss is distributed along the muon track. Graph (b) depicts the skewness of the $N^{\text{OM}}_{\text{pulse}}$ distributions, which also shows a distinct behavior for signal and background events. It tends to negative and values close to zero for signal events, meaning that the distribution of $N_{\mathrm{pulse}}^{\mathrm{OM}}$ is in many events left-skewed or symmetric, whereas it is right-skewed (positive skewness) for background events. In other words, the peak of the signal $N_{\mathrm{pulse}}^{\mathrm{OM}}$ distribution has a larger value than the mean, whereas the peak of the background distribution is located left to the mean. Again, this is explainable by the fact that modules with few pulses dominate the background event.

Graph (c) shows the distribution of the means of the $T_{1/2}^{\mathrm{OM}}$ values. For background events it is dominated by small values. This can be explained by the fact, that, if an OM is triggered by the light from a passing muon, the muon probably passed not too far away, because on average it produces less light. In turn this means the light traveled only a short distance, hence it is less scattered. The recorded waveform is located at the beginning of the readout time window, which gives small $T_{1/2}^{\mathrm{OM}}$ values. In contrast to background events, OMs contributing to a signal event are mostly not close to the vertex, hence the light has to propagate larger distances, which results in more scattering and a wider waveform. Thus the $T_{1/2}^{\mathrm{OM}}$ distributions are dominated by larger times. Finally graph (d) visualizes that also the distribution of the skewness of $T_{1/2}^{\mathrm{OM}}$ distributions shows a significant difference between signal and background events. Left skewed events dominate the signal sample, whereas there are more right skewed events in background events. Again, this describes the position of the peak and the tails of the $T_{1/2}^{\mathrm{OM}}$ distributions. Signal events have a peak above the mean and a tail to lower $T_{1/2}^{\mathrm{OM}}$ values and vice versa for background events. This can be explained by the same argumentation as above. The contribution from modules nearby the track are dominant for background events, whereas the contribution from modules distant from the vertex dominate for signal events. For the latter, most modules are multiple scattering lengths away from the vertex and will have large arrival times. Only a few are close to the vertex which constitute the tail to the left in the distribution.

Although the distributions of these observables show a good potential to discriminate signal and background they are overlapping and it would be inefficient to just apply cuts on each variable individually. Hence, a classification algorithm is used to determine the event class from the observables described here. This is discussed in Section 7.3, after two additional event variables are introduced that will also be used for the final event filtering.

7.2.3 Observables from First Guess Reconstruction

In the standard cascade analysis the velocity parameter of the LINE-FIT reconstruction and the eigenvalue ratio of the TENSOR OF INERTIA reconstruction are used as a first event filter and the online cascade filter running at Pole is based on these two reconstruction parameters. They show a good discriminating potential for cascade analysis and therefore are taken into account here as well. Both quantities have been introduced and discussed in Section 5.1.

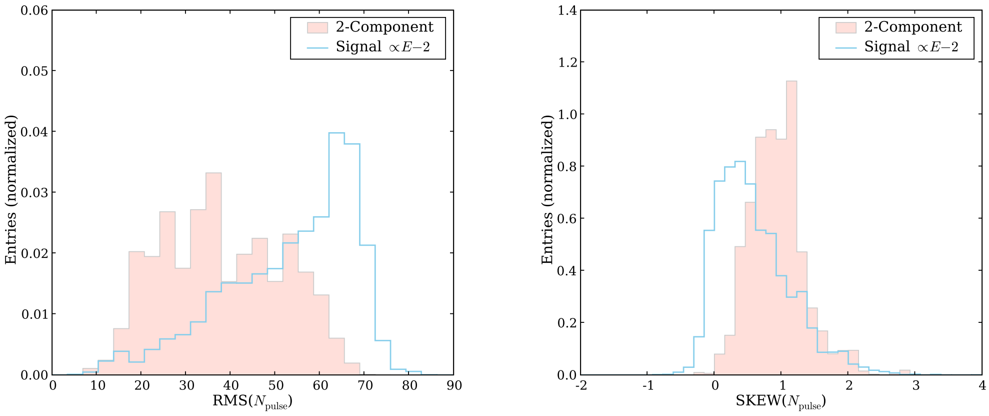

(a) Distribution of rms values of $N_{\text{pulse}}^{\text{OM}}$

(b) Distribution of skewness values of $N_{\text{pulse}}^{\text{OM}}$

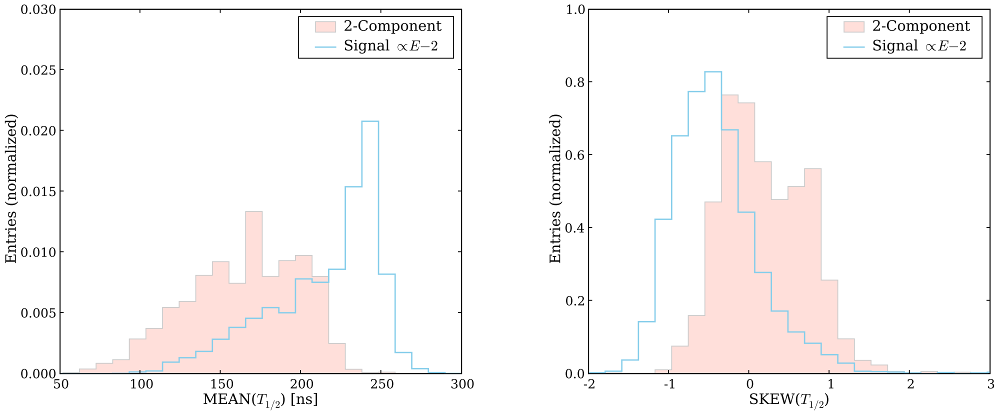

(c) Distribution of mean values of $T_{1/2}^{\text{OM}}$

(d) Distribution of skewness values of $T_{1/2}^{\text{OM}}$

Figure 7.4: The plots show OM related observables which appear to have distinct distributions for background (filled red) and signal (blue) events. See text for details.

Figure 7.5 shows the Line-Fit velocity for reconstructed background and signal events. For track-like background events the velocity is close to 0.3 m/ns due to the movement of the muon. For cascade-like signal events, which are rather static in space, the Line-Fit velocity evaluates to small values.

The Tensor of Inertia reconstruction provides a good measure of the sphericity of the distribution of triggered modules in space. The eigenvalue ratio is 1/3 for a spherical distribution and smaller for more stretched distributions. Since muon background events deposit energy along a track and signal events are more spherical, they show distinct distributions in this parameter, as depicted in the right plot of Figure 7.5.

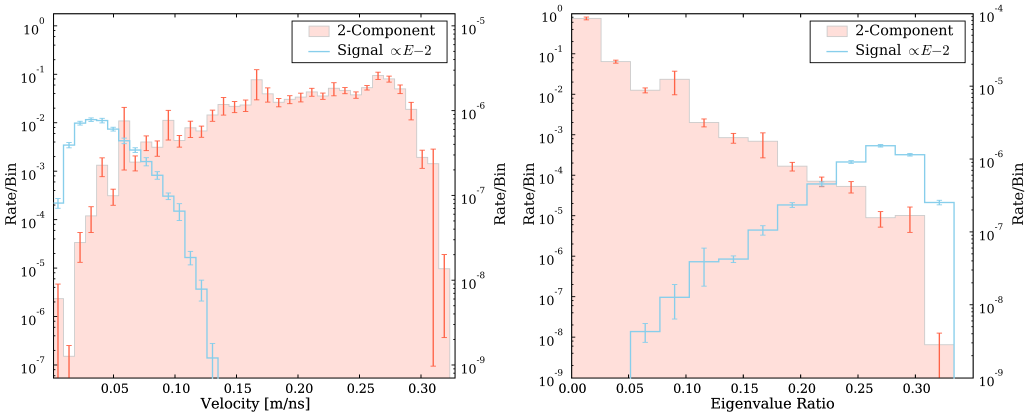

Figure 7.5: For signal (blue) and background (filled red) events the distribution of reconstruction parameters from first guess reconstructions are shown. The Line-Fit velocity (left) is larger for background than for signal events. The distribution of eigenvalue ratios obtained from the Tensor of Inertia reconstruction (right) are peaked at 0.3. Note the different scales for signal (left ordinate) and background events (right ordinate). The background distribution dominates over the full parameter space.

The Line-Fit velocity and Tensor of Inertia eigenvalue ratio parameters are not used to filter events in each of these two dimensions individually, rather they are used in combination with the OM related observables to construct an event classification.

7.3 Event Classification

The observables described in the previous sections suggest a good discrimination between signal and background. However, applying cuts on each observable individually is not suitable, since the distributions are partly overlapping. Either the selected signal events would be contaminated by background events if the cut is too loose, or the efficiency would be too low, when the cut is too harsh.

A solution to this problem is to use a classification scheme which is based on all observables. In a mathematical description the problem is to find a function $f(\vec{x})$ which yields the probability that the observables $\vec{x}$ are member of a class [39, 142]:

$$P(\text{class}|\vec{x}) = f_{\text{class}}(\vec{x}; \theta_{\text{class}}), \tag{7.1}$$

where θ_{class} are the parameters of the function. Given two functions which describe each class, signal (S) and background (B), one can construct the likelihood ratio:

$$\frac{P(S|\vec{x})}{P(B|\vec{x})} = \frac{f_S(\vec{x}; \theta_S)}{f_B(\vec{x}; \theta_B)}, \tag{7.2}$$

which is larger than 1 if $\vec{x}$ belongs to the signal class and smaller if it does not. To avoid numerical instabilities, when dividing extremely different numbers $\mathcal{O}(10^{15})$, the logarithm of equation (7.2) is used:

$$\mathcal{L} = \log\left(\frac{f_S(\vec{x}; \theta_S)}{f_B(\vec{x}; \theta_B)}\right) = \log(f_S(\vec{x}; \theta_S)) - \log(f_B(\vec{x}; \theta_B)). \tag{7.3}$$

With this transformation signal events are mapped to positive values and background events to negative values. There are different approaches to the problem of the estimation of $P(\text{class}|\vec{x})$. For example Bayesian classification uses Monte Carlo data to find $P(\vec{x}|\text{class})$ and the class probability is computed using Bayes' rule [39, 140]. Here, the approach known as kernel probability density estimation is chosen. It is introduced in the following section and the application in this sensitivity study is demonstrated.

7.3.1 Kernel Probability Density Estimation

Using a density estimation method one can approximate the functions f_s and f_B from given signal and background Monte Carlo data samples. Kernel probability density estimation (kernel PDE) provides an unbinned and non-parametric[1] estimate of a probability density function (PDF) [123].

Given a data set of random variates $\{\vec{t}_i; i = 1..N\}$ in a k-dimensional space the general kernel estimate of the underlying PDF is given by the sum of kernels centered around each point

$$f(\vec{x}) = \frac{1}{Nh^k} \sum_{i=1}^{N} K\left(\frac{\vec{x} - \vec{t}_i}{h}\right), \tag{7.4}$$

---

[1] non-parametric means that no assumptions are made about the form of the PDF, e.g. the histogram is the prototypical non-parametric density estimate (it can be constructed using a square function as kernel)

where K is the kernel function and h the smoothing parameter, also called the bandwidth. The role of K is to spread out the contribution of each data point to the estimate. In case of a static-kernel PDE, which is used here, the h parameter is fixed. It is determined from the sample and set to $h = N^{-1/(k+4)}$ [94, 123] and could be optimized in order to maximize, e.g. the best signal-to-noise ratio [81], which is not done here.

A standard choice for the kernel function is a multivariate Gaussian distribution [94], with this equation (7.4) reads as:

$$f(\vec{x}) = \frac{1}{N(2\pi h)^{k/2}|V|^{1/2}} \sum_{i=1}^{N} w_i \cdot \exp\left(-\frac{\vec{d}_i^T V^{-1} \vec{d}_i}{2h^2}\right), \tag{7.5}$$

where $\vec{d}_i = \vec{x} - \vec{t}_i$, and V is the covariance matrix estimated from the data set ($|V|$ denotes its determinant) and w_i the weight of $\vec{t}_i$, if the random variates are attributed with weights. It is important to notice that, in case of weighted samples $\vec{t}_i$, the covariance matrix has to be calculated taking the weights into account [121].

With this technique the functions $f_S(\vec{x};\theta_S)$ and $f_B(\vec{x};\theta_B)$ can be estimated from a training sample of signal and background Monte Carlo events, respectively. The parameters $\theta_{S,B}$ correspond to the two parameters of the kernel estimate, the bandwidth and the covariance matrix. For this study 20% from each data sample have been used for the "training", which is the estimation of a PDF describing the signal and background probability of events, respectively. The 6-dimensional parameter space is spanned by the rms and skewness of the $N_{\mathrm{pulse}}^{\mathrm{OM}}$ distributions, the mean and skewness of the $T_{1/2}^{\mathrm{OM}}$ distributions, the LINE-FIT velocity and TENSOR OF INERTIA eigenvalue ratio parameter. Due to the "curse of dimensionality" one is restricted to use a limited amount of variables, because the volume of the parameter space increases exponentially with the number of dimensions and a training with limited amount of data does not evenly sample the full phase space. Fortunately, as argued in [124], it has a minor effect for the application in discrimination problems where two kernel density estimations are compared.

7.3.2 Application of Kernel-PDE

Figure 7.6 shows as an example three input observable distributions of the training samples in combination with the corresponding distribution of random samples drawn from the kernel PDE. The left and right plots show background and signal samples, respectively. The agreement between the estimated distributions and the "training" samples is satisfactory, the shape is sufficiently described, individual structures are not reflected by the estimation. However, these individual structures like the spikes in the "training" samples can be ascribed to large weights and the situation could be improved with larger statistics in the Monte Carlo data samples. Also the estimated samples are reaching into unphysical parameter spaces, e.g. negative LINE-FIT velocities, which is caused by the symmetric kernel function with a non-zero width, which introduces contributions outside the boundaries of a parameter. This does not have an impact, because in the classification the kernel PDE is evaluated only within the bounds defined by the data samples. The strongly fluctuating weights make it difficult to perform statistical tests to affirm the consistency between the estimated and true PDF at a certain confidence level. However, a Kolmogorov-Smirnov test [119] was performed in each dimension neglecting the weights. The test uses 100 random variates, drawn from the estimated multivariate Gaussian kernel PDE and compares the cumulative distribution of these to the same number of items drawn from the signal and background samples, respectively. In case of items drawn from the signal sample and compared to the kernel PDE of the signal distribution, the null-hypothesis that both samples are governed by the same underlying PDF cannot be rejected at a confidence level of 10%. However, the p-values of the Kolmogorov-Smirnov test between these samples and those drawn from the background kernel PDE yield p-values worse than $\mathcal{O}(10^{-7})$. This supports the assumption that the kernel PDE method provides a reasonable estimate of the functions f_S and f_B.

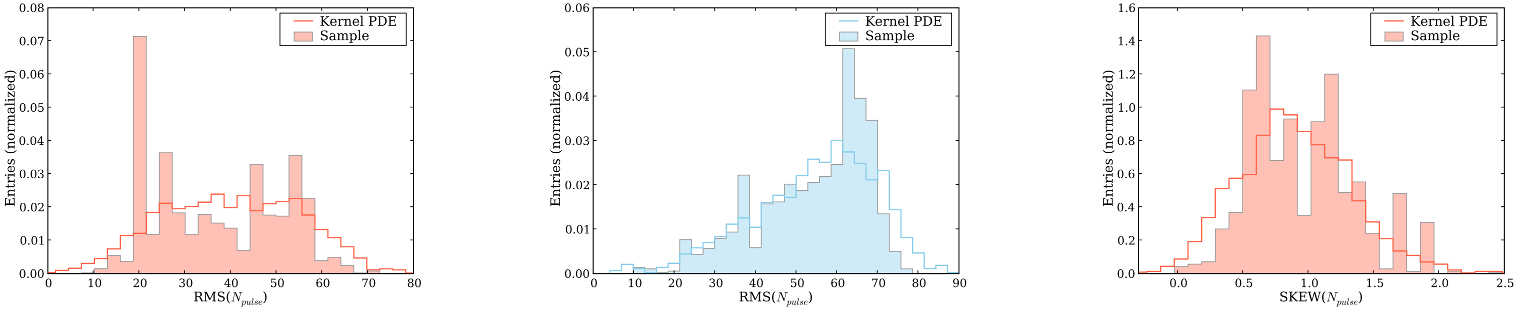

(a) Distribution of rms values of $N_{\text{pulse}}^{\text{OM}}$ for background events

(b) Distribution of rms values of $N_{\text{pulse}}^{\text{OM}}$ for signal events

(c) Distribution of skewness values of $N_{\text{pulse}}^{\text{OM}}$ for background events

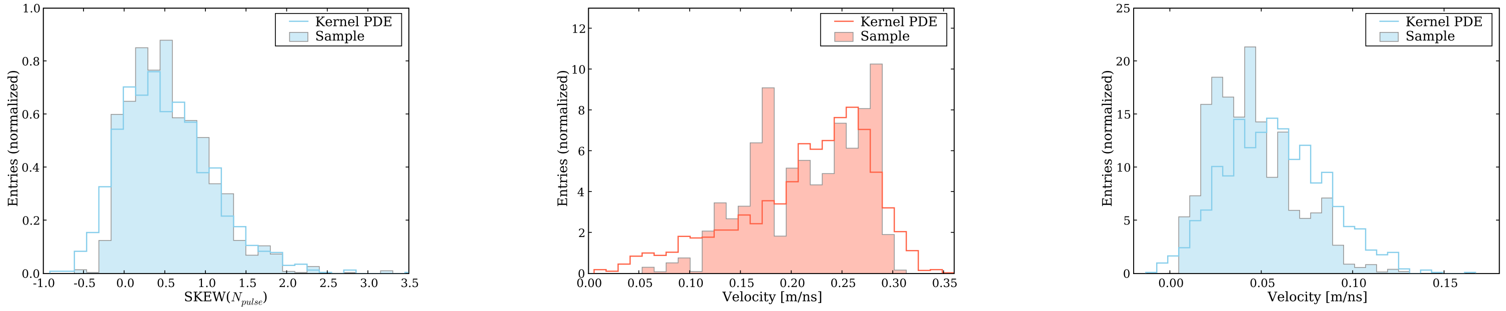

(d) Distribution of skewness values of $N_{\text{pulse}}^{\text{OM}}$ for signal events

(e) Distribution of LINE-FIT velocities for background events

(f) Distribution of LINE-FIT velocities for signal events

Figure 7.6: Distribution of training samples (filled) of the event observables used for the classification and random samples drawn from the kernel density estimate (line) that approximates the probability distributions in the 6-dimensional parameter space. Here only three of the six observables are shown as examples, the distributions in the other parameters show similar agreement. The left and right plots show background and signal samples, respectively.

7.3.3 Kernel-PDE and Classification Results

The likelihood ratio defined in equation (7.3) provides a very powerful discriminant and is evaluated using the estimated PDF functions for the remaining events. Figure 7.7 shows the logarithm of the ratio for signal and background, normalized to the minimal value of both distributions. Events with a negative $\mathcal{L} = \log_{10}(f_S/f_B)$ are more likely to be background. Most background events are classified correctly with the method described here. Only a small contribution extends into the signal regime with positive values. The signal samples are partly misidentified as background, however, the peak of the distribution is just above zero and a large fraction is clearly classified to be signal. The distribution extends to larger values in the signal region due to the normalization to the minimum value obtained, which compresses the background regime from -1 to 0.

There are discontinuities in the distribution of $\mathcal{L} > 0.1$ for background events, which is visible in the magnified inset plot. The problem arises due to too small statistics of the background sample, the peaks are build by single events with relatively large event weights. In the plot shown, this has been eliminated to some extend by applying an additional cut on the energy deposit, which exploits the different energy spectra of signal and background. Also previous analyses used the reconstructed energy in the final event selection to remove a large fraction of remaining background [98, 131]. Since no energy reconstruction was performed, the total charge parameter Σ_{charge} is used as an approximate measure of the energy deposit . The lower plot in Figure 7.7 shows the signal-to-background ratio in this two dimensional parameter space. In particular the background events with low energy deposits with Σ_{charge} below $\sim 1{\cdot}10^3$ cause discontinuities because of large event weights. To remove these events, a cut of $\Sigma_{\text{charge}} > 1 \cdot 10^3$ is applied. Although the plot suggests a two dimensional cut in the energy deposit and likelihood ratio parameter space, this path is not followed. Clearly the contribution of background events decreases to high energy deposits, however, the limited statistics do not motivate a optimization of the final event selection. Time limitations dictated the use of the available samples.

For increasing $\mathcal{L}$-cut values the signal and background efficiencies $N_{\mathcal{L}>\mathcal{L}_{\text{cut}}}/N$ are plotted in Figure 7.8 (left plot). The background rejection is very good, a reduction of $\sim 10^5$ is reached, while still more than 60% of the signal remains. Beyond that the interpretation becomes difficult due to the fluctuations of the surviving background. It is not clear, whether the gradient is still exponential or flattens out. At the point where the background vanishes, the signal efficiency is still above 20%.

Also shown in the right plot of the same Figure are the event rates within one year and the signal-to-background ratio as a function of the cut value of $\mathcal{L}$. Applying a cut at 0.05 slightly above the transition point at 0, where events are classified to be signal, the signal-to-noise ratio is ~ 0.1. Again, the behavior beyond that point is difficult to assess, the background contribution has discontinuities when the remaining events are removed one after the other. At a cut of $\mathcal{L} > 0.28$ the last background event is removed and the signal-to-noise ratio becomes infinite.

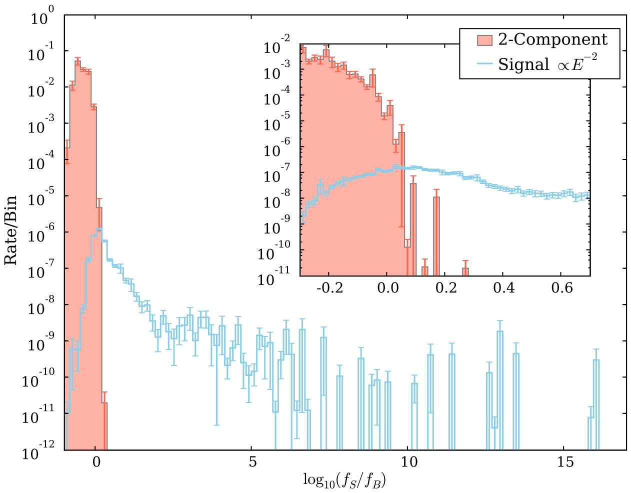

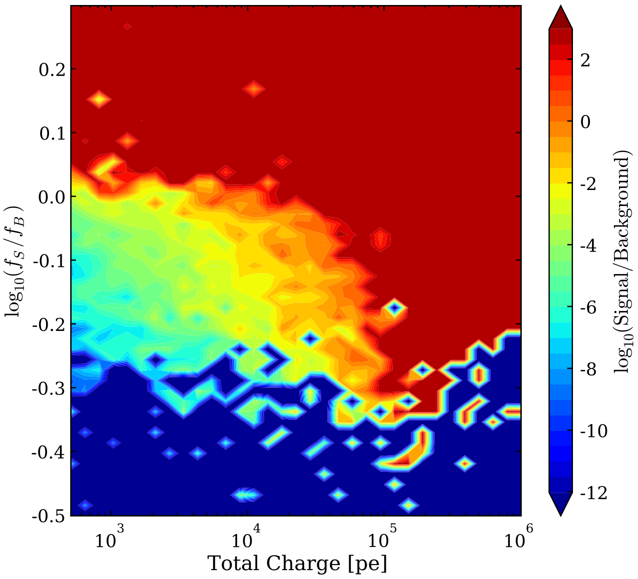

Figure 7.7: Top: The likelihood ratio distribution for signal and background samples. The ratio is defined by $\log_{10}(f_S/f_B)$ with probability density functions obtained from kernel PDE of signal and background training samples. The inset plot shows a magnified version with finer binning at the cross-over region around 0, where events become classified as being signal rather than background. Bottom: Signal-to-background ratio as a function of total charge and $\mathcal{L}$. Note the spots in the upper right to center area, these are the events causing discontinuities due to high event weights.

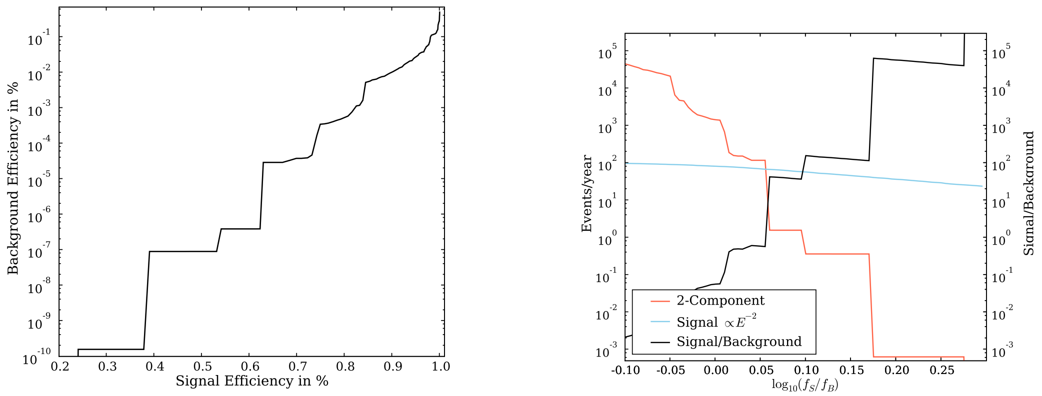

Figure 7.8: Left: Background and signal efficiencies with increasing $\mathcal{L}$-cut. The signal efficiency falls on a linear scale, while the background drops exponentially. Too few statistics of the background sample lead to discontinuities when the last remaining event samples are removed which have large event weights. Right: The event rate expected in one year calculated from background and signal event samples as a function of the cut value of $\mathcal{L}$. The signal-to-background ratio is plotted on a different scale. Again, fluctuations in the background sample introduce large background rate variations.

A cut of $\mathcal{L} > 0.36$ is chosen in order to be unaffected by statistical fluctuation. The value is more than three standard deviations above the maximum $\mathcal{L}$ value of the background distribution. The standard deviation is estimated using only values with $\mathcal{L} > 0$. An extrapolation of the likelihood ratio distribution for background events yields a background expectation of $4.1 \cdot 10^{-4}$ events per year, which can be treated in the sensitivity calculation as an expectation of 0 background events. The final passing rates are summarized in Table 7.2. The following Chapter gives the results obtained from this analysis, namely the electron-neutrino effective area of the detector and the sensitivity to electron neutrino fluxes.

Table 7.2: Event rate and filter efficiency for the E^{-2} signal flux and background sample after application of the final cut $\mathcal{L} > 0.36$. The efficiency is calculated with respect to the level one selection. The expected background rate for $\mathcal{L} > 0.36$ is extrapolated from the likelihood ratio plot (Figure 7.7). The background sample yields an event count of 0.

	Signal			Background
	Full	E ≤ 1 PeV	E > 1 PeV	
Events/year	18.8	12.5	6.3	$4.1 \cdot 10^{-4}$
Efficiency	15.3%	15.1%	15.8%	$< 10^{-11}$%

Chapter 8

Results

This chapter summarizes the results obtained from the analysis described in the previous Chapter and discusses the sensitivity of the IceCube detector for ultra-high energy electron-neutrino events.

8.1 Effective Detector Area

A useful measure of the detector performance is the neutrino effective area. It represents the area of an ideal detector which is capable of detecting neutrino events with 100% efficiency. If the neutrino effective area is known, it is easy to compute the number of events N expected to be observed from a certain flux $\phi(E, \theta)$ in a given time T:

$$N = T \int A_{\mathrm{eff}}(E, \theta)\, \phi(E, \theta)\, dE d\Omega\,. \tag{8.1}$$

The energy and angle dependent effective area $A_{eff}(E, \theta)$ is estimated using simulated data. It is given by the ratio of observed to generated events multiplied by the area over which the simulated events have been distributed:

$$A_{\mathrm{eff}}(E, \theta) = \frac{N_{\mathrm{observed}}(E, \theta)}{N_{\mathrm{gen}}(E, \theta)} \cdot A_{\mathrm{gen}}, \tag{8.2}$$

where N_{observed} and N_{gen} are the unweighted event counts[1]. The energy and zenith angle dependence is introduced by calculating the effective area for different energy and angle bins. The resulting effective area is only an estimate which resembles the true effective area in the limit of an infinite number of generated events and an infinite simulation area.

---

[1] The neutrino-generator forces neutrinos to interact in the detection volume, hence the observed events need to be weighted with the interaction probability weight to get the correct event count ratio (see Section 6.2).

Figure 8.1 shows the effective area as a function of primary neutrino energy. The corresponding event count is obtained from the final data selection which was based on an E^{-2} flux spectrum. The effective area itself is not directly depending on the power index of the simulated spectrum. However, the final event count depends on filter settings which can be optimized for different spectra, hence this would introduce an indirect dependency on the spectral index. The filtering applied in this analysis is rather independent of the spectral shape and the effect on the effective area is marginal. The zenith angle dependence is illustrated by plotting the effective area for different zenith angle regions. The absorption in the earth due to the higher cross section clearly extinguishes the contribution from events coming from below the horizon. The remaining events at the highest energies coming from below the horizon have performed multiple neutrino nucleon interactions, where the first interaction outside the detector volume is a neutral current interaction with a neutrino of the same flavor in the final state which subsequently reaches the detector. The effective area grows from $\sim 10^{-2}\,\mathrm{m}^2$ at $10\,\mathrm{TeV}$ to $\sim 200\,\mathrm{m}^2$ at $10\,\mathrm{EeV}$ due to the increasing signal efficiency and the rise of the neutrino nucleon cross section. In particular the rise above $1\,\mathrm{PeV}$ grows similar to the cross section as $\sim E^{0.36}$ (see Section 3.1). The integrated effective area over the energy range $10\,\mathrm{TeV}$ to $10\,\mathrm{EeV}$ is $\sim 45\,\mathrm{m}^2$. The impact of resonant $\bar{\nu}_e e^-$ scattering is prominent in the energy range 6-7 PeV and causes a peak in the effective area with $120\,\mathrm{m}^2$, which is the average over a bin width of 1.6 PeV. In comparison to previous cascade analyses with the AMANDA-II detector [98, 131], the electron-neutrino effective area of ICECUBE is larger by a factor of 20 for energies up to $\sim 5\,\mathrm{PeV}$. This is compatible with the increase of the detector volume, because these events need to be confined in or close to the fiducial volume of the detector. At higher energies, however, the increase of the effective area is only a factor of 2, due to the fact that events outside of the fiducial volume contribute more and more and the increase of the detector area is becoming less important. For a detailed quantification one needs to take detector saturation effects and non linear signal responses into account, which is particularly important at energies above $\sim 100\,\mathrm{PeV}$. The high energy analysis including all neutrino flavors benefits from the long muon range which grows as $\log(E_\mu)$ and the regeneration of taus. The effective area presented in [65] for the AMANDA-II all flavor analysis exceeds the one reached here by one order of magnitude at energies above $\sim 10\,\mathrm{PeV}$. The consequences will be be further discussed at the end of this Chapter.

8.2 Effective Detector Volume

The effective detector volume is a more seizable measure for the detector performance than the effective area as it does not account for the neutrino interaction probability inside the detector volume. It simply relates the number of observed events N_{observed} that reached the detector volume to the number of generated events N_{gen}. Scaling the volume used for the simulation V_{gen}, yields the effective

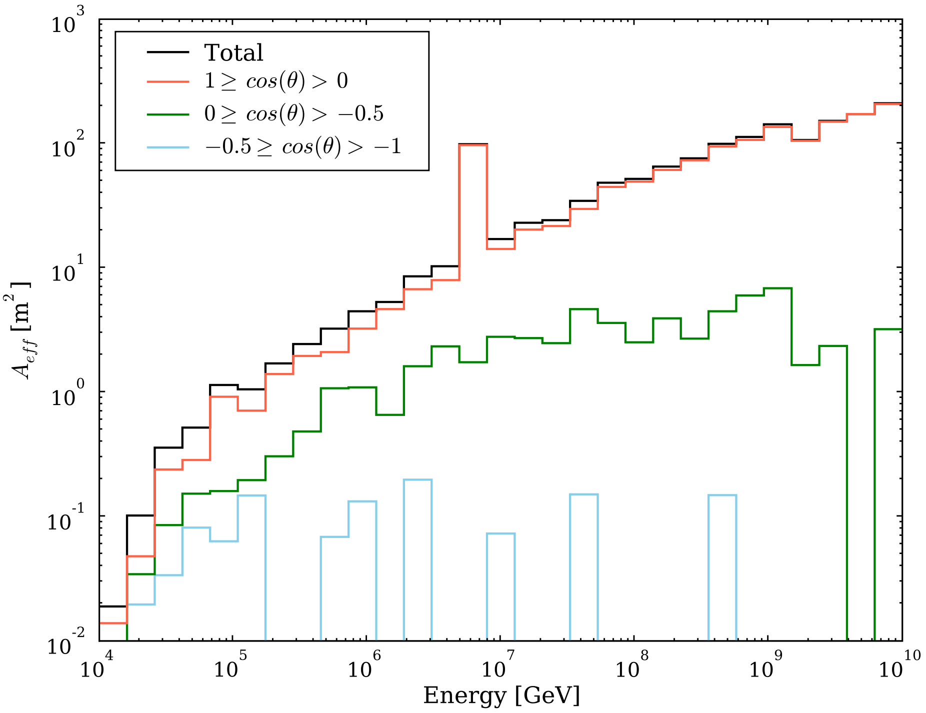

Figure 8.1: Electron-neutrino effective area of the ICECUBE detector as a function of the neutrino energy. To illustrate that the earth becomes opaque for neutrinos at high energies, different zenith angle bands are shown separately.

volume for electron neutrino detection:

$$V_{\text{eff}}(E,\theta) = \frac{N_{\text{observed}}(E,\theta)}{N_{\text{gen}}(E,\theta)} \cdot V_{\text{gen}} \,. \tag{8.3}$$

The event counts used are the bare numbers of generated events no event weights need to be included. The generation volume is chosen larger than the geometrical detector volume to include all neutrino tracks in the simulation which could possibly be detected.

Figure 8.2 shows the effective volume for electron neutrinos. At low energies the effective volume is limited due to the filtering which is optimized for energies above 1 PeV. Indeed, the effective volume rises constantly up to 1 EeV, reaching almost 85% of the fiducial detector volume of 1 km^3, when it starts to degrade due to absorption effects in the earth which is not compensated anymore by more efficient selection. The absorption effect is illustrated by showing the effective volume for different zenith bands. Neutrinos coming from the lower hemisphere are more likely to be absorbed with raising energy. Interestingly the effect of the Glashow-Resonance is visible in the energy bin below 10 PeV, even the neutrino flux from the upper hemisphere is reduced and in combination with the lower flux from the lower hemisphere, the total effective area shows a significant dip in the same energy bin. The performance of the event filtering at low energies is clearly not optimal, it barely reaches 10% of the geometrical detector volume and decreases slowly reaching a value of more than 50% only at ∼ 200 TeV.

8.3 Sensitivities and Model Rejection Factor

The sensitivity can be interpreted as the minimum flux of neutrinos that is required to produce a specified output, given a certain signal-to-noise ratio. The output defined here is an average upper limit, thus the sensitivity yields a measure for the maximal input signal which could be excluded. It does not give the detection capability of a neutrino signal. The signal-to-noise ratio is related to the inverse of the model rejection factor (MRF), which is introduced in the following Section together with a precise definition of the sensitivity.

8.3.1 Model Rejection Factor

The result of a counting experiment like IceCube is a number of observed events n. Given an expected number of background events b it is possible to infer an interval $[\mu_l, \mu_u]$ around the mean number of signal events μ which is compatible with this observation at a certain confidence level (CL). In [54] a frequentist approach for the construction of confidence intervals is described, which automatically yields an upper limit μ_u, if the observation does not allow to compute a central confidence interval around μ. This approach is used here at a confidence level of 90% and the corresponding upper limit is denoted with $\mu_{90\%}$.

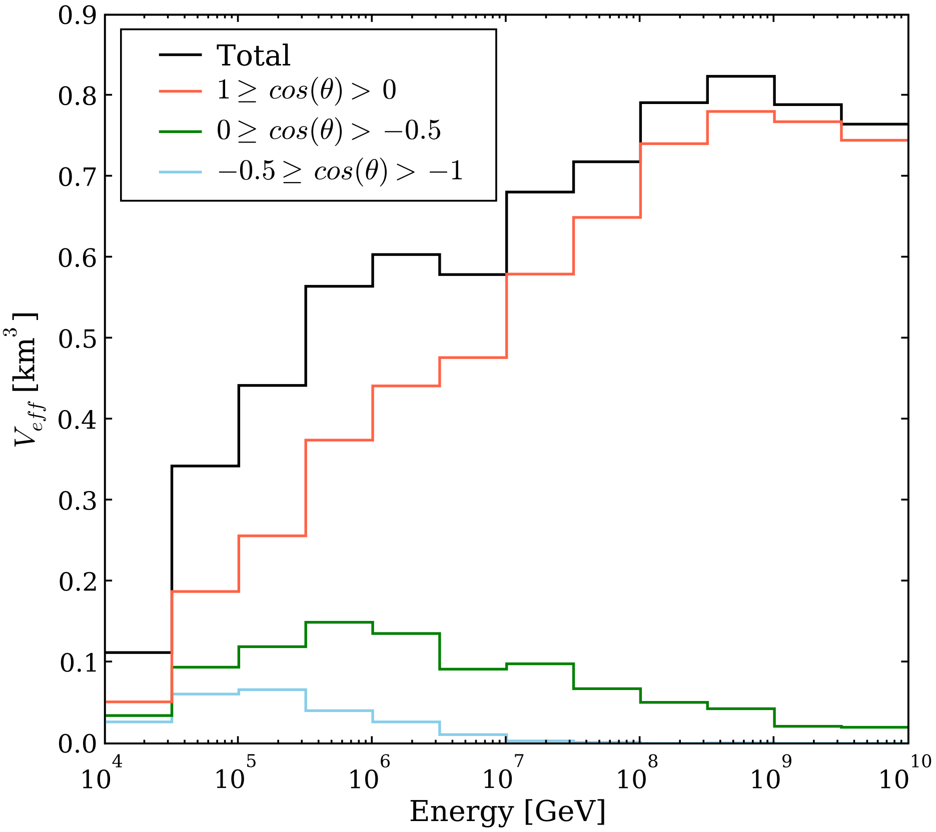

Figure 8.2: Electron neutrino effective volume of the IceCube detector as a function of the neutrino energy. To illustrate that the absorption effect by the earth different zenith angle bands are shown separately. The IceCube detector has a geometrical volume of $\sim 1\,\mathrm{km}^3$.

In case of a sensitivity study, where the number of observed events is not known, and when optimizing for the best event selection, the average upper limit provides an independent measure for all possible experimental outcomes [9]. It is constructed by averaging the upper limits obtained from all experimental outcomes n assuming an expected background event count b and no signal events:

$$\langle \mu_{90\%} \rangle = \sum_{n=0}^{\infty} \mu_{90\%}(n, b) P(n|b)\,. \tag{8.4}$$

The averaging is performed taking into account the underlying Poisson distribution of the experimental counting outcomes n. The values used here are taken from Table XII in [54].

The model rejection factor (MRF) is defined as the average upper limit divided by the expected amount of signal counts N_m from a hypothetical model flux $\phi_m(E)$ [78]. It is the fraction of an observed signal which could possibly be a background contribution and therefore closely related to a signal-to-noise ratio. Rescaling the flux ϕ_m with the MRF obtained from the corresponding signal rate N_m yields the flux strength which could be excluded at 90% confidence level. In other words, it describes the sensitivity for a certain flux:

$$\phi_{90\%}^{sens}(E) = \frac{\langle \mu_{90\%} \rangle}{N_m} \cdot \phi_m(E) = \mathrm{MRF}(\phi_m) \cdot \phi_m(E)\,. \tag{8.5}$$

8.3.2 Sensitivity

The energy distribution of events for different model fluxes determines the boundaries of the valid energy range of the sensitivity. The sensitivity interval is commonly taken as the central region of the observed spectrum which produces 90% of the observed signal events. In addition the model rejection factor depends on the model flux and thus a certain flux sensitivity is strictly valid only for the same flux shape. In particular, if a cut optimization is performed, the resulting cuts are only optimal for the simulated flux. However, here only an E^{-2} spectrum was used to determine the final cuts and the same filtering criteria have been applied to different model fluxes.

The impact of the different spectral indices on the observed particle spectrum and the sensitivity intervals is shown in Figure 8.3. For a soft spectrum proportional to E^{-3} the main contribution to the signal events stem from electron neutrinos with energies $\mathcal{O}(10\,\mathrm{TeV})$, whereas for a hard E^{-1} spectrum the peak of the distribution is shifted towards higher energies $\mathcal{O}(10\,\mathrm{EeV})$ (left plot). The intervals containing 90% of the signal are summarized in Table 8.1.

The right plot of the same figure shows the sensitivities calculated for the various power indices γ. Using the same flux normalization, harder fluxes with increasing γ indices produce more signal, hence the sensitivity increases. However, it does not increase linearly. To emphasize this effect and to show the performance for expected model fluxes of $\phi_m \propto E^{-2}$, the sensitivities are plotted in the lower

Table 8.1: Central primary spectrum energy intervals containing 90% of the neutrino events observed at the final filtering level for different power indices.

Spectrum	E_{min} [GeV]	E_{max} [GeV]
E^{-1}	$1.3 \cdot 10^7$	$6.2 \cdot 10^9$
E^{-2}	$1.6 \cdot 10^4$	$1.3 \cdot 10^7$
E^{-3}	$1 \cdot 10^4$	$1.7 \cdot 10^5$

graph weighted with E^2. The figure clearly illustrates the influence of the model spectrum. For soft spectra the sensitivity is valid for energies in the TeV-region, with increasing power indices the sensitive region of the detector shifts towards higher energies. However, due to the falling flux which cannot be compensated by the raising cross section nor by the increase of the sensitive volume, the detector performance compared to low energies decreases in terms of sensitivity. Varying the power index of the spectrum is similar to the quasi-differential sensitivity calculation presented below, where one calculates a sensitivity for distinct energy intervals, because the different spectra emphasize the detector performance in different energy intervals. The upper boundary of all sensitivities can be interpreted as a differential sensitivity valid in the energy range from 10 TeV to 5 EeV which is independent of the model spectrum. The plot suggest that the best sensitivity on any astrophysical neutrino flux is in the energy range from 100 TeV to 1 PeV. The commonly quoted sensitivity to an E^{-2} electron neutrino signal spectrum in the energy range 16 TeV to 13 PeV is:

$$\phi_{\text{sens}} = 1.5 \cdot 10^{-8} E^{-2}\,\text{GeV}\,\text{s}^{-1}\,\text{sr}^{-1}\,\text{cm}^{-2}\,.$$

The E^{-2} spectrum is chosen because most models which try to explain the mechanisms of particle acceleration and high energy neutrino production at cosmic sources rely on the first order Fermi-acceleration which suggest constant power indices of the source spectrum around $\gamma = -2$ over a few orders of magnitude in energy.

8.3.3 Event Rates for Specific Model Fluxes

In order to test the model rejection capabilities and to give an impression how many observed events can be expected within one year lifetime of the IceCube detector, several model fluxes have been used to re-weight the signal event spectrum and to calculate the corresponding signal passing rates. The results are summarized in Table 8.2. Model rejection factors smaller than one indicate that the flux model could be ruled out at 90% C.L.. Prompt atmospheric neutrino fluxes are at the border to being constrained. With a dedicated low energy analysis the situation should improve. The two AGN models MPR-Jet [107] and SSDS-core [126, 127] should either be detected or ruled out. Even if MPR-jet model is downscaled by one order of magnitude and the SSDS-core model by two orders of magnitude, they

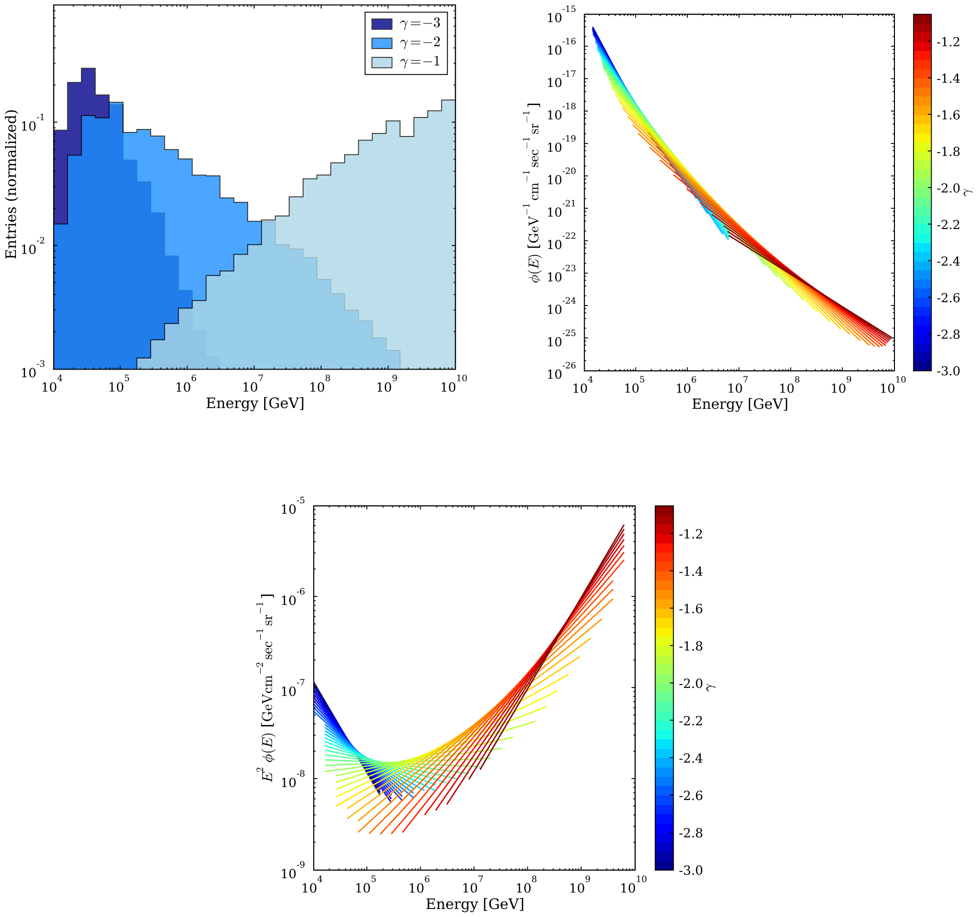

Figure 8.3: Left: The primary energy spectrum of electron neutrinos in the final event sample weighted for different source spectra. The sensitivity is calculated for the central interval containing 90% of the spectrum. Right: Sensitivities obtained for various power indices γ of the signal spectrum $\propto E^{\gamma}$. Bottom: The same plot weighted with E^2 to emphasize the impact changing model spectra. Soft spectra result in sensitivity boundaries in the 10 TeV to 1 PeV region, whereas sensitivities for harder fluxes constrain in the energy region 10 PeV to 10 EeV, though with lower performance.

could be ruled out. The GRB and GZK fluxes are out of reach to be measured. The reason for this will become clear when discussing the quasi-differential flux sensitivity introduced in the next Section.

Table 8.2: Expected event rates and model rejection factors for different model fluxes within one year lifetime of the ICECUBE detector. The flux models are grouped into atmospheric, AGN, GRB and GZK fluxes. Model rejection factors smaller than one indicate that this flux could be ruled out at 90% C.L.. See also Figure 8.4.

Model	$\langle N_S \rangle$	MRF
Honda (conventional) [82]	0.4	5.8
Naumov (prompt) [57]	2.5	1.0
Costa (prompt) [48]	1.1	2.2
MPR-Jet [107]	21.1	0.1
SSDS-Core [126, 127]	216.4	$1.1{\cdot}10^{-2}$
Waxman-Bahcall GRB [135]	0.4	5.5
GZK (1) [147]	$2.0{\cdot}10^{-3}$	$1.2{\cdot}10^{3}$
GZK (2) [147]	$3.1{\cdot}10^{-2}$	78.7
GZK (3) [52, 53]	$2.2{\cdot}10^{-2}$	112.2

8.3.4 Differential Sensitivity

The sensitivity discussed in the previous section is only valid for an E^{-2} spectrum. Models with different flux shapes can only be ruled out safely, when either tested directly by calculating event rates, or when the predicted flux is larger over the full sensitivity range. This is due to the the fact that the sensitivity is calculated by integrating over the quoted energy range. It has been shown that different assumed signal spectra drastically change the achieved sensitivities because the neutrino detection capability changes with energy. It is therefore desired to present experimental limits and sensitivities independent of the spectral shape. The method used here follows [98]. The expected number of signal events is calculated only for an energy range short enough not to be dependent on the spectral index of the source signal. The energy range chosen here is one decade. The mean event count is calculated in form of a moving average at distinct energies E_0:

$$N(E_o) = 4\pi \cdot T \cdot \int_{E_{\min}}^{E_{\max}} \phi_m \cdot A_{\mathrm{eff},\Delta E}(E) dE \,, \tag{8.6}$$

where $A_{\mathrm{eff},\Delta E}(E)$ is the effective area given in the energy bin ΔE which includes the energy E, $E_{\min}$ and $E_{\max}$ are the boundaries of the integration window set to one decade in energy. The events from the $\bar{\nu}_e e^-$ scattering interactions at the Glashow resonance are not take into account in the averaging since they bias the sensitivity too strongly in the energy range 1 PeV to 50 PeV. The limit obtained in this way is called a quasi-differential limit and independent of the assumed model flux. It is shown in Figure 8.4 as cross marks, the errors bars indicate the change in the sensitivity for signal spectra ϕ_m with spectral indices varying from -1 to -3. Also shown are model fluxes for AGN and GZK neutrinos, as well as theoretical bounds and limits for E^{-2} fluxes from other experiments.

The sensitivity for an ν_e flux proportional to E^{-2} reaches the Waxman-Bahcall bound and cuts into the AGN models shown in the plot. It is also well below the limits obtained with existing experiments. However, compared to experiments like RICE, AUGER and ANITA-LITE, the sensitivity covers only an energy region up to 10 PeV and does not reach into the GZK region. The quasi-differential limit illustrates the performance decrease at high energies. Clearly the sensitive volume of ICECUBE in the ν_e-channel is still not large enough to be sensitive to the low GZK flux rates.

In the lower energy range the sensitivity reaches into the atmospheric neutrino flux. Although the expected event rates are low in this analysis, it should be possible to measure the electron neutrino flux and determine the contribution from prompt neutrinos with a dedicated low energy analysis.

Compared to a previous 5 year cascade analysis with the AMANDA-II detector the sensitivity of the full ICECUBE detector is already within one year of operation a factor of ~ 9 better in the energy region around 1 PeV. However, the sensitivity of the muon channel within one year ICECUBE operation, is another factor of ~ 4 better and ranges to higher energies [21]. Taking into account that this analysis has no optimal cut at the last filter level and does not include muon- and tau-neutrino events, which contribute to the cascade detection channel, it is expected that the same performance as of muon analyses can be achieved in the energy range up to ~ 10 PeV. It seems that the long muon range can not compensate the good background separation capabilities of the electron channel at these energies. For an E^{-2} spectrum the main signal contribution lies in the 10 TeV to 10 PeV region, hence both detection channels are competitive in a diffuse analysis that is optimized for this energy. This is supported by the findings in [96] where a comparison of the different diffuse flux detection-channels was performed, and the fact that previous all-flavor analysis yielded comparable event rates for all three neutrino flavors [10, 125].

The advantage of the full waveform information has been demonstrated recently in [125]. Using the AMANDA-II Transient Waveform Recording (TWR) DAQ, the preliminary limit obtained in an all flavor diffuse flux analysis optimized for energies above 1 PeV is already after one year better than a comparable analysis using four years of the regular AMANDA-II data without the waveform information. In that work it is argued that the performance increase is due to the fact that events passing the detector in a distance of several 100 m can still be classified as signal or background. Indeed, a similar statement can be made here, Figure 8.5 shows the event distribution in the x-y plane of signal events passing the final filter. The distribution ranges ~ 300 m outside of the instrumented volume.

To sum up, the sensitivity obtained in this work for electron-neutrinos based

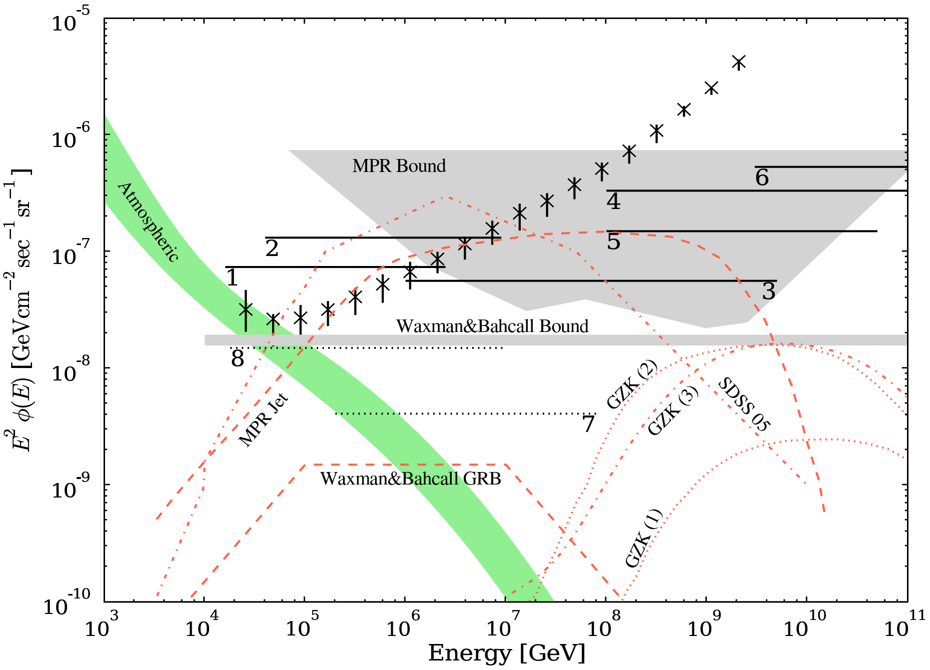

Figure 8.4: The quasi-differential sensitivity obtained from an average sensitivity calculation at distinct energies. Theoretical bounds are depicted, namely the Waxman-Bahcall bound [134] and the MPR bound [107], where the upper bound of the area is a flux constraint for optically thick sources and the lower bound for optically thin sources. Two AGN model fluxes are shown, the MPR jet model [107] and a recently updated model for neutrino fluxes from AGN cores [126, 127]. Three different GZK flux predictions are shown, one model with different evolution scenarios (1,2) [147] and a flux calculated by Engel, Stanev and Seckel [52, 53]. The GRB flux predicted by Waxman-Bahcall [135] is also included in the plot. Atmospheric neutrinos flux predictions are indicated as a band, the upper bound is the horizontal neutrino flux according to Honda [82] including a prompt neutrino contribution following Naumov [57]. The lower bound is the vertical contribution including prompt neutrinos according to [48]. Flux limits from different experiments are given, scaled to a single flavor limit: (1) AMANDA-II 4-year ν_μ [3], (2) AMANDA-II 5-year cascade search [13], (3) AMANDA-II 1-year enhanced data acquisition system [125], (4) RICE [101]; (5) AUGER ν_τ [38], (6) ANITA-LITE [33], (7) ICECUBE 1-year ν_μ [21], and (8) ICECUBE 1-year ν_e obtained in this work. The cross marks are the quasi-differential limit obtained by averaging the sensitivity in distinct energy bins, the errors bars indicate the change in the sensitivity for signal spectra ϕ_m with spectral indices varying from -1 to -3.

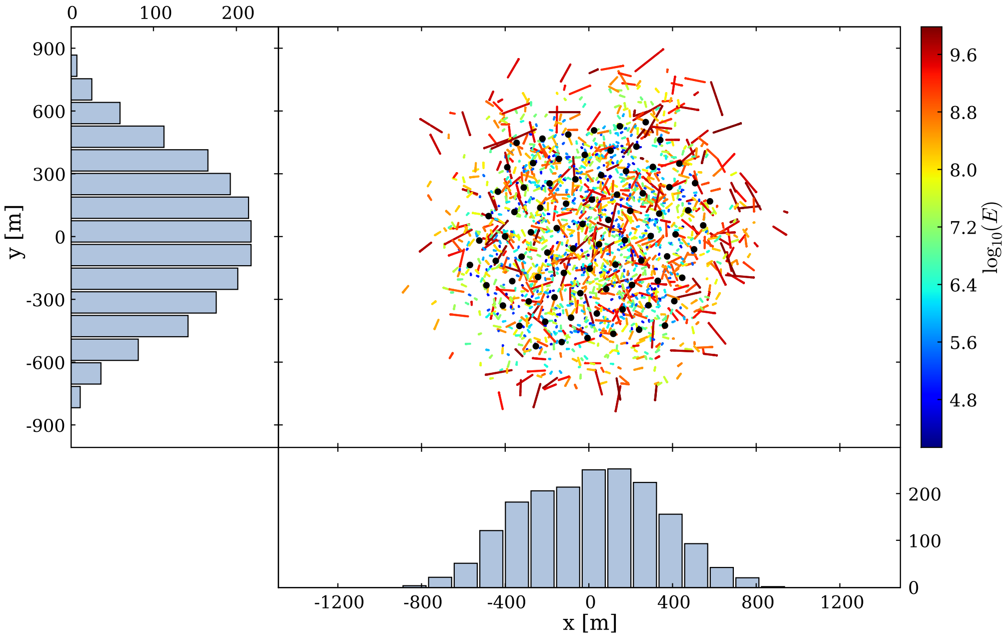

Figure 8.5: Event distribution in the x-y plane of the IceCube detector. Cascade vertices obtained from the cascade propagation software are indicated with colored dots. The dot size corresponds to the energy loss at that point. The color coding reflects the primary neutrino energy. The black points indicate the string locations of the IceCube detector. Projections of the x-y coordinates are shown at the bottom and left of the graph. The events are not weighted.

on the cascade detection channel improves previous limits from AMANDA-II by a factor of ~ 9 in the energy range from 10 TeV to 10 PeV. Including muon and tau neutrinos with cascade-like signature should improve the sensitivity at least to the expected level of muon neutrino analyses. Compared to existing high energy analyses including muon and tau neutrinos, the sensitivity is not improved. Due to the long muon range, the sensitivity obtained with AMANDA-II is even better at energies above ~ 10 PeV. The improvements expected in the high energy range, when including muons in this analysis, are probably not as good as in the lower energy range, since the sensitive area of AMANDA-II in high energy analysis is already much larger than the instrumented volume of ICECUBE.

8.4 Statistical and Systematic Errors

The following Section discusses the impact of statistical and systematic errors on the final sensitivity result. Since this study is solely based on simulated event samples, systematical errors can be assessed by varying fundamental parameters of the simulation and study the impact on the final event rates. Detailed analysis have not been performed for this particular work, rather existing error assessments from similar analyses have been used. This is justified as the underlying simulations are using the same tools. In the following the dominant sources of uncertainties are described.

8.4.1 Statistical Uncertainties

The signal simulation does not suffer from limited statistics and the error of the final passing rates can be calculated following the description in Section 6.2.3. Using equation (6.7) and (6.8), the relative error can be written as [39]:

$$\sigma_N/N = 1/\sqrt{N'} \qquad \text{with} \qquad N' = \left(\sum_i w_i\right)^2 / \sum_i w_i^2 \,. \tag{8.7}$$

The statistical uncertainty of the passing signal event sample is then calculated to be 5%.

For the background simulation, with zero events observed, one would scale the statistical uncertainty based on the simulation event weights in nearby bins. However, the weights of the events have large variations approaching this region, making a determination of this factor difficult. Nevertheless, it is calculated to be $\sim 30\%$ using the weights of the events passing a likelihood-ratio cut of 0.

8.4.2 Uncertainties related to the Cosmic Ray Flux

The average energy of cosmic-ray primaries of the background events before the final filtering is ~ 4.4 PeV and the uncertainties of the flux normalization at these energies are as large as 100% [146]. However, the 2-Component model used here has an uncertainty of 30% in the normalization [67] which is twice the value estimated in [105], where the simulated background rates of the same model are compared to experimental event rates for the uncertainty assessment. A value of 30% relative uncertainty is used here.

The uncertainty of the cosmic ray composition is estimated following [10] by considering two cases: proton-dominated composition and iron-dominated composition. Technically this is done by flipping the 2-Component model contributions of proton and iron. The change in the event rates before the last filtering level is an increase of $\sim 30\,\%$, which is used as the uncertainty ascribed to cosmic ray composition.

8.4.3 Uncertainties of Neutrino Cross Sections

The underlying software used for the simulation of neutrino interactions is also used in the analyses presented in [10]. There the uncertainty has been estimated to be 10%. At energies above 1 EeV, where the underlying cross sections depend on model extrapolations, the uncertainty of the cross section is as large as 100 % [63]. However, the main signal contribution for an E^{-2} spectrum is below these energies and in terms of passing rates the effect is negligible.

8.4.4 Detector Sensitivity and Ice Properties

Again, the effect of the uncertainties of the optical module sensitivities and the modeling of the ice properties has been analyzed in previous works. The uncertainty of the optical module sensitivity is taken to be 15% from the AMANDA-II high energy analysis [10]. However, in [21] it is argued that the impact of this parameter for a larger array is smaller, in particular for higher energies. In addition the calibration of the ICECUBE DOMs is more accurate than for the optical modules in AMANDA-II.

The uncertainty introduced by the ice modeling in the simulation is estimated to be 20% [4], though one can expect that the situation improves when detailed analysis with in-situ light sources become available.

8.4.5 Overall Uncertainty

Table 8.3 summarizes the uncertainties for the signal and background Monte Carlo samples. Summing the errors in quadrature gives an overall uncertainty of 41% for the signal and 58% for the background samples. In order to estimate a possible background rate change at the final level, a statistical uncertainty of 1.29 events is assumed, which is the 1σ upper limit of a zero event observation [54]. The background event count within one year is then $0.0^{+2.0}_{-0.0}$ and the signal event count for a flux of $\phi = 1 \cdot 10^{-7} E^{-2}\,\mathrm{GeV\,s^{-1}\,sr^{-1}\,cm^{-2}}$ is 18.7 ± 7.7. In the extreme case, the sensitivity to an E^{-2} flux degrades by a factor of ~ 2 and improves by a factor of $\sim 1/3$. The achieved sensitivity in the energy range from 16 TeV to 13 PeV is then:

$$\phi_{\mathrm{sens}} = 1.5^{+100\%}_{-33\%} \cdot 10^{-8} E^{-2}\,\mathrm{GeV\,s^{-1}\,sr^{-1}\,cm^{-2}}\,.$$

Table 8.3: Systematic and statistical uncertainties as discussed in the text.

Source	Background	Signal
Statistics	±30 %	±5 %
Cosmic ray normalization	±30 %	—
Cosmic ray composition	±30 %	—
Neutrino cross section	—	±10 %
Detector sensitivity	±15 %	±15 %
Ice properties	±20 %	±20 %
Total	±58 %	±41 %

Chapter 9

Summary and Outlook

In the first part of this work it was investigated whether it is possible to facilitate a direction reconstruction for cascade-like events. This would increase the importance of the cascade detection channel with the possibility to perform point-source analyses.

In the course of this investigation the simulation of electromagnetic and hadronic cascades was improved. Instead of a point-like light emitter cascades are now treated more realistically by taking into account the longitudinal development. This is a major improvement for electromagnetic cascades with energies above 10 PeV as the LPM effect increases the shower length significantly. At these energies the energy loss profile cannot be parameterized due to strong fluctuations, hence a one-dimensional simulation of the shower development has been developed. It incorporates parameterizations of bremsstrahlung and pair production cross sections including the LPM suppression effect. The resulting electromagnetic shower profiles can have lengths of more than 100 m.

Based on the modified light yield of elongated cascades (see Figure 4.14) a direction reconstruction for cascade-like events was developed, which incorporates the elongation of cascades. For the vertex and energy reconstruction the performance of the algorithm is as good as existing algorithms. The aimed reconstruction of the cascade direction with better than 10 ° was not achieved within the available time. However, positive indications were seen and the methods introduced will be incorporated in the ICEREC software framework [110]. In particular the "Deep-Core" extension of ICECUBE could improve the direction reconstruction due to denser module spacing. The decision to build this extension came too late to be included in the studies of this work, however, a dedicated analysis should be performed in the near future.

Consequently, without a direction reconstruction available, a diffuse flux analysis was developed to study the sensitivity of the complete ICECUBE detector in the ν_e detection channel. The sensitivity was assessed introducing new cut variables that exploit the time structure of photons arriving at individual optical modules. The resulting sensitivity reached within one year of data taking for an E^{-2} flux covers the energy range from 16 TeV to 13 PeV with a value of:

$$\phi_{\mathrm{sens}} = 1.5^{+100\%}_{-33\%} \cdot 10^{-8} E^{-2}\,\mathrm{GeV\,s^{-1}\,sr^{-1}\,cm^{-2}}\,.$$

Sensitivity is defined as the average upper limit that could be set in absence of a signal at 90 % confidence level. Without the use of sophisticated likelihood reconstructions the achieved sensitivity is already approximately one order of magnitude better than a more evolved cascade analysis using five years of AMANDA-II data [13].

At higher energies $\mathcal{O}(100\,\mathrm{PeV})$ the sensitivity of the ICECUBE detector in the ν_e detection channel is limited by low expected fluxes of ultra-high-energetic neutrinos and the finite detector volume. The quasi-differential limit derived in this work shows this performance decrease. The cascade channel is mostly restricted to the instrumented volume and only events within a maximum distance of ∼ 300 m outside of the geometrical volume of the detector can contribute to the signal. The effective volume reaches ∼ 0.9 km^3. Existing AMANDA-II analyses reach almost half this effective volume, since events outside of the detector contribute. Therefore, the improvements in the high energy region are not as good as in the 10 TeV to 10 PeV energy range.

The comparison with results from other experiments like AUGER and ANITA-LITE is more difficult. Of course experiments with larger detection volumes are superior at the highest energies. However, for comparisons in the same energy region, the assessment is subtle due to different detection channels and background contributions. With respect to many models, ICECUBE would cover lower energies, whereas AUGER and ANITA-LITE would cover the higher energy part of the spectrum. They are therefore complementing each other.

For the detection of GZK neutrinos most likely much larger detectors are required. Current development efforts address the possibility of radio and acoustic detection of high energy neutrino events [41]. A simulation of a detector instrumenting an area of $10 \times 10\,\mathrm{km}^2$ with radio and acoustic sensors, presented in [36], yields ∼ 20 GZK neutrino events per year assuming the flux predicted by [52]. Following the analysis in this work ICECUBE would detect at most one event within ten years of the same flux.

Improvements of the Analysis

Despite the improvements already achieved in this work, there are several things that can be optimized before the analysis is applied to data. The limited background statistics have to be increased and compared to a fraction of data taken with the detector in order to justify the filtering and classification based on simulated events. It is probably not necessary to use a dedicated high-energy background sample since the sensitive energy range is within the range where the standard Poly-Gonato background simulation provided by the collaboration is valid, i.e. below ∼ 100 PeV. However, a small high-energy sample should be used to study background contributions from cosmic rays with energies above $\sim 100\,\mathrm{PeV}$. The signal simulation should be extended to include the ν_μ and ν_τ interactions as these can also be classified as cascade-like due to the hadronic cascade in the final state of the neutrino-nucleon interaction and the decay signature of the tau, as well as high energy losses along the muon track.

The analysis does not include any likelihood reconstructions which provide parameters to discriminate cascade-like from track-like events [98]. In particular the reconstructed energy can be used to filter efficiently signal and background events and should also be included in a search for cascade-like events. Finally, the filtering could be optimized by introducing more filter levels.

In conclusion, the analysis presented in this work introduces new methods to improve existing cascade searches by exploiting the capabilities of the waveform readout system. A robust classification scheme has been utilized which yields promising results. This work suggests to focus on energies in the range from $10\,\mathrm{TeV}$ to $10\,\mathrm{PeV}$ in searches for cascade-like events. With the inclusion of all neutrino-flavors and energy reconstructions, an improvement of a least one order of magnitude is expected, reaching the sensitivity of diffuse muon analysis.

Appendix A

Details on the Simulation of Electromagnetic Cascades

A.1 Simulation of the Cascade Development

Already in a previous analyses, the simulation of the energy deposit and the corresponding Cherenkov light emission was adapted to reflect the longitudinal development of cascades [98]. Because the software used at that time was not applicable in this work, a new cascade simulation software was developed. For energies below $\mathcal{O}(1\,\mathrm{PeV})$ it follows the existing algorithm, where a single cascade is represented by a sequence of sub-cascades (Figure 3.8 on Page 34). Each sub-cascade is displaced in space and time and attributed with an energy according to the energy loss profile of low energetic cascades given by equation (3.16). The shift in space Δx follows the direction of the parent particle and is set to a few X_0, typically three radiation length. The corresponding time shift is $\Delta t = \Delta x / c$. The time integrated total light flux Φ emitted at shower depth x is given by the sum of fluxes ϕ_i from each sub-cascades at depth x_i

$$\Phi(x,t) = \sum_{i=0}^{n} \phi_i(x_i,t)\, E(x_i)\, H(t-t_i)\,, \tag{A.1}$$

where n is the number of sub-cascades, $E(x_i)$ is the integrated energy loss between two sub-cascades spaced by Δx: $E(x_i) = \int_{x_i-\Delta x}^{x_i} \frac{dE(x)}{dx} dx'_i$ and $H(t-t_i)$ the Heaviside function shifted by $t_i = t_0 + i\Delta t$. The Heaviside function accounts for the fact that only those sub-cascades contribute which have already emerged, hence, not only the spacial distribution of light changes due to the longitudinal development, but also the time distribution is affected.

A.2 Simulation of the longitudinal Energy Deposit at extremely-high Energies

For the simulation of the energy deposit profile at extremely-high energies, differential cross sections for bremsstrahlung and pair creation processes, including the LPM suppression effects derived by Midgal are used. These are shown in Figure 3.7 and 3.6 for different energies. The lower plots show the radiation length and mean free path, respectively, which have been obtained by numerical integration of the cross sections at distinct energies. For the simulation a cubic spline function is used to interpolate between different energies.

Cross section formulas

The cross section formulas used for the simulation have been taken from [91], where they are given per nucleus with charge Z. For a compound material like water the number of nuclei per unit volume is calculated taking into account the average charge per nucleus $\langle Z/A \rangle$ which is ~ 0.56 for water:

$$N = \frac{N_A}{A \cdot \langle Z/A \rangle}\, \rho,$$

where N_A is Avogadro's number, A the atomic weight, and ρ the density of the material. In the cross section formulas the atomic charge appears with exponents. For compound materials the averaged charge, has to be used where components are weighted with the exponent.

Simulation program flow

The simulation is performed in one dimension, all particles are propagated and secondaries are created until they fall below a threshold energy of $\mathcal{O}(10\,\mathrm{TeV})$ where the energy deposit of the particle can be well described by the parametrization of the energy loss profile given by equation (3.16). The total energy loss is then calculated by summation of all individual energy loss profiles appropriately shifted in space. The program flow of the simulation is given as follows:

1. determine the interaction point given by an exponential distribution with a scale parameter given by the radiation length (mean free path);
2. create bremsstrahlung photon (electron-positron pair) and sample energy transfer from the differential cross section;
3.
    a) remaining particles which are below the energy threshold are deposited and the energy loss profile obtained from the parametrization is added to the total energy loss at the current depth;

    b) remaining particles above the threshold are propagated further, starting at 1.

A difficulty is the sampling of the energy transfer according to the differential cross section. Since the parameter space is large it is not feasible to use the inverted histogram representation of the cross section at different energies to draw random variates from it. Here, a Markov chain algorithm is used to generate random variates following the differential cross sections.

Metropolis-Hastings algorithm

The Metropolis-Hastings [114, 146] algorithm allows to sample from an arbitrary probability density function (PDF), requiring only that a function $P(x)$ proportional to the density can be calculated at x. A Markov chain is constructed in which each state x_{t+1} depends only on the previous state x_t. It uses a proposal density function $Q(x'|x_t)$, which depends on the current state x_t, to generate a new proposal sample x'. The transition from x_t to x' is accepted according to a likelihood given by the ratio

$$\mathcal{L} = \frac{P(x')\,Q(x_t|x')}{P(x_t)\,Q(x'|x_t)}\,. \tag{A.2}$$

With this ratio, one determines whether the new proposal x' is more likely ($\mathcal{L} \geq 1$) than the current state x_t, and if so, it is accepted as the new state x_{t+1}. If it is not, it is only accepted with the probability of $\mathcal{L}$.

The proposal state x' can be drawn from an arbitrary distribution $Q(x')$, however, if the proposal state is drawn from a distribution which is similar to the target PDF, less proposals are rejected and the algorithm is very efficient. Here, the beta distribution [119, 136, 141] is chosen for Q. Using appropriate shape parameters, the distribution matches the cross section functions quite well, n.b. it does not depend on the previous state[1]. The shape parameters have been obtained by fitting the beta function to the cross sections. The beta function is related to the beta distribution and has identical shape parameters. Although the agreement is not sufficient in terms of a χ^2 test, it is good enough to draw proposal states from it.
Results of the simulation are depicted in Figure 3.9 on 35.

---

[1] which is then called an independence chain Metropolis-Hastings algorithm

Appendix B

Simulation Configuration

Listings of configuration parameters of programs and modules used in the simulation. It is not meant to be a complete list of all configuration parameters, rather it is a list of those values which were crucial to tweak in order make the simulation possible. For details the reader is referred to the documentation of the program.

Table B.1: Adapted settings of simulation programs.

Parameter	Setting	Comment
	CORSIKA	
NKG, EGS	T F	
ECUTS	500 500 2000 2000	Energy cuts for hadrons, muons, electrons, γs
	UCR-ICETRAY	
RADIUS	700 m	
LENGTH	1400 m	
CUTFE	500 MeV	

Table B.2: Adapted settings of simulation programs.

Parameter	Setting	Comment
	NEUTRINO-GENERATOR	
RADIUS	1000 m	
LENGTH	1000 m + 600 m	
	MMC	
ROMB	3	interpolation points for integration
ECUT	50 MeV	E_{thresh} for secondaries
	CMC	
SPLITWIDTH	10	
E_{thresh} SIMULATION	1 PeV	
	HIT-CONSTRUCTOR	
BINNING	Enabled	
BINS	0-600 in 5 ns 600-6000 in 30 ns	

List of Figures

Bibliography

[1] J. Abraham et al. Correlation of the Highest-Energy Cosmic Rays with Nearby Extragalactic Objects. *Science*, 318:896–897, 2007.

[2] A. Achterberg et al. Multi-messenger studies with AMANDA/IceCube: Observations and strategies. *Astropart. Phys.*, 2005. astro-ph/0509396.

[3] A. Achterberg et al. Multi-year search for a diffuse flux of muon neutrinos with AMANDA-II. *Phys. Rev.*, D76:042008, 2007. doi: 10.1103/PhysRevD.76.042008.

[4] A. Achterberg et al. Detection of Atmospheric Muon Neutrinos with the IceCube 9-String Detector. *Phys. Rev.*, D76:027101, 2007.

[5] A. Achterberg et al. Signal Capture, Digitization, and Time-Stamping in the IceCube Data Acquisition Subsystem, 2007. In preparation.

[6] A. Achterberg et al. Performance of the initial year partial IceCube array and the sensitivity of the full IceCube detector on search for extremely-high energy neutrino, 2008. In preparation.

[7] A. Achterberg et al. First year performance of the IceCube neutrino telescope. *Astropart. Phys.*, 26:155–173, 2006.

[8] A. Achterberg et al. Calibration and characterization of the IceCube photomultiplier tube, 2008. In preparation.

[9] M. Ackermann. *Searches for signals from cosmic point-like sources of high energy neutrinos in 5 years of AMANDA-II data.* PhD thesis, Humboldt-Universität zu Berlin, 2007.

[10] M. Ackermann et al. Search for Ultra-High-Energyg Neutrinos with AMANDA-II. *The Astrophysical Journal*, 675(2):1014–1024, 2008. doi: 10.1086/527046. URL `http://www.journals.uchicago.edu/doi/abs/10.1086/527046`.

[11] M. Ackermann et al. The ICECUBE prototype string in AMANDA. *Nucl. Instrum. Meth.*, A556:169–181, 2006.

[12] M. Ackermann et al. Optical properties of deep glacial ice at the south pole. *J. Geophys. Res.*, 111:D13203, 2006.

[13] O. Actis. *Search for neutrino-induced cascades with 5 year of the AMANDA-II data.* PhD thesis, Humboldt-Universität zu Berlin, 2008.

[14] F. Aharonian et al. A new population of very high energy gamma-ray sources in the Milky Way. *Science*, 307:1938–1942, 2005. doi: 10.1126/science.1108643.

[15] F. Aharonian et al. A detailed spectral and morphological study of the gamma- ray supernova remnant RX J1713.7-3946 with HESS. *Astron. Astrophys.*, 449:223–242, 2006. doi: 10.1051/0004-6361:20054279.

[16] F. Aharonian et al. Search for pulsed VHE gamma-ray emission from young pulsars with HESS. *Astropart. Phys.*, 2007. astro-ph/0702336.

[17] F. Aharonian et al. Serendipitous discovery of the unidentified extended TeV gamma-ray source HESS J1303-631. *Astron. Astrophys.*, 439:1013–1021, 2005.

[18] J. Ahrens et al. Observation of high energy atmospheric neutrinos with the Antarctic Muon and Neutrino Detector Array. *Phys. Rev.*, D66:012005, 2002. doi: 10.1103/PhysRevD.66.012005.

[19] J. Ahrens et al. Muon track reconstruction and data selection techniques in AMANDA. *Nucl. Instrum. Meth.*, A524:169–194, 2004.

[20] J. Ahrens et al. IceCube Preliminary Design Document, 2001. URL `http://www.icecube.wisc.edu/science/publications/pdd/`.

[21] J. Ahrens et al. Sensitivity of the IceCube detector to astrophysical sources of high energy muon neutrinos. *Astropart. Phys.*, 20:507–532, 2004. doi: 10.1016/j.astropartphys.2003.09.003.

[22] S. Aid et al. A Measurement and QCD Analysis of the Proton Structure Function $F_2(x, Q\ 2)$ at HERA. *Nucl. Phys.*, B470:3–40, 1996.

[23] J. Albert et al. VHE γ-Ray Observation of the Crab Nebula and its Pulsar with the MAGIC Telescope. *Astropart. Phys.*, 2007. arXiv:0705.3244.

[24] J. Albert et al. Observation of gamma rays from the galactic center with the MAGIC telescope. *Astrophys. J.*, 638:L101–L104, 2006.

[25] J. Alvarez-Muniz and E. Zas. The LPM effect for EeV hadronic showers in ice: Implications for radio detection of neutrinos. *Phys. Lett.*, B434:396–406, 1998.

[26] E. Andres et al. Observation of high-energy neutrinos using Cherenkov detectors embedded deep in Antarctic ice. *Nature*, 410:441–443, 2001.

[27] W. D. Arnett, J. Bahcall, R. P. Kirshner, and S. E. Woosley. SUPERNOVA SN1987A. *Ann. Rev. Astron. Astrophys.*, 27:629–700, 1989. doi: 10.1146/annurev.aa.27.090189.003213.

[28] P. Askebjer et al. Optical properties of deep ice at the south pole: absorption. *Appl. Opt.*, 36(18):4168–4180, 1997. URL `http://ao.osa.org/abstract.cfm?URI=ao-36-18-4168`.

[29] H. Athar, M. Jezabek, and O. Yasuda. Effects of neutrino mixing on high-energy cosmic neutrino flux. *Phys. Rev.*, D62:103007, 2000.

[30] V. Aynutdinov et al. Search for a diffuse flux of high-energy extraterrestrial neutrinos with the NT200 neutrino telescope. *Astropart. Phys.*, 25:140–150, 2006. doi: 10.1016/j.astropartphys.2005.12.005.

[31] V. Balkanov et al. An upper limit on the diffuse flux of high energy neutrinos obtained with the Baikal detector NT-96. *Astropart. Phys.*, 14:61–66, 2000. doi: 10.1016/S0927-6505(00)00110-9.

[32] G. D. Barr, T. K. Gaisser, P. Lipari, S. Robbins, and T. Stanev. A three-dimensional calculation of atmospheric neutrinos. *Phys. Rev.*, D70:023006, 2004. doi: 10.1103/PhysRevD.70.023006.

[33] S. W. Barwick et al. Constraints on cosmic neutrino fluxes from the antarctic impulsive transient antenna experiment. *Physical Review Letters*, 96(17):171101, 2006. doi: 10.1103/PhysRevLett.96.171101. URL `http://link.aps.org/abstract/PRL/v96/e171101`.

[34] J. K. Becker. High-energy neutrinos in the context of multimessenger physics. *Astropart. Phys.*, 2007. arXiv:0710.1557.

[35] W. Bednarek, G. F. Burgio, and T. Montaruli. Galactic discrete sources of high energy neutrinos. *New Astron. Rev.*, 49:1, 2005.

[36] D. Besson, S. Böser, R. Nahnhauer, P. B. Price, and J. A. Vandenbroucke. Simulation of a hybrid optical / radio / acoustic extension to IceCube for EHE neutrino detection. *Int. J. Mod. Phys.*, A21S1:259–264, 2006.

[37] S. Bevan et al. Simulation of Ultra High Energy Neutrino Interactions in Ice and Water. *Astropart. Phys.*, 28:366–379, 2007.

[38] O. B. Bigas et al. Limits to the diffuse flux of UHE tau neutrinos at EeV energies from the Pierre Auger Observatory. *Astropart. Phys.*, 2007. arXiv:0706.1658.

[39] G. Bohm and G. Zech. *Einführung in die Statistik und Messwertanalyse für Physiker*. DESY, Hamburg, 2006.

[40] J. Bolmont, B. Voigt, and R. Nahnhauer. Very high energy electromagnetic cascades in the LPM regime with IceCube. In *Proc. 30th ICRC*, 2007. Prepared for 30th International Cosmic Ray Conference (ICRC 2007), Merida, Yucatan, Mexico, 3-11 Jul 2007.

[41] Böser, S. *Acoustic detection of ultra-high energy cascades in ice*. PhD thesis, Humboldt-Universität zu Berlin, 2007.

[42] J. Breitweg et al. ZEUS results on the measurement and phenomenology of F2 at low x and low Q**2. *Eur. Phys. J.*, C7:609–630, 1999.

[43] G. Burdman, F. Halzen, and R. Gandhi. The highest energy cosmic rays and new particle physics. *Phys. Lett.*, B417:107–113, 1998.

[44] D. Chirkin. Cosmic ray energy spectrum measurement with the Antarctic Muon and Neutrino Detector Array (AMANDA), 2003. UMI-31-21434.

[45] D. Chirkin. *Feature Extraction of IceCube Waveforms*. Lawrence Berkeley National Laboratory, 2007.

[46] D. Chirkin and W. Rhode. Muon Monte Carlo: A high-precision tool for muon propagation through matter, 2004. hep-ph/0407075.

[47] B. M. Connolly, S. Y. BenZvi, C. B. Finley, A. C. O'Neill, and S. Westerhoff. Comparison of the ultra-high energy cosmic ray flux observed by AGASA, HiRes and Auger. *Phys. Rev.*, D74:043001, 2006. doi: 10.1103/PhysRevD.74.043001.

[48] C. G. S. Costa. The prompt lepton cookbook. *Astropart. Phys.*, 16:193–204, 2001.

[49] R. Dossi, A. Ianni, G. Ranucci, and O. Yu. Smirnov. Methods for precise photoelectron counting with photomultipliers. *Nucl. Instrum. Meth.*, A451: 623–637, 2000.

[50] Bramall N. E., R. C. Bay, K. Woschnagg, R. A. Rohde, and P. B. Price. A deep high-resolution optical log of dust, ash, and stratigraphy in south pole glacial ice. *Geophys. Res. Lett.*, 32:L21815, 2005.

[51] R. Engel, T. K. Gaisser, T. Stanev, and P. Lipari. Air shower calculations with the new version of SIBYLL, 1999. Prepared for 26th International Cosmic Ray Conference (ICRC 99), Salt Lake City, Utah, 17-25 Aug 1999.

[52] R. Engel, D. Seckel, and T. Stanev. Neutrinos from propagation of ultra-high energy protons. *Phys. Rev.*, D64:093010, 2001. doi: 10.1103/PhysRevD.64.093010.

[53] R. Engel, D. Seckel, and T. Stanev. Data Files to astro-ph/0101216, 2008. URL `ftp://ftp.bartol.udel.edu/seckel/ess-gzk/flux_n3_8_flat_om0p3.txt`. [Online; accessed 14-April-2008].

[54] G. J. Feldman and R. D. Cousins. A Unified approach to the classical statistical analysis of small signals. *Phys. Rev.*, D57:3873–3889, 1998.

[55] E. Fermi. On the Origin of the Cosmic Radiation. *Physical Review*, 75:742, 1949.

[56] H. Fesefeldt. The simulation of hadronic showers: Physics and applications, 1985. PITHA-85-02.

[57] G. Fiorentini, V. A. Naumov, and F. L. Villante. Atmospheric neutrino flux supported by recent muon experiments. *Phys. Lett.*, B510:173–188, 2001. doi: 10.1016/S0370-2693(01)00572-X.

[58] R. S. Fletcher, T. K. Gaisser, P. Lipari, and T. Stanev. Sibyll: An event generator for simulation of high-energy cosmic ray cascades. *Phys. Rev.*, D50:5710–5731, 1994.

[59] T. Gaisser. *Cosmic Rays and Particle Physics.* Cambridge University Press, 1990.

[60] T. K. Gaisser. Cosmic rays at the knee. *Astropart. Phys.*, 2006. astro-ph/0608553.

[61] T. K. Gaisser and M. Honda. Flux of atmospheric neutrinos. *Ann. Rev. Nucl. Part. Sci.*, 52:153–199, 2002. doi: 10.1146/annurev.nucl.52.050102.090645.

[62] R. Gandhi, C. Quigg, M. H. Reno, and I. Sarcevic. Ultrahigh-energy neutrino interactions. *Astropart. Phys.*, 5:81–110, 1996.

[63] R. Gandhi, C. Quigg, M. H. Reno, and I. Sarcevic. Neutrino interactions at ultrahigh energies. *Phys. Rev.*, D58:093009, 1998.

[64] A. Gazizov and M. P. Kowalski. ANIS: High energy neutrino generator for neutrino telescopes. *Comput. Phys. Commun.*, 172:203–213, 2005.

[65] L. Gerhardt. Multi-year search for UHE diffuse neutrino flux with AMANDA-II. In *Proc. 30th ICRC*, 2007. Prepared for 30th International Cosmic Ray Conference (ICRC 2007), Merida, Yucatan, Mexico, 3-11 Jul 2007.

[66] S. L. Glashow. Resonant scattering of antineutrinos. *Phys. Rev.*, 118(1): 316–317, Apr 1960. doi: 10.1103/PhysRev.118.316.

[67] R. Glasstetter et al. Analysis of electron and muon size spectra of eas. In *Proc. 26th ICRC, Salt Lake City, USA*, 1999.

[68] P. Gondolo, G. Ingelman, and M. Thunman. Charm production and high energy atmospheric muon and neutrino fluxes. *Astropart. Phys.*, 5:309–332, 1996.

[69] M. C. Gonzalez-Garcia and M. Maltoni. Phenomenology with massive neutrinos, 2007. arXiv:0704.1800.

[70] K. Greisen. End to the cosmic ray spectrum? *Phys. Rev. Lett.*, 16:748–750, 1966. doi: 10.1103/PhysRevLett.16.748.

[71] A. Gross et al. The combined AMANDA and IceCube Neutrino Telescope. In *Proc. 30th ICRC*, 2007. Prepared for 30th International Cosmic Ray Conference (ICRC 2007), Merida, Yucatan, Mexico, 3-11 Jul 2007.

[72] F. Halzen. Cosmic neutrinos from the sources of galactic and extragalactic cosmic rays. *Astrophys. Space Sci.*, 309:407–414, 2007. doi: 10.1007/s10509-007-9434-7.

[73] F. Halzen and D. Hooper. High-energy neutrino astronomy: The cosmic ray connection. *Rept. Prog. Phys.*, 65:1025–1078, 2002. doi: 10.1088/0034-4885/65/7/201.

[74] F. Halzen and D. Saltzberg. Tau neutrino appearance with a 1000-Megaparsec baseline. *Phys. Rev. Lett.*, 81:4305–4308, 1998.

[75] K. Hanson and O. Tarasova. Design and production of the IceCube digital optical module. *Nucl. Instrum. Meth.*, A567:214–217, 2006.

[76] D. Heck, J. Knapp, et al. CORSIKA: A Monte Carlo Code to Simulate Extensive Air Showers. *Forschungszentrum Karlsruhe Report FZKA*, 6019, 1998.

[77] V. F. Hess. Über Beobachtungen der durchdringenden Strahlung bei sieben Freiballonfahrten. *Phys. Z.*, 13:1084–1091, 1912.

[78] G. Hill and K. Rawlins. Unbiased cut selection for optimal upper limits in neutrino detectors: The model rejection potential technique. *Astropart. Phys.*, 19:393–402, 2003. doi: 10.1016/S0927-6505(02)00240-2.

[79] A. M. Hillas. The Origin of Ultrahigh-Energy Cosmic Rays. *Ann. Rev. Astron. Astrophys.*, 22:425–444, 1984. doi: 10.1146/annurev.aa.22.090184.002233.

[80] J.R. Hoerandel. On the knee in the energy spectrum of cosmic rays. *Astropart. Phys.*, 19:193–220, 2003.

[81] L. Holmstrom, S. R. Sain, and H. E. Miettinen. A New multivariate technique for top quark search. *Comput. Phys. Commun.*, 88:195–210, 1995.

[82] M. Honda, T. Kajita, K. Kasahara, S. Midorikawa, and T. Sanuki. Calculation of atmospheric neutrino flux using the interaction model calibrated with atmospheric muon data. *Phys. Rev.*, D75:043006, 2007. doi: 10.1103/PhysRevD.75.043006.

[83] D. Hooper, A. Taylor, and S. Sarkar. The impact of heavy nuclei on the cosmogenic neutrino flux. *Astropart. Phys.*, 23:11–17, 2005. doi: 10.1016/j.astropartphys.2004.11.002.

[84] P. A. Čerenkov. Visible radiation produced by electrons moving in a medium with velocities exceeding that of light. *Phys. Rev.*, 52(4):378–379, Aug 1937. doi: 10.1103/PhysRev.52.378.

[85] J.D. Jackson. *Classical Electrodynamics*. Wiley, New York, USA, 3 edition, 1996.

[86] U. F. Katz. KM3NeT: Towards a km**3 Mediterranean neutrino telescope. *Nucl. Instrum. Meth.*, A567:457–461, 2006. doi: 10.1016/j.nima.2006.05.235.

[87] J. Kelley. dCORSIKA, 2007. URL `http://icecube.wisc.edu/~jkelley/simulation/dcorsika.html`.

[88] J. Kelley and J. Braun. DOM-Cal Users' Guide, 2004.

[89] Till A. Kirsten. Solar neutrino experiments: results and implications. *Rev. Mod. Phys.*, 71(4):1213–1232, Jul 1999. doi: 10.1103/RevModPhys.71.1213.

[90] J. Kiryluk et al. IceCube performance with artificial light sources: The road to cascade analyses. In *Proc. 30th ICRC*, 2007. Prepared for 30th International Cosmic Ray Conference (ICRC 2007), Merida, Yucatan, Mexico, 3-11 Jul 2007.

[91] S. Klein. Suppression of bremsstrahlung and pair production due to environmental factors. *Rev. Mod. Phys.*, 71:1501–1538, 1999.

[92] S. Klein. Cascades from nu/e above 10**20-eV. *Astropart. Phys.*, 2004. astro-ph/0412546.

[93] S. Kleinfelder. Gigahertz waveform sampling and digitization circuit design and implementation. *Nuclear Science, IEEE Transactions on*, 50:955–962, 2003.

[94] B. Knuteson, H. Miettinen, and L. Holmstrom. alphaPDE: A New Multivariate Technique for Parameter Estimation. *Comput. Phys. Commun.*, 145: 351–356, 2002.

[95] H. Kolanoski. Einführung in die Astroteilchenphysik, 2007. URL `http://www-zeuthen.desy.de/~kolanosk/astro0607/welcome.html`.

[96] M. Kowalski. Measuring diffuse neutrino fluxes with IceCube. *JCAP*, 0505: 010, 2005. doi: 10.1088/1475-7516/2005/05/010.

[97] M. Kowalski. On the Cherenkov light emission of hadronic and electromagnetic cascades. AMANDA Internal Report 20020803, 2002.

[98] M. Kowalski. *Search for neutrino induced cascades with the AMANDA-II detector*. PhD thesis, Humboldt-Universität zu Berlin, 2004.

[99] M. Kowalski and A. Mohr. Detecting neutrino-transients with optical follow-up observations. *Astropart. Phys.*, 27:533–538, 2007. doi: 10.1016/j.astropartphys.2007.03.005.

[100] M. Kowalski and I. Taboada. Cascade reconstruction in AMANDA, 2001. Prepared for 2nd Workshop on Methodical Aspects of Underwater/Ice Neutrino Telescopes, Hamburg, Germany, 15-16 Aug 2001.

[101] I. Kravchenko et al. RICE limits on the diffuse ultra-high energy neutrino flux. *Phys. Rev.*, D73:082002, 2006. doi: 10.1103/PhysRevD.73.082002.

[102] H. L. Lai et al. Global QCD analysis of parton structure of the nucleon: Cteq5 parton distributions. *Eur. Phys. J.*, C12:375–392, 2000. URL `http:www.phys.psu.edu/~cteq/`.

[103] L. D. Landau and I. Pomeranchuk. Electron cascade process at very high-energies. *Dokl. Akad. Nauk Ser. Fiz.*, 92:735–738, 1953.

[104] J. G. Learned and K. Mannheim. High-energy neutrino astrophysics. *Ann. Rev. Nucl. Part. Sci.*, 50:679–749, 2000.

[105] J. Lundberg. Unblinding proposal amanda-ii 2003+2004 uhe analysis, 2008.

[106] J. Lundberg et al. Light tracking for glaciers and oceans: Scattering and absorption in heterogeneous media with photonics. *Nucl. Instrum. Meth.*, A581:619–631, 2007.

[107] K. Mannheim, R. J. Protheroe, and J. P. Rachen. On the cosmic ray bound for models of extragalactic neutrino production. *Phys. Rev.*, D63:023003, 2001. doi: 10.1103/PhysRevD.63.023003.

[108] A. B. McDonald, C. Spiering, S. Schonert, E. T. Kearns, and T. Kajita. Astrophysical neutrino telescopes. *Rev. Sci. Instrum.*, 75:293–316, 2004. doi: 10.1063/1.1642740.

[109] P. Meszaros. Gamma-Ray Bursts. *Rept. Prog. Phys.*, 69:2259–2322, 2006.

[110] E. Middell, 2008. Personal communication.

[111] G. Mie. Beiträge zur Optik trüber Medien, speziell kolloidaler Metallösungen. *Ann. Phys.*, 25:377, 1908.

[112] P. Miocinovic. Muon energy reconstruction in the Antarctic Muon and Neutrino Detector Array (AMANDA), 2001. UMI-30-62680.

[113] I. F. Mirabel. Very energetic gamma-rays from microquasars and binary pulsars. *Science*, 312:1759–1760, 2006.

[114] R.M. Neal. Probabilistic inference using markov chain monte carlo methods, 1993. URL `http://www.cs.toronto.edu/~radford/res-mcmc.html`. Technical Report CRG-TR-93-1, Dept. of Computer Science, University of Toronto.

[115] W. Nelson, H. Hirayama, and D. Rogers. The egs4 code system, 1985. SLAC-0265.

[116] V. Niess and V. Bertin. Underwater acoustic detection of ultra high energy neutrinos. *Astropart. Phys.*, 26:243–256, 2006.

[117] S. Panknin. Cascade Monte Carlo with Muons, 2007. URL `http://eeh06.physik.hu-berlin.de/~panknin/cmc/`.

[118] D.H. Perkins. *Particle Astrophysics.* Oxford University Press, 2003.

[119] W. Press, S. Teukolsky, W. Vetterling, and B. Flannery. *Numerical Recipies in C.* Cambridge University Press, Cambridge, UK, 2 edition, 1997.

[120] P. B. Price and K. Woschnagg. Role of group and phase velocity in high-energy neutrino observatories. *Astropart. Phys.*, 15:97–100, 2001.

[121] R Development Core Team. *R: A Language and Environment for Statistical Computing.* R Foundation for Statistical Computing, Vienna, Austria, 2008. URL `http://www.R-project.org`. ISBN 3-900051-07-0.

[122] M. Ribordy and G. Japaridze. Reconstruction PDF in an Inhomgeneous Medium. AMANDA Internal Report 20050301, 2005.

[123] D. W. Scott. *Multivariate Density Estimation.* J. Wiley & Sons, Inc., New York, 1992.

[124] D. W. Scott and S. R. Sain. (multi-dimensional density estimation, handbook of statistics, volume 24: Data mining and data visualization, 2004.

[125] A. Silvestri. *Limit On Ultra High Energy Neutrino Flux.* PhD thesis, University of California, Irvine, 2007.

[126] F. W. Stecker. A note on high energy neutrinos from AGN cores. *Phys. Rev.*, D72:107301, 2005. doi: 10.1103/PhysRevD.72.107301.

[127] F. W. Stecker, C. Done, M. H. Salamon, and P. Sommers. High-energy neutrinos from active galactic nuclei. *Phys. Rev. Lett.*, 66(21):2697–2700, May 1991. doi: 10.1103/PhysRevLett.66.2697.

[128] R. Stokstad. Design and performance of the IceCube electronics, 2005. Prepared for 11th Workshop on Electronics for LHC and Future Experiments (LECC 2005), Heidelberg, Germany, 12-16 September 2005.

[129] R. Stokstad. RAP - A Method for Absolute Time Calibration of a Large Array based on a digital Optical Module System, 1998. LBNL-43200.

[130] M. Takeda et al. Extension of the cosmic-ray energy spectrum beyond the predicted greisen-zatsepin-kuz'min cutoff. *Phys. Rev. Lett.*, 81(6):1163–1166, Aug 1998. doi: 10.1103/PhysRevLett.81.1163.

[131] O. Tarasova, M. Kowalski, and M. Walter. Search for neutrino-induced cascades with AMANDA data taken in 2000-2004. In *Proc. 30th ICRC*, 2007. Prepared for 30th International Cosmic Ray Conference (ICRC 2007), Merida, Yucatan, Mexico, 3-11 Jul 2007.

[132] Y.-S. Tsai. Pair production and bremsstrahlung of charged leptons. *Rev. Mod. Phys.*, 46(4):815–851, Oct 1974. doi: 10.1103/RevModPhys.46.815.

[133] G. van Rossum et al. *Python Library Reference*, 2008. URL `http://www.python.org`.

[134] E. Waxman. Cosmological origin for cosmic rays above 10**19-eV. *Astrophys. J.*, 452:L1–L4, 1995.

[135] E. Waxman and J. Bahcall. High energy neutrinos from cosmological gamma-ray burst fireballs. *Phys. Rev. Lett.*, 78(12):2292–2295, Mar 1997. doi: 10.1103/PhysRevLett.78.2292.

[136] E. W. Weisstein. Beta Distribution — From MathWorld – A Wolfram Web Resource, 2008. URL `http://mathworld.wolfram.com/BetaDistribution.html`.

[137] E. W. Weisstein. Erlang Distribution — From MathWorld – A Wolfram Web Resource, 2008. URL `http://mathworld.wolfram.com/ErlangDistribution.html`.

[138] C. Wiebusch. *The detection of faint light in deep underwater neutrino telescopes.* PhD thesis, Technische Hochschule Aachen, 1995. PITHA-95-37.

[139] C. Wiedemann. Unblinding proposal 2003 stockholm uhe analysis, 2007.

[140] Wikipedia. Naive Bayes Classifier — Wikipedia, The Free Encyclopedia, 2008. URL `http://en.wikipedia.org/wiki/Naive_Bayes_classifier`. [Online; accessed 21-March-2008].

[141] Wikipedia. Beta Distribution — Wikipedia, The Free Encyclopedia, 2008. URL `http://en.wikipedia.org/wiki/Erlang_distribution`. [Online; accessed 11-March-2008].

[142] Wikipedia. Statistical Classification — Wikipedia, The Free Encyclopedia, 2008. URL `http://en.wikipedia.org/wiki/Statistical_classification`. [Online; accessed 21-March-2008].

[143] Wikipedia. Erlang Distribution — Wikipedia, The Free Encyclopedia, 2008. URL `http://en.wikipedia.org/wiki/Erlang_distribution`. [Online; accessed 01-March-2008].

[144] H. Wissing, 2007. Personal communication.

[145] T. Yamamoto. The UHECR spectrum measured at the Pierre Auger Observatory and its astrophysical implications. *Astropart. Phys.*, 2007. arXiv:0707.2638.

[146] W.-M. Yao et al. Review of particle physics. *J. Phys.*, G33:1–1232, 2006.

[147] S. Yoshida and M. Teshima. Energy spectrum of ultrahigh-energy cosmic rays with extragalactic origin. *Prog. Theor. Phys.*, 89:833–845, 1993. doi: 10.1143/PTP.89.833.

[148] E. Zas, F. Halzen, and T. Stanev. Electromagnetic pulses from high-energy showers: Implications for neutrino detection. *Phys. Rev.*, D45:362–376, 1992.

[149] G. T. Zatsepin and V. A. Kuzmin. Upper limit of the spectrum of cosmic rays. *JETP Lett.*, 4:78–80, 1966.

Danksagung

An dieser Stelle möchte ich mich bei den vielen Menschen bedanken, die diese Arbeit ermöglicht haben. Die Arbeit wäre ohne die Hilfe vieler Kollegen und Freunde nicht zustande gekommen. Während meiner Zeit als Doktorand habe ich sehr viel gelernt, dank der Hilfe- und Fragestellungen meiner Betreuer und Mitstreiter. Ich bin glücklich dass Ihr mir geholfen habt. Vielen herzlichen Dank! Ich hoffe die Dinge, die ich von Euch gelernt habe, weiter in die Welt zu tragen.

Im Speziellen möchte ich mich bei Prof. Hermann Kolanoski bedanken, für das Vertrauen als Doktorvater einzustehen. Dr. Christian Spiering sei gedankt für die Einstellung und die freundschaftliche Atmosphäre in der Arbeitsgruppe. Einen herzlichen Dank an Dr. Rolf Nahnhauer für drei-einhalb Jahre tolle und antreibende Betreuung. Vielen Dank an Dr. Marek Kowalski für die vorzüglichen Ratschläge und bemerkenswerte Diskussionen gerade in den letzten Monaten der Analysearbeit. Vielen Dank auch für das Engagement beim "last-minute" Korrekturlesen! Bei Prof. Shigeru Yoshida bedanke ich mich herzlich für die Übernahme des Gutachtens.

Ein ganz großer Dank geht an die gesamte Zeuthener-Arbeitsgruppe und an die IceCube Kollaboration. Ich hatte eine wunderschöne und ereignisreiche Zeit! Vielen Dank für gemeinsame sportliche Aktivitäten, Kartenspielen, Essen und (Kaffee-) Trinken, Reisen, technische Tips und Diskussionen und vieles mehr. Mein herzlicher Dank geht an: Stefan K., Sebastian B., Michael B., Kevin, Michael W., Stefan S., Jan-Henrik F., Eike M., Delia, Fabian, Adam, Pepe, Sirin, Sebastian P., Robert F., Robert L., Konstancja, Martin T., Martin B., Markus, Oxana, Elisa, Julien, Justin, Arthur, Kalle, Holger, Hubert, Kael, Chris W., Jim H., ...
Vielen Dank an alle Korrekturleser, das war eine großartige Hilfe!

Mein allergrößter Dank gebührt Tina und Emil, ohne Euch hätte ich es nicht geschafft, ich hoffe ich kann Euch alles zurückgeben, was ihr mir gegeben habt.

Mit Liebe, Bernhard

Selbständigkeitserklärung

Hiermit erkläre ich, diese Arbeit sebstständig und nur unter Verwendung der angegebenen Literatur und Hilfsmittel erstellt zu haben.

Bernhard Voigt Berlin, 30.04.2008